Influence of Vane Sweep on Rotor-Stator Interaction Noise

Edmane Envia
Sverdrup Technology, Inc.
Lewis Research Center Group
Brook Park, Ohio

and

Edward J. Kerschen
University of Arizona
Tucson, Arizona

December 1990

NASA

National Aeronautics and
Space Administration
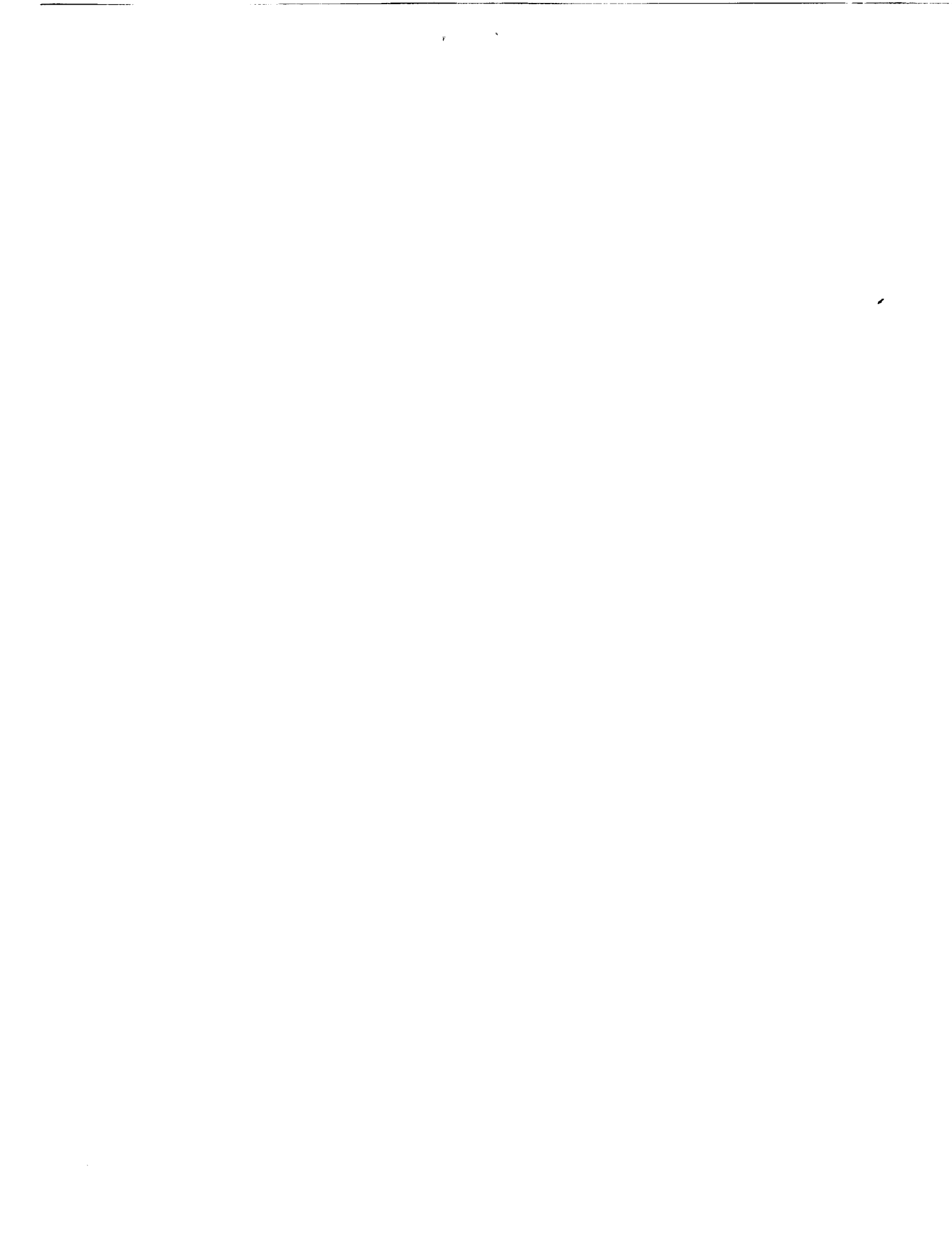
TABLE OF CONTENTS

Page

LIST OF ILLUSTRATIONS

LIST OF ILLUSTRATIONS--<u>continued</u>

Page

v

Page

LIST OF ILLUSTRATIONS--<u>continued</u>

Page

viii

LIST OF TABLES

ABSTRACT

In this study the influence of vane sweep on rotor-stator interaction noise is investigated. In an analytical approach, the interaction of a convected gust, representing the rotor viscous wake, with a cascade of finite span swept airfoils, representing the stator, is analyzed. The analysis is based on the solution of the exact linearized equations of motion. High-frequency convected gusts for which noise generation is concentrated near the leading edge of the airfoils are considered.

In a preliminary study, the problem of an isolated finite span swept airfoil interacting with a convected gust is analyzed. Using Fourier transform methods and the Wiener-Hopf technique, an approximate solution for this problem is developed. Closed form expressions for the acoustic farfield are obtained and used in a parametric study to assess the effect of airfoil sweep on noise generation. Results indicate that sweep can substantially reduce the farfield noise levels for a single airfoil.

Utilizing the single airfoil model, an approximate solution to the problem of noise radiation from a cascade of finite span swept airfoils interacting with a convected gust is derived. Only upstream radiated noise is considered. Neglecting the weak coupling between the adjacent airfoils at high frequencies, the cascade solution is constructed as a superposition of acoustic farfields emanating from an infinite number of isolated airfoils. A parametric study of noise generated by gust-cascade interaction is then carried out to assess the effectiveness of vane sweep in reducing rotor-stator interaction noise. The results of the parametric study show that, over a fairly wide range of conditions, sweep is beneficial in reducing noise levels. One conclusion of particular importance is that rotor wake twist or circumferential lean substantially influences the effectiveness of vane sweep. The orientation of the vane sweep must be chosen to enhance the natural phase lag caused

1

by wake lean, in which case rather small sweep angles substantially reduce the noise levels.

CHAPTER 1

INTRODUCTION

In view of the stringent community noise regulations, the prediction and suppression of noise generated by the propulsion system of large commercial aircraft has become an issue of critical importance. Over the past three decades, comprehensive research programs have been implemented to identify the various engine noise sources and devise viable means of reducing the generated noise levels. With the emergence of high-bypass ratio turbofan engines, particular emphasis has been placed on reducing the noise associated with the fan component. This reflects the fact that, for such an engine, the fan is the dominant source of noise on both landing approach and takeoff (see, for example, Hodge (1980)). Indeed, preliminary studies of advanced engine concepts (Johnston (1978) and Owens (1979)) indicate that the fan will remain a significant source of propulsion noise for the next generation turbofan engines as well. As such, NASA[†] and the private industry have been engaged in active research to further the ability to predict and control the fan assdciated noise.

A principal mechanism responsible for the generation of fan noise is the interaction of blade rows with convected disturbances present in the flow. The convected disturbances, or gusts, are unsteady fluctuations in the flow quantities that are carried by the flow. They are generated in the exterior as well as the interior of the engine. Atmospheric turbulence is a common example of the former while inlet boundary layer

---

[†] A summary of recent NASA-initiated work can be found in a review article by Groeneweg and Rice (1987).

3

instabilities are typical of the latter. The interaction of such gusts with fan blades produces broadband, or random, noise. The most important type of a convected gust, however, is the periodic disturbance field associated with the velocity deficits of viscous wakes of the fan (rotor) blades. The interaction of these periodic velocity fluctuations with downstream outlet guide vanes (stator) produces discrete frequency noise or pure tones. This source, often referred to as rotor-stator interaction noise, is particularly significant during approach and landing. It is the suppression of this source of fan noise that is the subject of this study.

The engine components relevant to rotor-stator interaction noise are highlighted in Fig. (1.1). The basic mechanism underlying the rotor-stator noise generation process can be described as follows. Ignoring the presence of the stator for a moment, the flow downstream of the rotor is steady in a frame of reference fixed with respect to the rotor. This flow consists of a mean component and a spatially periodic disturbance component due to the velocity deficits of the viscous wakes shed from the fan blades. The velocity deficits are typically small compared with the mean component, and hence they may be assumed to convect at the mean flow velocity. Although viscosity is responsible for producing the wakes, little viscous diffusion occurs over the short distances in which the interaction with the stator vanes takes place. Hence, these small-amplitude convecting velocity disturbances (called vortical gusts) may be assumed to convect inviscidly.

Switching to a stationary frame of reference fixed with respect to the stator vanes, the rotor induced vortical gust is now a function of both space and time. In effect, the spatial periodicity of velocity perturbations in the rotor-fixed coordinates gives rise to a temporal periodicity in the stator-fixed coordinates. The temporal dependence of the gust impinging on the stator vanes is expressible in terms of a Fourier series involving the

4

Rotor Viscous Wakes

Acoustic Waves (Noise)

Bypass Duct

Fan (Rotor)

Outlet Guide Vanes (Stator)
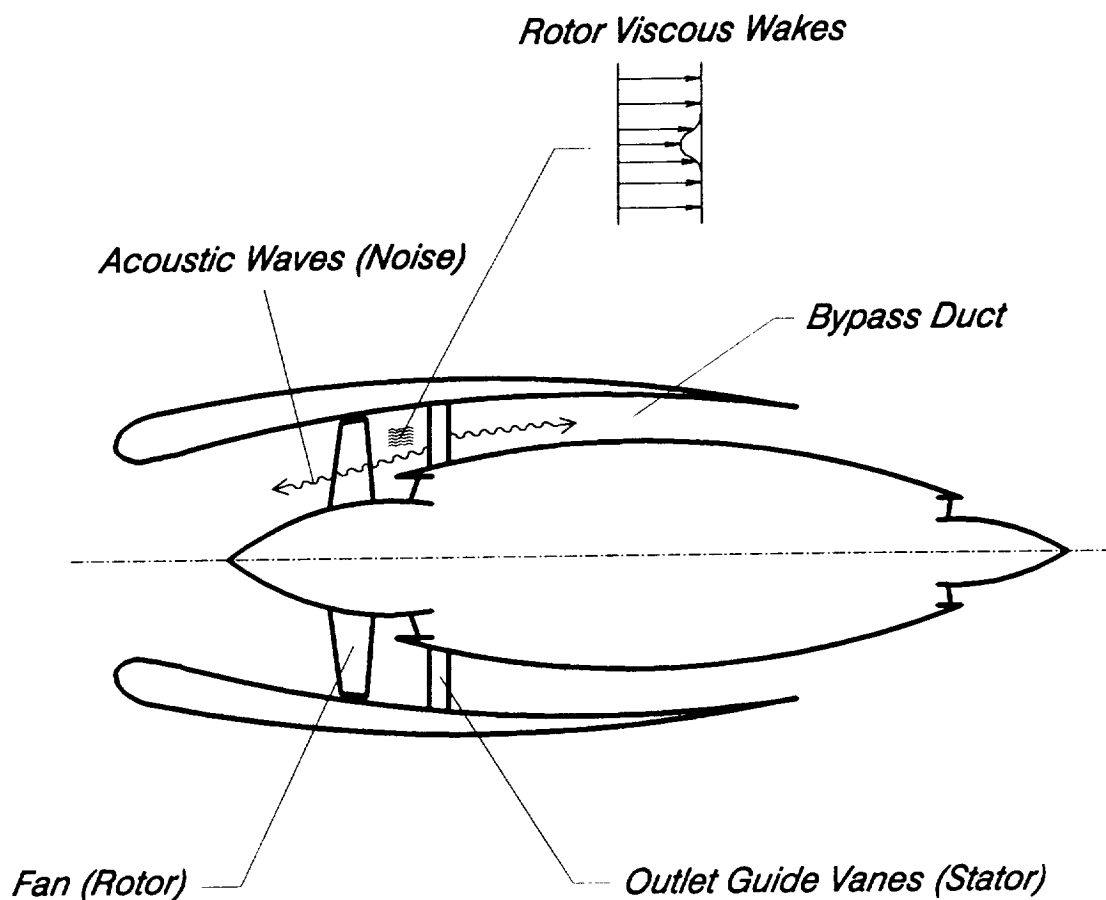
Fig. 1.1   High-bypass ratio turbofan engine components relevant to rotor-stator interaction noise.

5

blade-passing frequency (the frequency at which rotor blades pass a stator vane) and its higher harmonics. The rotor-stator interaction noise is caused by the time-periodic pressure forces (i.e., unsteady aerodynamic loading) exerted on stator vanes as a result of the rotor vortical gust. This unsteady loading generates pressure waves that propagate through the compressible medium and are perceived as pure tones at the blade-passing frequency (BPF) and its higher harmonics. Equivalently, the unsteady loading on each stator vane may be thought of as a surface distribution of acoustic dipole sources, each radiating a tone at the same frequency.

Rotor-stator interaction noise can be reduced by decreasing the strength of the interaction or by decreasing the efficiency with which the source radiates acoustic waves. Since viscous wakes decay with downstream distance, the intensity of the interaction can be reduced by increasing the axial spacing between the rotor and the stator. However, increases in spacing impose weight and efficiency penalties and, furthermore, beyond moderate spacings the wake decay with downstream distance is quite gradual. The more successful approaches to noise reduction have generally modified the interaction such that propagating acoustic duct modes are not strongly excited. In particular, a proper choice of the blade/vane count ratio can completely eliminate the noise at BPF by causing destructive interference between acoustic fields generated at different stator vanes (Tyler and Sofrin (1961)). This phenomenon is commonly referred to as cut-off. Although, in principle, the same method is applicable for cutting off the higher harmonics of the BPF noise, the required vane counts are quite high and thus impose cost and weight penalties.

A similar cut-off phenomenon can be achieved by the introduction of stator vane sweep. Here sweep refers to a configuration where the leading edge of the vane is no longer perpendicular to the streamwise direction. Cut-off in this case is a result of

6

destructive interference between the acoustic fields generated at different locations along the span of the same vane. For a vane of infinite span and for sweep angles beyond a critical value, the farfield noise is completely eliminated provided that the vortical gust is harmonic and has a constant amplitude along the span. This cut-off phenomenon can also be explained in terms of the gust spanwise trace velocity relative to the oncoming mean flow. This is the velocity of the intersection point between the leading edge of the airfoil and the gust constant phase line as the gust convects past the airfoil. For supersonic relative trace velocities noise is radiated to the farfield while for subsonic trace velocities destructive interference completely eliminates the noise radiation. For stator row Mach numbers typical of current turbofan designs large enough sweep angles (details to be given in Chapter 3) will reduce the gust relative trace velocity to a subsonic value resulting in a cut-off noise field for an infinite span airfoil.

The complete destructive interference leading to cut-off requires perfect symmetry. In the case where cut-off is due to proper choice of blade/vane count ratios, the symmetry is destroyed only by manufacturing imperfections. In contrast, the perfect symmetry required for complete cut-off by vane sweep can never be achieved in actual applications. The vane span is finite and there are generally variations in the gust amplitude along the span. These two features destroy the perfect symmetry that leads to cut-off and thus nonzero noise levels are present beyond the critical sweep angle.

Fortunately, in most aeronautical applications, the sound produced by rotor-stator interaction has wavelengths that are small compared to the vane span. In this situation the end wall influence is confined to a small region whose characteristic length is comparable to the sound wavelength. Similarly, spanwise gradients in the gust amplitude should be less important at high frequencies. Therefore, vane sweep may provide sizable reductions in

the noise level generated by rotor-stator interaction. Furthermore, since the effectiveness of sweep is based on modifying the acoustic field generated at a single vane, it is reasonable to expect that it should be equally advantageous in a cascade configuration. The objective of this study is to quantify the reductions that can be achieved in the level of rotor-stator interaction noise as a result of the introduction of vane sweep.

The classical approach to the analysis of noise generated by rotor-stator interaction is to separate the problem into aerodynamic and acoustic parts. First, unsteady aerodynamics is utilized to determine the unsteady lift on the stator vanes due to interaction with a vortical gust representing the rotor viscous wake. The individual vanes are then treated as point sources in the sound radiation calculation.

The separation into aerodynamic and acoustic parts is most useful when the acoustic wavelength is large compared to the airfoil chord. This occurs when the Mach number of the flow is fairly low and/or when the rotor gust chordwise wavelength is large compared with the stator vane chord. Under these conditions the wavelength of the sound generated is much larger than the vane chord, and hence each vane can be considered as a single compact dipole noise source. The great simplification that occurs in the compact source (i.e., low-frequency) approximation is that the aerodynamics can be treated as incompressible and only the total unsteady lift on each stator vane is needed to determine the acoustic radiation. Two-dimensional incompressible aerodynamic theories for gust-airfoil interaction were first developed by Küssner (1936), and von Kármán and Sears (1938). Gutin's (1948) propeller theory was one of the first compact source dipole acoustic radiation models.

As the Mach number increases, the compact source approximation is applicable only to very long wavelength gusts. In most aeronautical applications, however, the gust

wavelengths are on the order of or shorter than the chord of a stator vane. Therefore, in situations of practical interest, the compact source approximation does not apply. The classical separation into aerodynamic and acoustic parts is no longer advantageous for the noncompact source case. In contrast to the compact source case, for the noncompact case the acoustic wave motion near the airfoil must be included in the unsteady aerodynamic model. There is then little benefit in solving for the aerodynamics separately. In fact, in the highly noncompact (i.e., high-frequency) regime, it is most sensible to calculate the farfield radiated noise directly from the equations governing the wave motion everywhere in the fluid.

Probably for historical reasons the problem of noise generated by gust-airfoil interaction is often approached from the classical viewpoint. As a result, considerable effort has been devoted to improving the aerodynamic predictions. For the most part theories have been developed for infinite span airfoils interacting with convected gusts. Filotas (1969) obtained closed form lift expressions for an airfoil encountering an oblique sinuosoidal gust in an incompressible stream. In a numerical calculation, Graham (1970) included the effects of compressibility. Using essentially acoustic theories Adamczyk (1974) developed analytical models which extended the aerodynamic response into regions where the compressibility effects are important. In generalizing this work Amiet (1976) showed that at high frequencies the airfoil response is dominated by the region near the leading edge. One of the few unsteady compressible aerodynamic calculations to consider the end effects is due to Martinez and Widnall (1983). This work is restricted to square wing tip loading and hence is not applicable to stator vane geometries resulting from arbitrary sweep.

In so far as the acoustic response of finite span airfoils is concerned, only a few researchers have investigated the sweep effects. A brief rotor-stator noise analysis

incorporating stator vane as well as rotor blade leading-edge sweep and finite span effects was presented by Hayden and Bliss (1977). They used the compact source approximation in conjunction with an acoustic analogy approach. The end wall effects were treated by assuming that the ends of the airfoils radiated incoherently. The analysis was mostly focused on the actual design of a low noise fan stage and was somewhat qualitative. A lifting surface theory which accounts for blade lean rather than sweep was presented by Schulten (1981).

In the present study, an approximate analytical model of noise generated by the interaction of high-frequency vortical gusts with cascades of finite span swept airfoils is developed. The model accounts for gust three-dimensionality as well as compressibility and noncompactness effects. In Chapter 2, an approximate model for the rotor viscous wake is presented and the derivation of the exact linearized differential equations governing the generation of sound by gust-airfoil interaction is reviewed. Chapter 3 considers the kernel problem of a single finite span swept airfoil interacting with a harmonic high-frequency gust. A detailed parametric study of the gust response is also included in that chapter. This solution is then used to construct an approximate model for the farfield sound produced by a cascade of swept airfoils interacting with a rotor viscous wake. The cascade model is developed in the first part of Chapter 4. In the second part of that chapter, the wake model of Chapter 2 is utilized to perform a parametric study of the influence of vane sweep on rotor-stator interaction noise. This parametric study quantifies the effectiveness of vane sweep as a means of reducing rotor-stator interaction noise in realistic situations. Finally, in Chapter 5 conclusions from this study and recommendations for future extensions are summarized.

Results from this work have been reported in Kerschen and Envia (1983) and Envia and Kerschen (1984 and 1986).

CHAPTER 2

ROTOR VISCOUS WAKE MODEL AND
ACOUSTIC DISTURBANCE EQUATIONS

In this chapter, an approximate descriptions for the rotor viscous wake is developed and the derivation of the equations governing sound generation by gust-airfoil interaction is reviewed.

2.1 Rotor Viscous Wake Model

In deriving the rotor viscous wake model, the effect of the downstream stator is neglected. Consequently, the flow downstream of the rotor is steady if viewed in a frame of reference fixed to the moving blades. It consists of a mean part and a spatially periodic small-amplitude disturbance part. For the purpose of this study, it is sufficient to consider the mean component as a uniform flow. On the other hand, the disturbance component which represents the rotor viscous wake must be modeled more precisely.

Rotor wakes typically exhibit a complicated three-dimensional structure which depends on the details of the fan design. Accurate prediction of the detailed structure is a formidable task which taxes the capability of available computational methods. However, the goal of this study is to provide general guidance through parametric studies of rotor-stator interaction noise. In fact, strictly speaking, the interest here is in the relative comparison of noise levels for swept versus unswept vanes rather than in accurate predictions of the absolute noise levels. Thus, here a simplified model of the rotor viscous wake which includes those features that are expected to have critical influence on the relative noise levels is utilized.

11

In general, the wake of a rotor blade has a deficit velocity and half-width which are functions of the radial coordinate. The variations with radius initially arise due to radial variations in rotor loading. As the wake convects downstream, the deviation in rotor loading from a forced vortex design creates swirl velocities that produce a "twist" or circumferential lean which increases with downstream distance. The wake centerline deficit and half-width also change with downstream distance, and these changes themselves depend on radial location due to the same mechanisms that produce the wake lean. Finally, there are the complicated three-dimensional features created by tip vortices and the effective body force in the rotating reference frame. In this work, wake lean, radial variations of wake centerline deficit velocity, and half-width are accounted for, but the influence of tip vortices is neglected.

For the sake of mathematical simplicity, the engine wall curvature effects are ignored. The engine annulus can then be "unrolled" to form a linear cascade as sketched in Fig. (2.1). The rotor blade and stator vane rows along with their appropriate coordinate systems are shown. The rotor blade-coordinate system (x_r^*, y_r^*, z_r^*) is fixed to the trailing edge of a typical rotor blade arbitrarily denoted as the zeroth blade. The coordinate axes x_r^* and y_r^* are aligned with and perpendicular to the blade, respectively. It is convenient to nondimensionalize all the coordinates by the channel height. Thus, in terms of nondimensional quantities, the coordinate $z_r^* = 0$ corresponds to the hub, or inner wall, and $z_r^* = 1$ corresponds to the shroud, or outer wall. U_r^*, the uniform mean flow velocity relative to the rotor blades, is along the coordinate axis x_r^*. v^* is the wake deficit velocity profile with v_c as the centerline deficit along the coordinate axis x_r^*. The rotor-fixed coordinate system (x_r, y_r, z_r) is also fixed to the trailing edge of the zeroth rotor blade, but
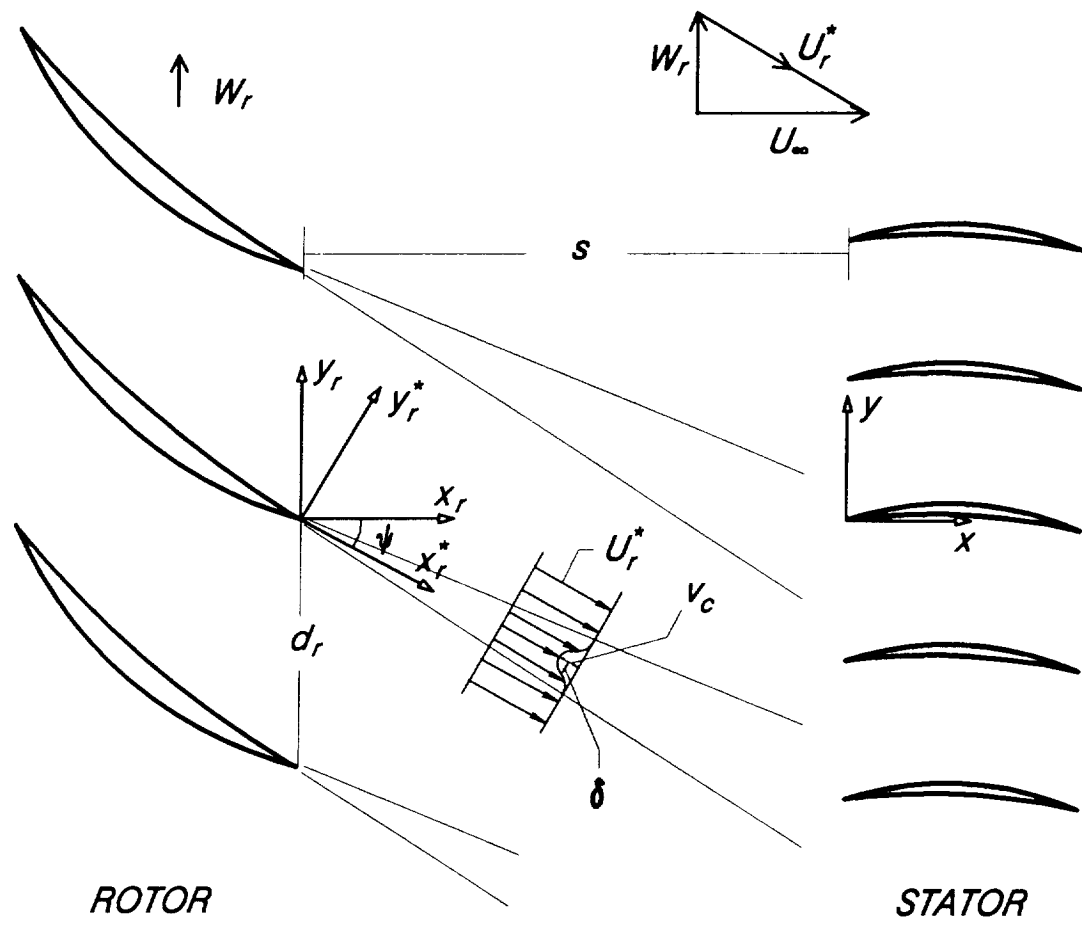
Fig. 2.1   Rotor and Stator linear cascades and coordinate systems. z_r^*, z_r, and z are out of the paper.

is aligned with the engine axis. The stator-fixed coordinate system (x,y,z) is centered on the leading edge of and aligned with the chord of the zeroth stator vane.

The simplest rotor wake model consistent with the unrolled cascade approximation is a deficit pattern that is periodic with rotor blade spacing and independent of the "radial" coordinate z_r^*. Since over small rotor-stator separations, typical of current engine designs, the viscous diffusion effects are not significant they will be ignored here. Then, the profile of the wake of an individual blade can be represented by an inviscid shear pertur-bation of the uniform mean flow. The wake deficit and half-width can be chosen consistent with average values of experimental measurements at an axial distance corresponding to the location of stator vanes leading edges. This type of model, which was first developed by Kemp and Sears (1955), lacks several features that are important for predicting the influence of vane sweep on the noise generation process. The most important of these is the wake circumferential lean which significantly modifies the wake trace velocity along the vane leading edge and thus influences the effectiveness of sweep. The influence of wake lean is incorporated in the analysis by assuming that the wake centerline location for a given rotor blade is a linear function of z_r^* and consequently of z_r and z (see Fig. (2.2)). Reasonable estimates of the lean angle can be made using available experimental data. Another feature which may be of some importance is the radial variation of the wake deficit velocity. This is accounted for by allowing v_c to depend on z_r^* as well.

Consider, then, the following inviscid shear perturbation representation of the wake of the zeroth rotor blade expressed in the rotor blade-fixed coordinate system (x_r^*, y_r^*, z_r^*),

$$v_0^*(x_r^*, y_r^*, z_r^*) = v_c(z_r^*) \, e^{-\ln 2 \, (y_r^* \cos\Gamma + z_r^* \sin\Gamma)^2/\delta^2} \qquad (2.1)$$

14
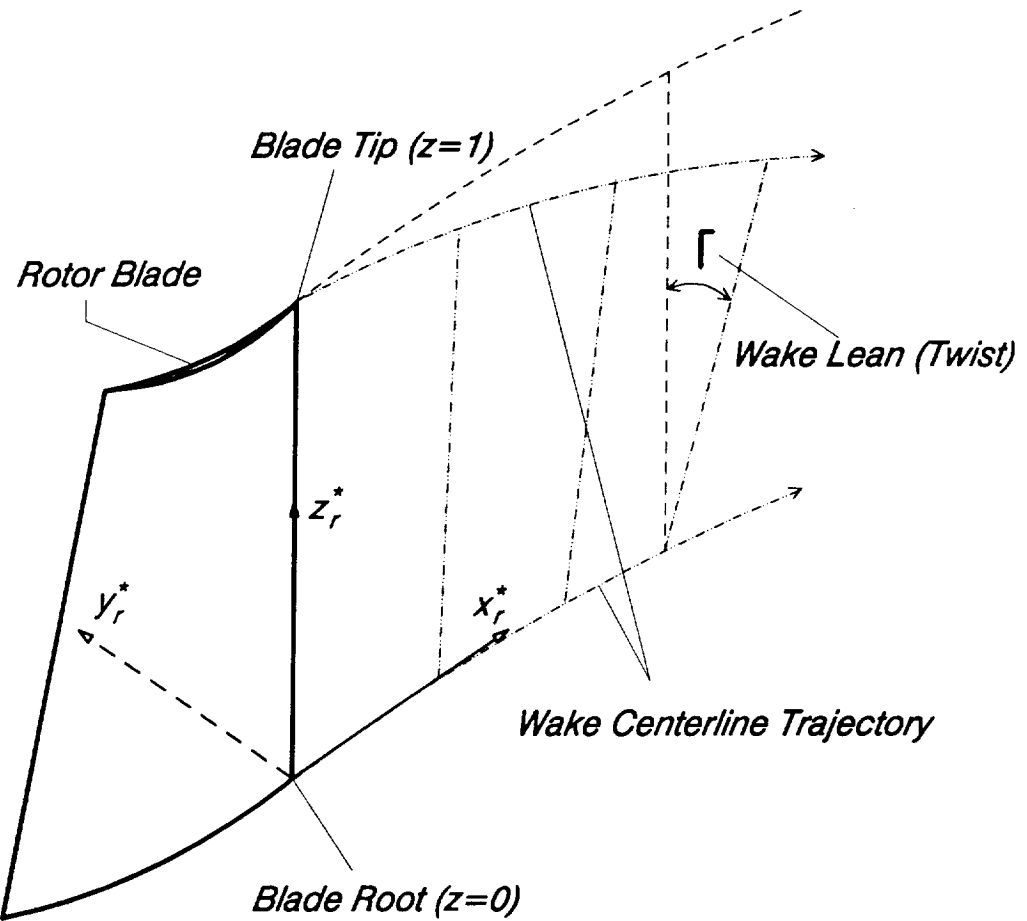
Fig. 2.2 Circumferential lean of a rotor blade viscous wake.

where for the sake of mathematical simplicity the wake profile is modeled as Guassian. As shown in Fig. (2.2) Γ is the angle representing the lean of the wake with respect to the z^*-axis. δ, depicted in Fig. (2.1), is the wake half-width[†] of the leaned wake. Although, the centerline deficit velocity $v_c(z_r^*)$ can, in general, be any function of z_r^*, in this study only linear variations with respect to z_r^* are considered. The extension to other cases is straightforward. Since the rotor blades move along the y_r direction, it is convenient to rewrite Eq. (2.1) in the (x_r, y_r, z_r) coordinate system. Thus,

$$v_0^*(x_r, y_r, z_r) = v_c(z_r)\, e^{-\ln 2\,(x_r \sin\psi + y_r \cos\psi + z_r \tan\Gamma)^2 \cos^2\Gamma/\delta^2} \tag{2.2}$$

where ψ is the stagger angle of the rotor blades with respect to the streamwise direction (see Fig. (2.1)). Now, the nth rotor blade sheds a wake identical to that described by Eq. (2.2), but displaced a distance nd_r in the y_r direction (d_r is the nondimensionalized rotor blade spacing shown in Fig. (2.1)). Summing over the infinite number of rotor blades one finds

$$U_r(x_r, y_r, z_r) = U_r^* - \sum_{n=-\infty}^{+\infty} v_n^*(x_r, y_r, z_r) \tag{2.3a}$$

where

$$v_n^*(x_r, y_r, z_r) = v_c(z_r)\, e^{-\ln 2\,(x_r \sin\psi + (y_r - nd_r) \cos\psi + z_r \tan\Gamma)^2 \cos^2\Gamma/\delta^2}. \tag{2.3b}$$

[†] Experimentally, it is not practical to measure δ. Instead one measures the wake half-width as seen in the rotor-fixed coordinate system (x_r, y_r, z_r). The precise relationship between the measured half-width, say δ_m, and δ is difficult to ascertain. In this work, when utilizing the experimental data, it is assumed that the relationship between the two is simply $\delta = \delta_m \cos\psi$ where ψ is the rotor blade stagger angle shown in Fig. (2.1).

Note that, since the summation term in Eq. (2.3a) describes a pattern that is periodic in y_r, it can be transformed into a complex Fourier series by means of the Poisson sum formula (for a discussion see Carrier, Krook and Pearson (1966)) which states that for a suitable $f(n)$,

$$\sum_{n=-\infty}^{+\infty} f(n) = \sum_{j=-\infty}^{+\infty} \int_{-\infty}^{+\infty} f(n) \, e^{2\pi i j n} \, dn \ . \tag{2.4a}$$

Here n is regarded as a continuous variable rather than a discrete index on the right hand side of Eq. (2.4a). Setting $f(n) = v_n^*$, the integral on the right hand side of the Eq. (2.4a) can be evaluated by completing the squares in the exponent and using the known identity

$$\int_{-\infty}^{+\infty} e^{-x^2} \, dx = \pi^{1/2} \ . \tag{2.4b}$$

The result is

$$\sum_{n=-\infty}^{+\infty} v_n^*(x_r, y_r, z_r) = \frac{\pi^{1/2} \, \delta \, v_c(z_r)}{(\ln 2)^{1/2} \, d_r \, \cos\psi \, \cos\Gamma}$$

$$x \left[1 + 2 \sum_{j=1}^{+\infty} e^{-[j\pi\delta/(d_r \cos\psi \, \cos\Gamma)]^2} \, e^{2\pi i j (x_r \tan\psi + y_r + z_r \tan\Gamma/\cos\psi)/d_r} \right] \ . \tag{2.5}$$

The first term in the square bracket is the average of $\Sigma \, v_n^*$ taken over a period in the y_r direction. Since this is actually a small correction to the uniform mean flow, this term is absorbed in the uniform velocity U_r^*. Note that the evenness in the index j is utilized to simplify the expression.

17

Finally, the flow field can be written in the stator-fixed frame using the fact that the (x_r, y_r, z_r) and (x, y, z) coordinate systems are related through a Galilean transformation given by:

$$x_r = x + s \ ,$$

$$y_r = y - W_r \, t \ , \tag{2.6}$$

$$z_r = z$$

where s is the axial spacing between the rotor blade trailing edge and the stator vane leading edge. Noting that $U_\infty = U_r^* \cos\psi$ and $W_r = U_r^* \sin\psi$, one can write

$$\overrightarrow{U}_s(x,y,z,t) = \overrightarrow{U}_\infty + \overrightarrow{v}(x,y,z,t) \tag{2.7a}$$

where

$$\overrightarrow{U}_\infty = U_\infty \, \overrightarrow{e}_x \ , \qquad \overrightarrow{v} = v \left[\overrightarrow{e}_x \cos\psi - \overrightarrow{e}_y \sin\psi \right] \ , \tag{2.7b}$$

$$v(x,y,z,t) = \frac{2\pi^{1/2} \, \delta \, v_c(z)}{(\ln 2)^{1/2} \, d_r \, \cos\psi \, \cos\Gamma}$$

$$x \left[\sum_{j=1}^{+\infty} e^{-[j\pi\delta/(d_r \cos\psi \cos\Gamma)]^2} + 2\pi i j s \tan\psi \ e^{2\pi i j (x \tan\psi + y + z \tan\Gamma/\cos\psi - W_r \, t)/d_r} \right] . \tag{2.7c}$$

Eqs. (2.7) describe a superposition of a steady uniform mean flow and an unsteady small-amplitude disturbance which is convected by the mean flow. Note that the unsteady disturbance, or the convected gust, is expressed in terms of a time Fourier series with

18

index j describing the temporal harmonic of the gust whose frequency is $f_j = j\, W_r/d_r$. The blade-passing frequency (BPF) corresponds to $j = 1$. Thus, a typical temporal harmonic of the gust has the following general form[†]

$$\vec{v}_j(x,y,z,t) = \vec{B}_j(z)\, e^{i(k_x\, x + k_y\, y + k_z\, z - \omega_j\, t)} \tag{2.8a}$$

where

$$\omega_j = 2\pi j\, W_r/d_r \ ,$$

$$k_x = 2\pi j\, \tan\psi/d_r \ ,$$

$$k_y = 2\pi j/d_r \ , \tag{2.8b}$$

$$k_z = 2\pi j\, \tan\Gamma/(d_r\, \cos\psi) \ ,$$

$$\vec{B}_j(z) = \frac{2}{(\ln 2)^{1/2} d_r\, \cos\psi\, \cos\Gamma}\ \pi^{1/2}\ \delta\ v_c(z)\ e^{-[j\pi\delta/(d_r\, \cos\psi\, \cos\Gamma)]^2 + 2\pi ijs\tan\psi}$$

$$\times \left[\vec{e}_x\, \cos\psi - \vec{e}_y\, \sin\psi \right] \ . \tag{2.8c}$$

Note that, since U_∞ has no z-component, $\vec{U}_s(x,y,z,t)$ satisfies the no-flow condition through the channel walls. Furthermore, $\vec{B} \cdot \vec{k} = 0$ where $\vec{k} = (k_x, k_y, k_z)$ is the wavenumber vector, and hence the gust $\vec{v}(x,y,z,t)$ is solenoidal (i.e., $\nabla \cdot \vec{v} = 0$). Moreover, since $\vec{B}$ and $\vec{k}$ are perpendicular, the gust is a transverse wave.

[†] For comparison purposes, in the parametric calculations to be presented in the later chapters, the amplitude of the gust given by $B_j(z)$ in Eq. (2.8b) will be normalized by the momentum thickness of the rotor wake given by $\theta_w = \pi^{1/2}\, (1 - \sqrt{2}/2)\, \delta/((\ln 2)^{1/2}\, \cos\Gamma)$.

19

It will become clear in the next section that only the y-component of the gust, often called upwash, is responsible for noise generation. Fig. (2.3) shows a typical upwash pattern as predicted by Eqs. (2.8) for $\delta = 0.1$ and $\Gamma = 20$ degrees. These values are consistent with the experimental data of Shaw and Balombin (1981) who carried out detailed wake measurements at a distance of 1.23 rotor chord behind NASA ROTOR 55. This upwash pattern is used in the parametric calculations presented in later chapters.

2.2 Formulation of Acoustic Disturbance Equations

It was shown in the previous section that the rotor wake, when viewed in a stationary frame of reference, represents a convected gust. This gust is divergence-free and contains all of the fluid rotation or vorticity. The interaction of this vortical disturbance with the stator row generates small-amplitude pressure (and velocity) fluctuations that propagate through the compressible medium at the speed of sound relative to the fluid. These acoustic waves are irrotational.

Regarding air as a homogeneous perfect gas and neglecting the effects of viscosity and thermal conductivity on the propagation of sound, the fluid motion can be described by the inviscid flow equations which, in the absence of any sources, have the following form:

Momentum:
$$\rho \, \frac{D\vec{U}}{Dt} = - \nabla p \, , \tag{2.9a}$$

Continuity:
$$\frac{D\rho}{Dt} + \rho \, \nabla \cdot \vec{U} = 0 \, , \tag{2.9b}$$

Equation of State:
$$p = p(\rho, S_0) \, , \qquad S_0 = \text{constant} \tag{2.9c}$$

20
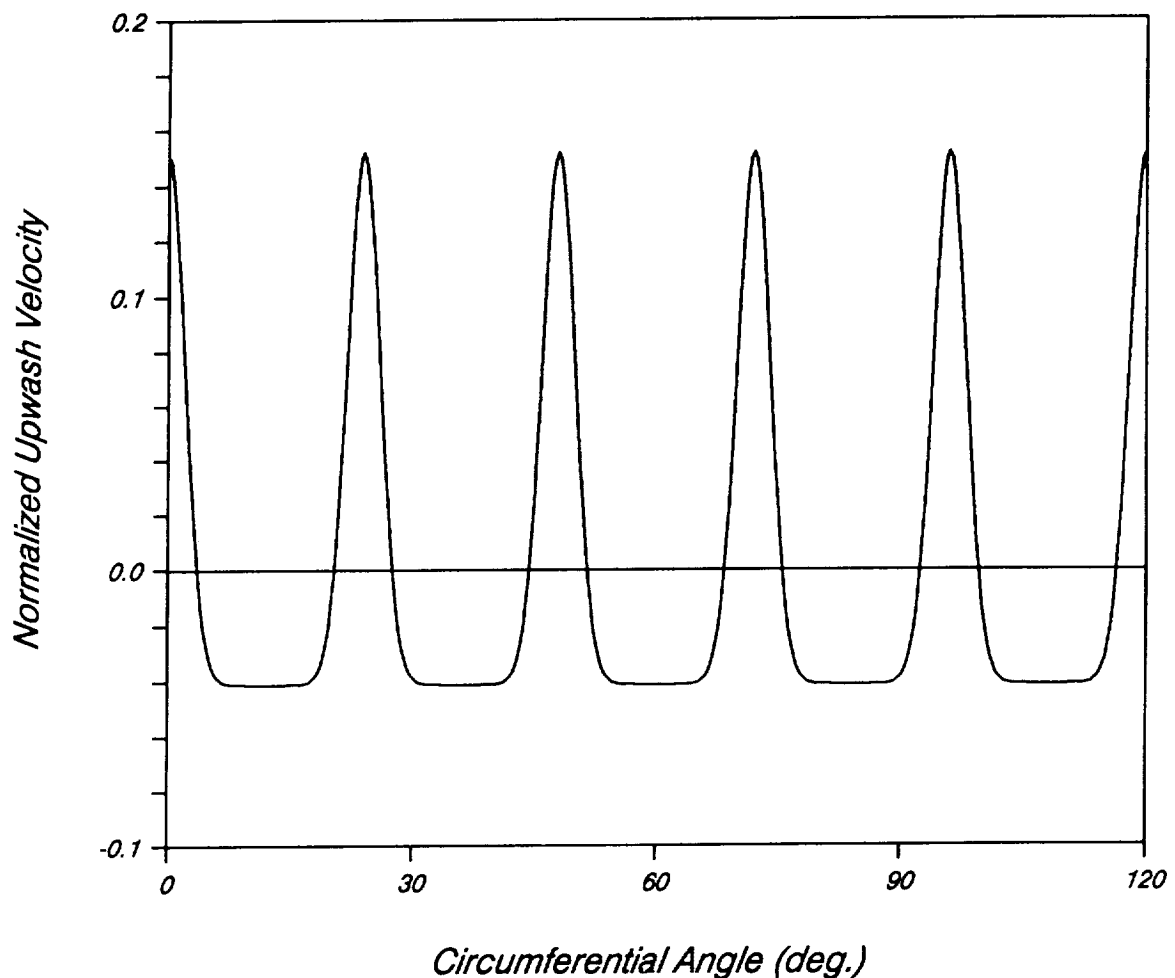
Fig. 2.3   Stator upwash velocity due to rotor viscous wake. (Model based on data of Shaw and Balombin (1981)).

where $D/Dt = \partial/\partial t + \vec{U} \cdot \nabla$ is the convective derivative which represents the time rate of change as seen by an observer moving with the flow. Here, $\vec{U}$ denotes the velocity, p the pressure, ρ the density, and S_0 the entropy of the fluid. These flow variables represent the total quantities which include the steady mean flow component and the small-amplitude disturbance component. Therefore, they can be written as

$$\vec{U}(x,y,z,t) = \vec{U}_\infty + \vec{u}'(x,y,z,t) , \qquad (2.10a)$$

$$p(x,y,z,t) = p_\infty + p'(x,y,z,t) , \qquad (2.10b)$$

$$\rho(x,y,z,t) = \rho_\infty + \rho'(x,y,z,t) \qquad (2.10c)$$

where the mean flow quantities are denoted by the subscript ∞ and the disturbance quantities are designated by a prime. As was mentioned earlier, for the purpose of the current study it is sufficient to consider the steady mean flow as spatially uniform. Moreover, it will be assumed that the stator vanes are thin and at small angle of attack to the oncoming mean flow. Since the steady perturbation to the uniform mean flow due to camber and angle of attack is small, it can be neglected to first order in examining the unsteady flow. Hence, effects of camber and angle of attack are ignored and the stator vanes are replaced with flat plates of "zero thickness" at zero angle to the mean flow. After inserting Eqs. (2.10) into Eqs. (2.9), neglecting the products of the small quantities, and noting that the uniform mean flow trivially satisfies the equations of motion, the following set of linearized equations is obtained:

$$\rho_\infty \frac{D_0\vec{u}'}{Dt} + \nabla p' = 0 , \qquad (2.11a)$$

$$\frac{D_0 \rho'}{Dt} + \rho_\infty \nabla \cdot \vec{u}' = 0 , \tag{2.11b}$$

$$p' = C_\infty^2 \rho' \tag{2.11c}$$

where

$$\frac{D_0}{Dt} = \frac{\partial}{\partial t} + U_\infty \frac{\partial}{\partial x} \tag{2.11d}$$

where C_∞ is the constant ambient speed of sound. Eq. (2.11c) is a consequence of the equation of the state and constancy of entropy.

Kovásznay (1953) showed that, for an isentropic flow, Eqs. (2.11) admit two types of unsteady small-amplitude disturbance solutions. The first type is convected by the mean flow. It is solenoidal (divergence-free) and has no pressure (and density) fluctuations associated with it. All of the fluid rotation or vorticity is connected with that type, and hence it is often called the vortical velocity disturbance. Now, since the rotor wake field $v(x,y,z,t)$ is convected by the mean flow and is solenoidal, it can be identified as (or more precisely can be written as a superposition of) the first type solution. Therefore, $v(x,y,z,t)$ satisfies

$$\frac{D_0 \vec{v}}{Dt} = 0 . \tag{2.12a}$$

The second type of solution of Eqs. (2.11) is irrotational (has zero curl) and contains all the pressure (and density) fluctuations. In the context of compressible flows it is referred to as an acoustic wave. It satisfies

$$\rho_\infty \frac{D_0 \vec{u}'_1}{Dt} + \nabla p' = 0 , \tag{2.12b}$$

23

$$\frac{D_0 \rho'}{Dt} + \rho_\infty \nabla \cdot \vec{u}_1' = 0 , \qquad (2.12c)$$

$$p' = C_\infty^2 \rho' . \qquad (2.12d)$$

Therefore, the most general solution to Eqs. (2.11) can be written as

$$\vec{u}'(x,y,z,t) = v(x,y,z,t) + \vec{u}_1'(x,y,z,t) . \qquad (2.13)$$

The appropriate boundary condition is that the total normal velocity must be vanish at solid boundaries. Thus,

$$\vec{n} \cdot \vec{u}_1'(x,y,z,t) = - \vec{n} \cdot \vec{v}(x,y,z,t) \qquad (2.14)$$

where $\vec{n}$ is the normal to the solid boundaries, i.e., the channel walls and vane surfaces. The radiation, or outgoing wave, condition applies at infinity. Therefore, while in the linear approximation the vortical and acoustic disturbances are independent solutions of the equations of motion, they are coupled together by the requirement that the total normal velocity must vanish at rigid surfaces. It is precisely this coupling that is responsible for the noise generation.

Now, since the acoustic disturbance is irrotational its velocity $\vec{u}_1'$ can be described by the gradient of a potential ϕ. Consequently, the linear version of the equation of motion requires the acoustic pressure p' to be related to ϕ in the following manner:

$$\vec{u}_1' = \nabla \phi \quad \rightarrow \quad p' = - \rho_\infty \frac{D_0 \phi}{Dt} . \qquad (2.15)$$

Upon multiplying Eq. (2.12c) by $\vec{u}_1$, applying divergence (i.e., $\nabla \cdot$) to Eq. (2.12b), noting that the convective derivative and the divergence operators commute, and eliminating all $\vec{u}_1$ and p' in terms of the velocity potential, the convected wave equation for ϕ is obtained which is given by

$$\frac{D_0^2 \phi}{Dt^2} - C_\infty^2 \nabla^2 \phi = 0 \qquad (2.16a)$$

subject to the boundary condition

$$\vec{n} \cdot \nabla \phi = - \vec{n} \cdot \vec{v}(x,y,z,t) \qquad (2.16b)$$

with the radiation condition applying at infinity.

The unit normal to surface of the stator is given by $\vec{e}_y$. Thus, on the surfaces of vanes the boundary condition given by Eq. (2.16b) can be rewritten as

$$\frac{\partial \phi}{\partial y} = - \vec{v} \cdot \vec{e}_y = - \sum_{j=1}^{+\infty} A_j(z) \, e^{i(k_x \, x \, + \, k_y \, y \, + \, k_z \, z \, - \, \omega_j \, t)} \qquad (2.17a)$$

where

$$A_j(z) = \vec{B}_j(z) \cdot \vec{e}_y = \frac{2\pi^{1/2} \, \delta \, v_c(z) \, \tan\psi}{(\ln 2)^{1/2} d_r \, \cos\Gamma} \, e^{-[j\pi\delta/(d_r \, \cos\psi \, \cos\Gamma)]^2 \, + \, 2\pi ijs\tan\psi} \ .$$

$$(2.17b)$$

Note that, as was mentioned at the end of the previous section, only the upwash component of the gust appears explicitly in Eq. (2.17a). Since $\vec{v} \cdot \vec{e}_z = 0$, the no-flow condition through the channel walls takes the form:

$$\frac{\partial \phi}{\partial z} \bigg|_{z=0,1} = 0 \ . \qquad (2.18)$$

Since Eq. (2.16a) is linear, each temporal harmonic component of the upwash can be considered separately. Then, let the variable ϕ_j represents the solution corresponding to the jth temporal harmonic component of the upwash.

25

Detailed experimental data on the wake radial variations are not available, and hence for convenience a linear variation for the centerline deficit velocity $v_c(z)$ is assumed which is given by:

$$v_c(z) = (1 - a/2 + az) . \tag{2.19}$$

The z dependence of the jth temporal harmonic component of the upwash in Eq. (2.17a) can then be expanded in an eigenfunction as follows:

$$(1 - a/2 + az) e^{ik_z z} = \sum_{m=0}^{+\infty} b_m \cos m\pi z \tag{2.20a}$$

where k_z is defined in Eq. (2.8b). The Fourier coefficient b_m is given by

$$b_m = \left[\frac{i (a/2 - 1) k_z}{k_z^2 - (m\pi)^2} + a \frac{k_z^2 + (m\pi)^2}{(k_z + m\pi)^2 (k_z - m\pi)^2} \right] [(-1)^m e^{ik_z} - 1]$$

$$- i a \left[\frac{k_z}{k_z^2 - (m\pi)^2} \right] (-1)^m e^{ik_z} . \tag{2.20b}$$

Again, utilizing the linearity of the differential equation, only the solution for a single upwash spatial mode m is developed. This single component of the solution is denoted by $\phi_{j,m}$. A summation over the spatial mode number m provides the total acoustic field corresponding to the jth temporal harmonic component of the upwash. The single component $\phi_{j,m}$ satisfies the convected wave equation

$$\frac{D_0^2 \phi_{j,m}}{Dt^2} - C_\infty^2 \nabla^2 \phi_{j,m} = 0 \tag{2.21a}$$

26

and the following boundary conditions. On stator vane surfaces:

$$\frac{\partial \phi_{j,m}}{\partial y} = b_m \, e^{2\pi i j s \tan\psi} \, e^{i(k_x \, x \, + \, k_y \, y \, - \, \omega_j \, t)} \cos m\pi z \, , \qquad (2.21b)$$

$$\left. \frac{\partial \phi_{j,m}}{\partial z} \right|_{z=0,1} = 0 \, . \qquad (2.21c)$$

Equations (2.21) may be simplified as follows. First, a Prandtl-Glauert transformation given by:

$$x' = x/\beta_\infty, \qquad y = y, \qquad z = z \, , \qquad (2.22a)$$

where

$$\beta_\infty = (1 - M_\infty^2)^{1/2}, \qquad M_\infty = U_\infty/C_\infty \qquad (2.22b)$$

is introduced. Here, M_∞ is the Mach number of the mean flow. Next, the harmonic time dependence in Eqs. (2.21) may be factored out. Finally, it is convenient to eliminate the first derivative with respect to x' by removing an additional x' dependent phase factor. Setting

$$\phi_{j,m}(x',y,z,t) = h_m(x',y,z) \, e^{-ik_x \left[M_\infty^2 \, x'/\beta_\infty \, + \, U_\infty t \right] + 2\pi i j s \tan\psi} \, , \qquad (2.23)$$

one obtains

$$\frac{\partial^2 h_m}{\partial x'^2} + \frac{\partial^2 h_m}{\partial y^2} + \frac{\partial^2 h_m}{\partial z^2} + k_x^2 \, \frac{M_\infty^2}{\beta_\infty^2} \, h_m = 0 \qquad (2.24a)$$

where the relation $\omega_j = k_x U_\infty$ from Eq. (2.8b) is utilized. Here, $k_x M_\infty/\beta_\infty$ is the reduced frequency. On the surfaces of the airfoils, the boundary condition is now given by

27

$$\frac{\partial h_m}{\partial y} = - b_m \, e^{i(k_x \, x'/\beta_\infty + k_y \, y)} \cos m\pi z \qquad (2.24b)$$

while on the channel walls it is

$$\frac{\partial h_m}{\partial z} \bigg|_{z=0,1} = 0 \, . \qquad (2.24c)$$

Recall that the radiation condition applies at infinity. Note that, Eq. (2.24a) is the Helmholtz equation for the modified acoustic disturbance velocity potential $h_m(x',y,z)$.

Eqs. (2.24) represent the final form of the governing equations for $h_m(x',y,z)$ corresponding to the mth spatial mode of the jth temporal harmonic component of the upwash. All necessary information about the sound field generated by the gust-airfoil interaction may be obtained from simple operations on $h_m(x',y,z)$. In the following chapters these equations are solved for the case of an isolated swept vane and then the results are utilized in constructing an approximate solution to the cascade problem.

CHAPTER 3

ANALYSIS FOR AN ISOLATED STATOR VANE

In this chapter, an approximate solution to the equations governing the modified acoustic velocity potential $h_m(x',y,z)$ for the case of a single vane interacting with a high-frequency (i.e., short-wavelength) harmonic convected gust is developed. This is the kernel solution which is utilized, in the next chapter, to construct the rotor-stator interaction noise model. A parametric study of the kernel solution is also presented.

In solving the governing equations (derived in the previous chapter), in addition to the usual approximations of linearized theory, two more approximations are introduced. The first one is a consequence of the high-frequency character of the gust. As was mentioned in the introduction, at high frequencies the airfoil unsteady response is dominated by the region near the leading edge. Therefore, one can calculate the leading-edge response as if the trailing edge were absent (i.e., making the chord semi-infinite). The solution then satisfies the exact boundary conditions upstream of the leading edge and on the airfoil, but violates the boundary condition downstream of the trailing edge. To obtain a correction for the trailing edge, the leading edge can then be assumed to extend to upstream infinity. This, of course, introduces an error upstream of the leading edge which can be corrected by solving yet another semi-infinite problem for the leading edge. The process of iterating between the edges can be continued indefinitely. For the case of a uniform mean flow Landahl (1958) showed that the resulting series converges for all disturbance wavelengths. Amiet (1976) showed that the airfoil unsteady lift is predicted to within ten percent accuracy by the first term in the series when the high-frequency parameter is greater than $\pi/4$. The appropriate high-frequency parameter here is defined

as kM_∞/β_∞^2, where k is the wavenumber, M_∞ the Mach number, and β_∞ was defined in the last chapter. This parameter is greater than $\pi/4$ for all cases considered in this study. Hence, in the present theory, the effects of the trailing edge on noise generation are neglected. A discussion of the second approximation used in this analysis is postponed until Section 3.2.

Consider the zeroth stator vane. The geometry and the orthogonal Prandtl-Glauert coordinate system (x',y,z) introduced in Chapter 2 are shown in Fig. (3.1). The vane is represented by a flat plate which lies in the plane y = 0 and spans the channel walls. The coordinate axis x' is in the direction of the uniform mean flow, y is perpendicular to the vane surface, and z is perpendicular to the channel walls. The airfoil leading edge is swept back at an angle α with respect to the z-axis. The trailing edge of the airfoil is shown as a dashed line since it will be ignored in this high-frequency analysis. The equations governing the acoustic field generated by the mth spatial mode of the jth temporal harmonic component of the gust upwash were derived in the previous chapter and are quoted here for an isolated stator vane. They are given by

$$\frac{\partial^2 h_m}{\partial x'^2} + \frac{\partial^2 h_m}{\partial y^2} + \frac{\partial^2 h_m}{\partial z^2} + k_x^2 \frac{M_\infty^2}{\beta_\infty^2} h_m = 0 \ , \qquad (3.1a)$$

$$\left. \frac{\partial h_m}{\partial y} \right|_{y=0} = -b_m \, e^{ik_x x'/\beta_\infty} \cos m\pi z \quad \text{on} \quad x' - (z \tan\alpha)/\beta_\infty > 0 \ , \qquad (3.1b)$$

$$\left. \frac{\partial h_m}{\partial z} \right|_{z=0,1} = 0 \qquad (3.1c)$$

where $x' - (z \tan\alpha)/\beta_\infty > 0$ in Eq. (3.1b) defines the airfoil surface. The constant b_m is given by Eq. (2.20b) of Chapter 2. Recall that Eqs. (3.1b&c) correspond to no-flow

(ξ, y, ζ): Nonorthogonal Coordinates
(x', y, z): Orthogonal Coordinates

ζ = Constant

α

ζ, x'

Leading Edge

Lower Channel Wall

α : Sweep Angle
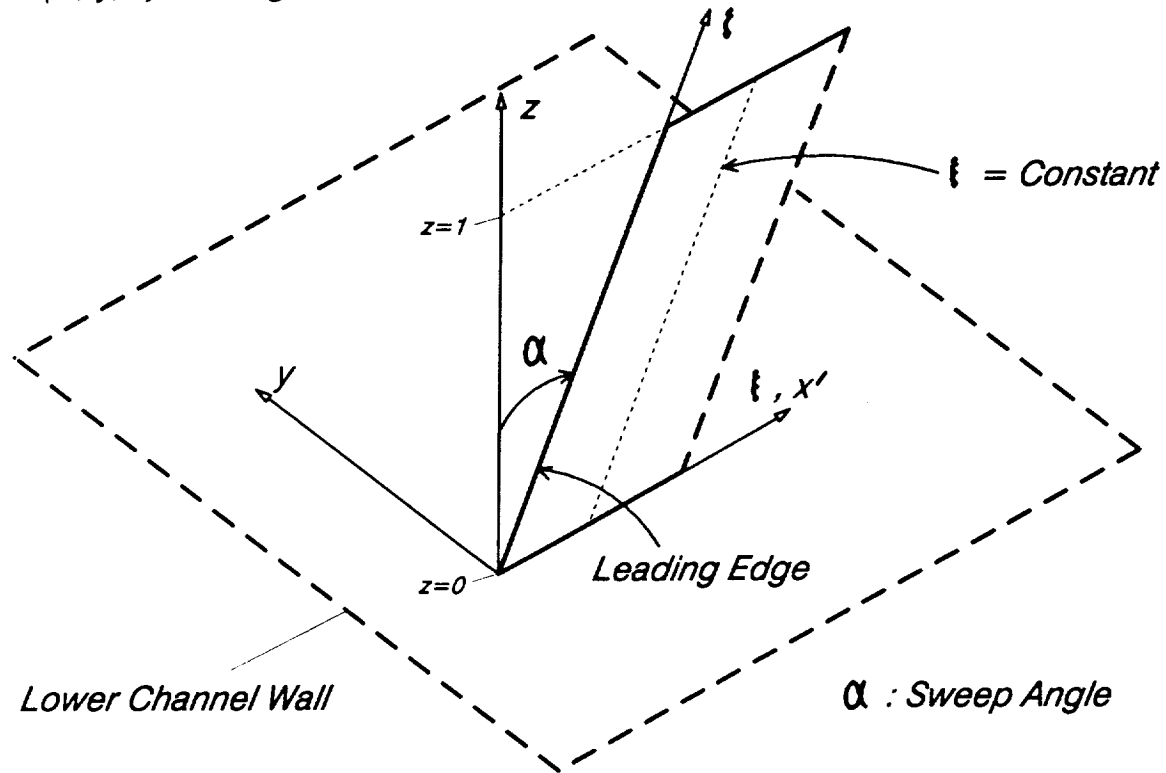
Fig. 3.1   Airfoil geometry and coordinate systems. The (x',y,z) system is orthogonal
            while the (ξ,y,ζ) system is nonorthogonal. The upper channel wall at z = 1 is
            not shown.

through the airfoil and channel walls, respectively. The radiation condition applies at infinity.

For the infinite span case, airfoil aligned coordinates are generally used to simplify the application of the boundary condition (3.1b). However, orthogonal airfoil aligned coordinates would complicate the additional wall boundary condition (3.1c) which occurs in the finite span case. Thus, a nonorthogonal coordinate system is chosen which is aligned with both the end walls and the airfoil leading edge (see Fig. (3.1)). Introducing

$$\xi = \sqrt{1 - \gamma^2} \; x' - \gamma \, z, \qquad y = y, \qquad \zeta = z \tag{3.2}$$

into Eqs. (3.1) yields

$$\frac{\partial^2 h_m}{\partial \xi^2} + \frac{\partial^2 h_m}{\partial \zeta^2} - 2\gamma \frac{\partial^2 h_m}{\partial \xi \partial \zeta} + \frac{\partial^2 h_m}{\partial y^2} + k_x^2 \; \frac{M_\infty^2}{\beta_\infty^2} \; h_m = 0 \; , \tag{3.3a}$$

$$\frac{\partial h_m}{\partial y} \bigg|_{y=0, \; \xi>0} = -b_m \, e^{i\kappa(\xi \, + \, \gamma\zeta)} \cos m\pi\zeta \; , \tag{3.3b}$$

$$\left(\frac{\partial h_m}{\partial \zeta} - \gamma \, \frac{\partial h_m}{\partial \xi} \right)_{\zeta=0,1} = 0 \tag{3.3c}$$

where

$$\gamma = \frac{\tan\alpha}{\sqrt{\beta_\infty^2 + \tan^2\alpha}} \qquad \kappa = \frac{k_x}{\beta_\infty \sqrt{1 - \gamma^2}} \; . \tag{3.3d}$$

The transformation has slightly complicated the differential operator, but the boundary condition (3.3b) now applies for $\xi > 0$.

The partial differential equation (3.3a) is second order, and hence $h_m(\xi,y,\zeta)$ and its first derivatives must be continuous everywhere except (possibly) across the airfoil surface (i.e., $\xi < 0$, $y = 0^\pm$). Therefore, $h_m(\xi,0^+,\zeta) = h_m(\xi,0^-,\zeta)$ for $\xi < 0$. On the other hand, upon applying the simple transformation $y \rightarrow -y'$ to Eqs. (3.3), it can be seen that the boundary condition (3.3b) implies that $h_m(\xi,y,\zeta)$ is an odd function of y. Thus, $h_m(\xi,0^+,\zeta) = -h_m(\xi,0^-,\zeta)$. These results taken together yield

$$h_m \bigg|_{y=0, \ \xi<0} = 0 \qquad\qquad (3.3e)$$

Now, if either $h_m(\xi,0,\zeta)$ or $\partial h_m(\xi,0,\zeta)/\partial y$ were known for all ξ, the solution to Eqs. (3.3) could be obtained by a straightforward application of a Fourier transform in the ξ direction. However, Eqs. (3.3) describe a mixed boundary value problem, since $h_m(\xi,0,\zeta)$ is known only for $\xi < 0$ while $\partial h_m(\xi,0,\zeta)/\partial y$ is known only for $\xi > 0$. The Wiener-Hopf technique, which combines transform methods with analytic continuation arguments in the complex plane of the transform variable, is applicable to mixed boundary value problems. A detailed exposition of the method may be found in Noble (1958).

The Wiener-Hopf technique is now applied to Eqs. (3.3). First, a Fourier transform is applied in the ξ direction;

$$H_m(\lambda,y,\zeta) = (2\pi)^{-1/2} \int_{-\infty}^{+\infty} h_m(\xi,y,\zeta) \, e^{i\lambda\xi} \, d\xi \ . \qquad\qquad (3.4a)$$

In standard Wiener-Hopf nomenclature

$$H_m^+(\lambda,y,\varsigma) = (2\pi)^{-1/2} \int_0^{+\infty} h_m(\xi,y,\varsigma)\, e^{i\lambda\xi}\, d\xi \;, \tag{3.4b}$$

$$H_m^-(\lambda,y,\varsigma) = (2\pi)^{-1/2} \int_{-\infty}^0 h_m(\xi,y,\varsigma)\, e^{i\lambda\xi}\, d\xi \;. \tag{3.4c}$$

Here the superscripts refer to the regions of analyticity in the complex λ-plane. Assuming that for given y and ς, $|h_m(\xi,y,\varsigma)| < c_1\, e^{-\delta_1\xi}$ as $\xi \to +\infty$, and $|h_m(\xi,y,\varsigma)| < c_2\, e^{\delta_2\xi}$ as $\xi \to -\infty$, where c_1, c_2, $\delta_1 > 0$, and $\delta_2 > 0$ are constants, the following statements can be made regarding the regions of analyticity. The integral in Eq. (3.4b) converges for all values of λ such that $\mathrm{Im}(\lambda) > -\delta_1$, and hence $H_m^+(\lambda,y,\varsigma)$ is analytic (i.e., free of singularities) in the upper half-plane defined by $\mathrm{Im}(\lambda) > -\delta_1$. Similarly, $H_m^-(\lambda,y,\varsigma)$, defined by Eq. (3.4c), is analytic in the lower half-plane defined by $\mathrm{Im}(\lambda) < \delta_2$. Functions which are analytic in the upper or lower half planes are called "plus" or "minus" functions, respectively.

Equations (3.3a&c) are now transformed to obtain

$$\frac{\partial^2 H_m}{\partial\varsigma^2} + 2i\gamma\lambda\frac{\partial^2 H_m}{\partial\varsigma} + \frac{\partial^2 H_m}{\partial y^2} - \left[\lambda^2 - k_x^2\frac{M_\infty^2}{\beta_\infty^2}\right] H_m = 0 \;, \tag{3.5a}$$

$$\left(\frac{\partial H_m}{\partial\varsigma} + i\gamma\lambda H_m\right)_{\varsigma=0,1} = 0 \;. \tag{3.5b}$$

Next, consider the Fourier transform of Eq. (3.3b). Since $\partial h_m(\xi,0,\varsigma)/\partial y$ is not known for $\xi < 0$, it may be represented by $d(\xi,\varsigma)$, given by:

34

$$d_m(\xi,\zeta) = \begin{cases} \dfrac{\partial h_m}{\partial y}\bigg|_{y=0} & \xi < 0 \\[2em] 0 & \xi > 0 \end{cases} \tag{3.5c}$$

Now, upon transforming Eq. (3.3b), one can write

$$\frac{\partial H_m}{\partial y}\bigg|_{y=0} = D_m^-(\lambda,\zeta) - i(2\pi)^{-1/2} b_m \frac{e^{i\gamma(\lambda + \kappa)\zeta} \cos m\pi\zeta}{(\lambda + \kappa)} \tag{3.5d}$$

where $D_m^-(\lambda,\zeta)$ is the Fourier transform of $d_m(\xi,\zeta)$ and, in accordance with the convention defined by Eq. (3.4c), is analytic in the lower half of the complex λ-plane. Here, to produce convergence of the Fourier transform integral, it is assumed that κ has a small positive imaginary part ϵ. At the conclusion of the analysis ϵ will be allowed to approach zero.

Note that Eq. (3.5a) is separable in y and ζ, and that Eq. (3.5b) has no explicit dependence on y. Setting $H_m(\lambda,y,\zeta) = Y(\lambda,y) Z(\lambda,\zeta)$ and substituting in Eqs. (3.5a&b) one finds

$$\frac{d^2Y}{dy^2} - \left[\lambda^2 - k_x^2 \frac{M_\infty^2}{\beta_\infty^2} + \chi^2\right] Y = 0 , \tag{3.6a}$$

$$\frac{d^2Z}{d\zeta^2} + 2i\gamma\lambda \frac{dZ}{d\zeta} + \chi^2 Z = 0 \tag{3.6b}$$

subject to

$$\left(\frac{dZ}{d\zeta} + i\gamma\lambda Z\right)_{\zeta=0,1} = 0 \tag{3.6c}$$

where χ is the separation constant. Eqs. (3.6b&c) define an eigenvalue problem for $Z(\lambda,\zeta)$. Upon solving the eigenvalue problem, the eigenvalues are found to be $\chi = n\pi$, $n = 0,1,2,\cdots$. The corresponding eigenfunctions are given by

$$Z_n(\lambda,\zeta) = e^{-i\gamma\lambda\zeta}\cos n\pi\zeta \ . \tag{3.7a}$$

For complex λ, the differential operator in Eq. (3.6b) is non-Hermitian (i.e., it is not equal to the complex conjugate of its adjoint). Then, there exists a set of biorthogonal eigenfunctions (see Morse and Feshbach (1953))

$$\tilde{Z}_\ell(\lambda,\zeta) = e^{-i\gamma\lambda^*\zeta}\cos\ell\pi\zeta \tag{3.7b}$$

which satisfy the orthogonality condition

$$\int_0^1 Z_n(\lambda,\zeta)\,\tilde{Z}_\ell^*(\lambda,\zeta)\,d\zeta = \begin{cases} 1/2, & \text{if} \quad n = \ell \\ 0\,, & \text{if} \quad n \neq \ell \\ 1\,, & \text{if} \quad n = \ell = 0 \end{cases} \tag{3.7c}$$

where the asterisk denotes the complex conjugate.

The solution to the remaining equation (i.e., Eq. (3.6a)) is straightforward. Combining the results in an eigenfunction expansion and noting the antisymmetry of $H_m(\lambda,y,\zeta)$, one finds

36

$$H_m(\lambda,y,\zeta) = \text{sgn}(y) \sum_{n=0}^{+\infty} C^+_{m,n}(\lambda) \, Y_n(y) \, Z_n(\zeta) \qquad (3.8a)$$

where

$$Y_n(\lambda,y) = e^{-|y| \, \sqrt{1-\gamma^2} \, \sqrt{\lambda^2 - W_n^2}} \, , \qquad (3.8b)$$

$$W_n^2 = \left[\frac{(k_x M_\infty/\beta_\infty)^2 - (n\pi)^2}{1-\gamma^2} \right] , \qquad (3.8c)$$

and the $C^+_{m,n}(\lambda)$ are functions that must be determined by further analysis. The analyticity of $C^+_{m,n}(\lambda)$ follows from the condition that $h_m(\xi,0,\zeta) = 0$ for $\xi < 0$ (see Eq. (3.3e)). Note that $Y_n(\lambda,y)$ has two branch points at $\lambda = \pm W_n$. The radiation (outgoing wave) condition at infinity is satisfied by a proper choice of branch cuts of W_n to be shown later. $C_{m,n}(\lambda)$ may now be determined as follows.

Substituting the eigenfunction expansion representation for $H_m(\lambda,y,\zeta)$ in Eq. (3.5d) and applying the orthogonality property (i.e. Eq. (3.7c)), one finds

$$-\sqrt{1-\gamma^2} \, \sqrt{\lambda^2 - W_n^2} \, C^+_{m,n}(\lambda) = D^-_{m,n}(\lambda) - \frac{\epsilon_{m,n} \, b_m}{(2\pi)^{1/2}} \frac{E_{m,n}(\lambda)}{(\lambda + \kappa)} \qquad (3.9a)$$

where

$$E_{m,n}(\lambda) = \frac{p \, [2p^2 - (m-n)^2\pi^2 - (m+n)^2\pi^2] \, [(-1)^{(m+n)} e^{ip} - 1]}{2 \, [p^2 - (m+n)^2\pi^2] \, [p^2 - (m-n)^2\pi^2]} \, , \qquad (3.9b)$$

37

$$p = \gamma(\lambda + \kappa), \qquad \epsilon_{m,n} = \begin{cases} 1, & \text{for } n = m \\ \\ 2, & \text{for } n \neq m \end{cases} \tag{3.9c}$$

Note that the apparent poles in the denominator of $E_{m,n}(\lambda)$ are cancelled by zeros in the numerator. Hence, $E_{m,n}(\lambda)$ is an entire function of λ. The $D_{m,n}^-(\lambda)$'s are the unknown coefficients in the eigenfunction expansion of $D_m^-(\lambda,\zeta)$, i.e.,

$$D_m^-(\lambda,\zeta) = \sum_{n=0}^{+\infty} D_{m,n}^-(\lambda)\, Z_{m,n}(\lambda,\zeta) \ . \tag{3.9d}$$

The function $\sqrt{\lambda^2 - W_n^2}$ is a mixed function since, it has singularities (i.e., branch points) in both half-planes.

The Wiener-Hopf technique basically consists of rearranging Eq. (3.9a) such that one side is analytic in the upper half of the λ-plane while the other side is analytic in the lower half of the λ-plane. The two sides are equal in a common strip of analyticity and thus, are the analytic continuation of each other. Hence, they represent an entire function, say $J(\lambda)$, in the complex λ-plane. This entire function can often be deduced with the aid of Liouville's theorem (see Noble (1958)) which states that the most general bounded entire function is a constant. To apply Liouvillle's theorem, the edge conditions (i.e., the physical constraints on the flow very near the leading edge) are utilized to determine the behavior of the plus and minus sides of the Wiener-Hopf equation as λ approaches infinity. Often, the edge conditions show that both the plus and minus sides of the Wiener-Hopf equation

approach zero as $|\lambda| \to \infty$ in the respective half planes. By Liouville's theorem, the entire function must then be identically zero.

To implement the technique, first, both sides of Eq. (3.9a) are divided by $\sqrt{\lambda + W_n}$. This yields

$$-\sqrt{1 - \gamma^2} \sqrt{\lambda + W_n} \ C^+_{m,n}(\lambda) = \frac{D^-_{m,n}(\lambda)}{\sqrt{\lambda - W_n}} - \frac{\epsilon_{m,n} \ b_m}{(2\pi)^{1/2}} \frac{E_{m,n}(\lambda)}{\sqrt{\lambda - W_n} \ (\lambda + \kappa)} \ . \qquad (3.10)$$

The locations of branch points (and their corresponding branch cuts), poles, and the common strip of analyticity in the complex plane are shown in Fig. (3.2). The left hand side of Eq. (3.10) is a plus function while the first term on the right hand side is a minus function. For $m = n$ the last term is a mixed function. It is interesting to note that for $m \neq n$ this term is a minus function.

As was mentioned earlier, the edge conditions determine the form of the entire function $J(\lambda)$. The flow near the leading edge is required to behave locally as irrotational and incompressible. For the case of zero sweep, one finds that

$$h_m(\xi,0,\zeta) \propto \xi^{1/2} \cos m\pi\zeta \qquad \text{as} \qquad \xi \to 0^+ \qquad (3.11a)$$

and

$$\frac{\partial}{\partial y} h_m(\xi,0,\zeta) \propto \xi^{-1/2} \cos m\pi\zeta \qquad \text{as} \qquad \xi \to 0^- \ . \qquad (3.11b)$$

Note that for the unswept case the two coordinate systems (ξ,y,ζ) and (x',y,z) are identical (see Eq. (3.2)). The exponents on ξ correspond to a locally two-dimensional flow around the sharp leading edge. The introduction of sweep does not change the local two-dimensional behavior over the central portion of the span. However, when sweep is
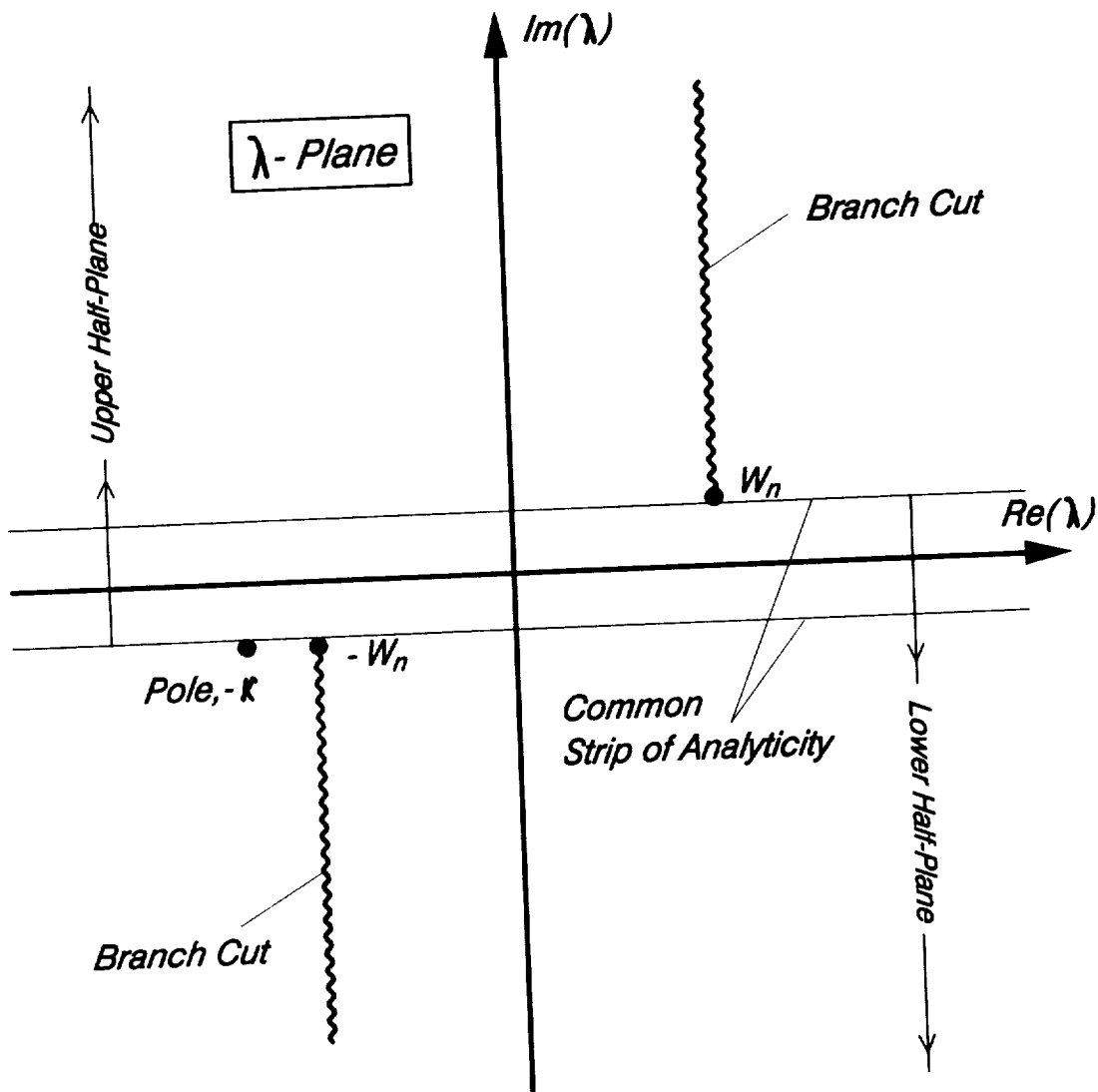
Fig. 3.2   Location of singularities and common strip of analyticity in the complex λ-plane.

present, the flow becomes highly three dimensional very near the end walls. In Appendix A it is shown that for a given sweep angle, at $\zeta = 0$, $h_m(\xi,0,0) \propto \xi^{\mu_0}$ where $0 < \mu_0 < 1/2$, while at $\zeta = 1$, $h_m(\xi,0,1) \propto \xi^{\mu_1}$ where $1/2 < \mu_1 < 1$. The details of the transition from the near wall behavior to that of the central portion of the span are not known, but it seems reasonable to expect a dependence of the form (for a discussion see Appendix A):

$$h_m(\xi,0,\zeta) \propto \xi^{\mu(\zeta)} F(\zeta) \qquad \text{as} \qquad \xi \to 0^+ \qquad (3.12a)$$

and

$$\frac{\partial}{\partial y} h_m(\xi,0,\zeta) \propto \xi^{\mu(\zeta)-1} G(\zeta) \qquad \text{as} \qquad \xi \to 0^- \qquad (3.12b)$$

where the transition from the value $\mu = 1/2$ to the wall values occurs over "boundary layers" near each wall. The qualitative behavior of μ as a function of ζ for different sweep angles is shown in Fig. (3.3).

Now, consider the behavior of $C^+_{m,n}(\lambda)$ and $D^-_{m,n}(\lambda)$ as λ approaches infinity in the upper and lower half planes, respectively. From Eqs. (3.8a) and (3.9d), one can write

$$C^+_{m,n}(\lambda) = (2\pi)^{-1/2} \int_0^1 \left[\int_0^{+\infty} h_m(\xi,0,\zeta) \, e^{i\lambda\xi} \, d\xi \right] e^{i\gamma\lambda\zeta} \cos n\pi\zeta \, d\zeta , \qquad (3.13a)$$

$$D^-_{m,n}(\lambda) = (2\pi)^{-1/2} \int_0^1 \left[\int_{-\infty}^0 \frac{\partial}{\partial y} h_m(\xi,0,\zeta) \, e^{i\lambda\xi} \, d\xi \right] e^{i\gamma\lambda\zeta} \cos n\pi\zeta \, d\zeta . \qquad (3.13b)$$

For complex λ in the appropriate half planes, the factor $e^{i\lambda\xi}$ decays exponentially with increasing $|\xi|$ with the decay rate depending on the magnitude of λ. Clearly, for sufficiently large λ, the integrals in Eqs. (3.13) are dominated by the regions near $\xi = 0$

41
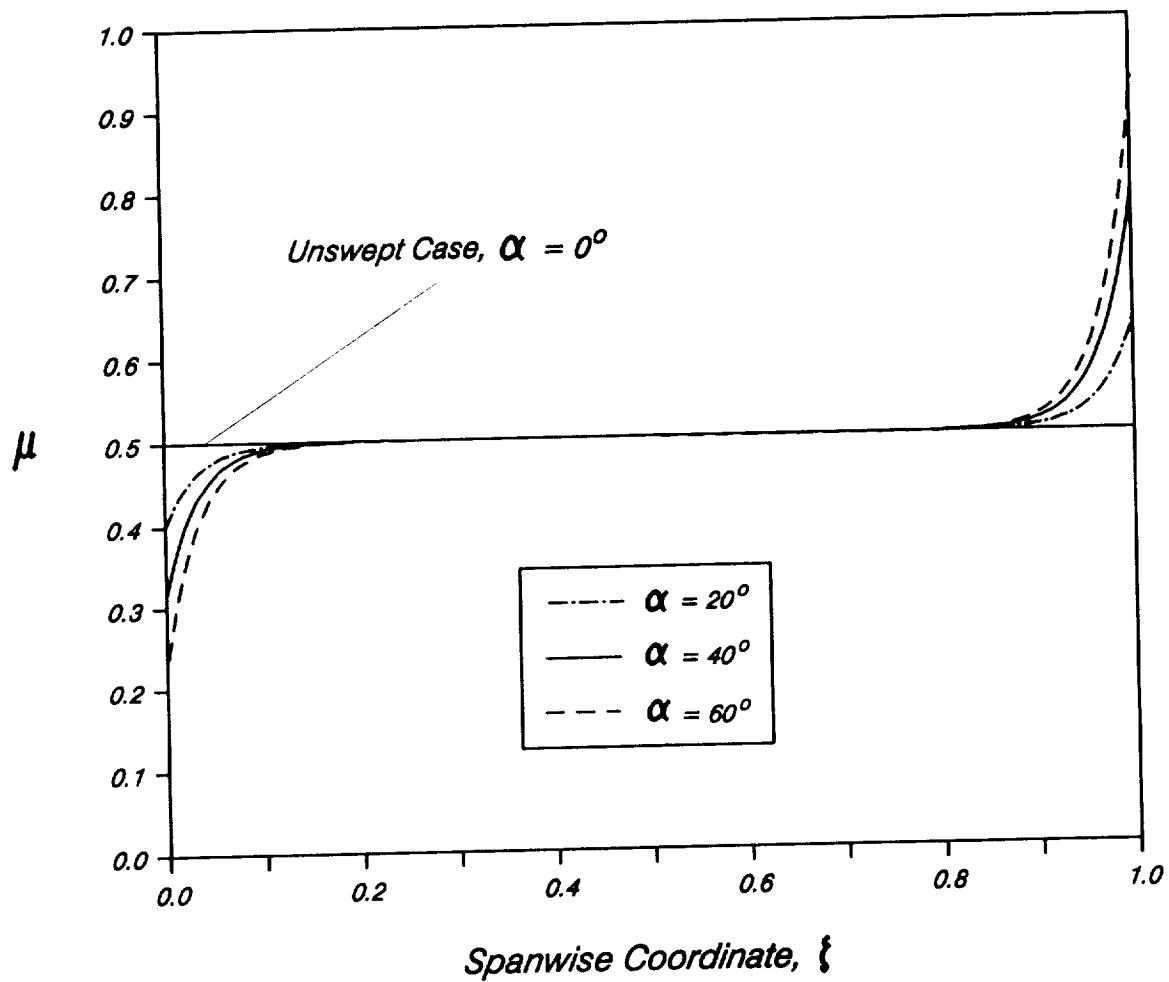
Fig. 3.3   Qualitative variations of μ with spanwise coordinate ς for different sweep angles α.

42

where $h_m(\xi,0,\zeta)$ and $\partial h_m(\xi,0,\zeta)/\partial y$ can be approximated by Eqs. (3.12). Then, the asymptotic behavior of the Fourier transform integral in Eqs. (3.13) as $|\xi| \to 0$ can be estimated using Abelian theorems (see, for example Noble (1958)). After the asymptotic behavior of these equations for $|\xi| \to 0$ is obtained, the integral over ζ can be evaluated using integration by parts. The final results are given below. As $|\lambda| \to \infty$ in the upper half plane

$$C^+_{m,n}(\lambda) \propto \lambda^{-2-\mu_0} F(0) + \text{H.O.T.} \tag{3.14a}$$

and as $|\lambda| \to \infty$ in the lower half-plane

$$D^-_{m,n}(\lambda) \propto \lambda^{-1-\mu_1} e^{i\gamma\lambda} G(1) + \text{H.O.T.} \tag{3.14b}$$

where μ_0 and μ_1 are the values of μ in the vicinity of the lower and upper walls, respectively. Note that $C^+_{m,n}(\lambda)$ is algebraically small in the upper half while $D^-_{m,n}(\lambda)$ is exponentially large in the lower half of the complex λ-plane. The expressions given by Eqs. (3.14) are fairly crude estimates of the asymptotic behavior of $C^+_{m,n}(\lambda)$ and $D^-_{m,n}(\lambda)$. However, they are adequate for present purposes.

In most applications of the Wiener-Hopf technique, the functions involved behave algebraically at infinity and hence Liouville's theorem can be utilized to ascertain the form of $J(\lambda)$. Some of the complex functions appearing in Eq. (3.10) however, behave non-algebraically as $|\lambda| \to \infty$. In fact, the function on the left hand side decays algebraically at infinity in the upper half of the λ-plane while the functions appearing on the right hand side increase exponentially at infinity in the lower half of the λ-plane. The presence of exponential functions in Eq. (3.10) in turn means that $J(\lambda)$ must be exponential. Unfortunately, there does not exist a general theorem analogous to Liouville's to specify

43

the form of an exponential $J(\lambda)$. Consequently, using the available theory it is not possible to derive the exact solution to Eq. (3.10). However, before proceeding to present an approximate solution to that equation, an approach is described, in Section 3.1, which leads to a representation of the exact solution in terms of an infinite number of unknown constants. Then, in Section 3.2, an approximate solution to Eq. (3.10) is developed which will be utilized in the next chapter to construct the cascade model.

3.1 A Representation of the Exact Solution of Eq. (3.10)

In this section, an approach that leads to a representation of the exact solution of Eq. (3.10) in terms of an infinite number of unknown constants is described. Detailed derivations of the results presented in this section are included in Appendix B. The approach involves a modification of the standard Wiener-Hopf technique to overcome the difficulty due to exponential behavior at infinity. At the end of this section a summary of conclusions regarding the problem of indeterminacy of the unknown constants that arise and an explanation for the cause of the difficulty are presented.

In order to avoid excessive algebra, and without loss of generality, it is assumed that $m = 0$. Therefore, the results obtained in this section represent the acoustic field generated by the interaction of a single stator vane with the zeroth mode of the oncoming gust (i.e., a plane wave gust). For this case, Eq. (3.10) reduces to

$$-\sqrt{1 - \gamma^2} \sqrt{\lambda + W_n} \, C_h^+(\lambda) = \frac{D_n^-(\lambda)}{\sqrt{\lambda - W_n}} - \frac{\epsilon_n \, b_o}{(2\pi)^{1/2} \, \gamma} \frac{E_n(\lambda)}{\sqrt{\lambda - W_n} \, (\lambda + \kappa)} \qquad (3.15a)$$

where

$$E_n(\lambda) = \frac{(\lambda + \kappa) [(-1)^n e^{i\gamma(\lambda + \kappa)} - 1]}{(\lambda + \kappa - n\pi/\gamma)(\lambda + \kappa + n\pi/\gamma)}$$ (3.15b)

and where, for ease of writing, reference to index $m = 0$ is dropped. The estimates for the behavior at infinity of $C_n^+(\lambda)$ and $D_n^-(\lambda)$ are given by Eqs. (3.14).

In order to solve Eq. (3.15a) using the Wiener-Hopf technique, the exponential behavior at infinity must be circumvented. This is done by dividing both sides of the equation by an appropriate function such that the resulting equation exhibits algebraic behavior at infinity, and hence becomes amenable to the application of Liouville's theorem. The divisor function must behave algebraically in the upper half-plane and be exponentially large in the lower half-plane. Several choices of the divisor function are explored.

First consider the divisor function

$$Q_1(\lambda) = [(-1)^n e^{i\gamma(\lambda + \kappa)} - 1].$$ (3.16a)

This function has the required behavior at infinity, but it has an infinite number of zeros in the lower half-plane located at $\lambda_j = -\kappa + (2j - n)\pi/\gamma$ (recall that κ has a small positive imaginary part). Dividing Eq. (3.15a) by $Q_1(\lambda)$, yields

$$-\frac{\sqrt{1 - \gamma^2} \sqrt{\lambda + W_n} \; C_n^+(\lambda)}{[(-1)^n e^{i\gamma(\lambda + \kappa)} - 1]} = \frac{D_n^-(\lambda)}{\sqrt{\lambda - W_n} \; [(-1)^n e^{i\gamma(\lambda + \kappa)} - 1]}$$

$$-\frac{\epsilon_n \, b_0}{(2\pi)^{1/2} \, \gamma} \frac{1}{\sqrt{\lambda - W_n} \; (\lambda + \kappa - n\pi/\gamma)(\lambda + \kappa + n\pi/\gamma)}.$$ (3.16b)

The term on the left hand side of Eq. (3.16b) remains a plus function while the first term on the right-hand side has now become a mixed function. The last term in the equation remains a mixed function. In order to separate the equation into plus and minus functions,

45

additive splits of the mixed terms are required. This is easily achieved by the use of the Cauchy's integral formula. After rearranging the equation into plus and minus sides and utilizing the edge conditions, the entire function $J(\lambda)$ is found to be identically zero. Setting the plus and minus sides of the equation separately to zero and solving for $C_n^+(\lambda)$ and $D_n^-(\lambda)$, (see Appendix B), one finds that

$$C_n^+(\lambda) = \frac{i[(-1)^n e^{i\gamma(\lambda + \kappa)} - 1]}{\sqrt{1 - \gamma^2}\ \sqrt{\lambda + W_n}}$$

$$\left\{ \gamma^{-1} \sum_{j=-\infty}^{+\infty} \frac{D_n^-(\lambda_j)}{\sqrt{\lambda_j - W_n}\ (\lambda - \lambda_j)} + \frac{\epsilon_n b_0}{(2\pi)^{3/2}\ n} \right.$$

$$\left. \times \left[\frac{1}{\sqrt{\kappa + W_n - n\pi/\gamma}\ (\lambda + \kappa - n\pi/\gamma)} - \frac{1}{\sqrt{\kappa + W_n + n\pi/\gamma}\ (\lambda + \kappa + n\pi/\gamma)} \right] \right\} \ , \quad (3.16c)$$

$$D_n^-(\lambda) = -\sqrt{\lambda - W_n}\ [(-1)^n e^{i\gamma(\lambda + \kappa)} - 1]$$

$$\times \left\{ i\gamma^{-1} \sum_{j=-\infty}^{+\infty} \frac{D_n^-(\lambda_j)}{\sqrt{\lambda_j - W_n}\ (\lambda - \lambda_j)} \right.$$

$$- \frac{\epsilon_n b_0}{(2\pi)^{1/2}\ \gamma}\ \frac{1}{\sqrt{\lambda - W_n}\ (\lambda + \kappa - n\pi/\gamma)\ (\lambda + \kappa + n\pi/\gamma)} + \frac{i\epsilon_n b_0}{(2\pi)^{3/2} n}$$

$$\left. \times \left[\frac{1}{\sqrt{\kappa + W_n - n\pi/\gamma}\ (\lambda + \kappa - n\pi/\gamma)} - \frac{1}{\sqrt{\kappa + W_n + n\pi/\gamma}\ (\lambda + \kappa + n\pi/\gamma)} \right] \right\} \ . \quad (3.16d)$$

The unknown constants $D_n^-(\lambda_j)$ represent the values of the unknown function $D_n^-(\lambda)$ at λ_j. Therefore, the expressions given by Eqs. (3.16c&d) are implicit representations of the required solution. In order to obtain an explicit solution, the values of these unknown constants must be determined.

A similar situation involving unknown constants arises when the Wiener-Hopf technique is used to solve a general class of problems known as the three-part boundary value problems. In such problems, boundary conditions are specified on three different parts of the boundary, say, on $-\infty < x < 0$, $0 \le x \le x_0$, and $x_0 < x < +\infty$ in three different forms. An example of a three-part boundary value problem is wave diffraction by a thick plate (Jones (1953)). In a typical three-part boundary value problem the unknown constants are related to physical quantities in the problem. Methods have been developed to find the approximate values of such unknown constants in certain frequency limits. In most cases an infinite set of algebraic equations for the $D(\lambda_j)$ can be found by evaluating Eq. (3.16d) at $\lambda = \lambda_j$. Solution of a suitably truncated version of the resulting system of linear algebraic equations then yields approximate values for a desired number of unknown constants.

Despite the fact that the present problem is not a conventional three-part boundary value problem, the two corners at $x' = 0$ ($\zeta = 0$) and $x' = x_0' = (\tan\alpha)/\beta_\infty$ ($\zeta = 1$) can be regarded as the analogues of the two junctions in a three-part boundary value problem. Unfortunately, evaluation of Eqs. (3.16c&d) at points $\lambda = \lambda_j$ leads to simple identities rather than a system of algebraic equations for the unknown constants, and hence no information on the values $D_n(\lambda_j)$ is obtained. Thus, here the problem of evaluating the unknown constants is attacked using an alternative approach. Relying on the uniqueness of the solution, alternative representations for $C_n^+(\lambda)$ and $D_n^-(\lambda)$ are sought which are then

equated with the ones given by Eqs. (3.16c&d) to discern some information regarding the unknown constants $D_n^-(\lambda_j)$.

Before proceeding to find alternative representations for $C_n^+(\lambda)$ and $D_n^-(\lambda)$, it is instructive to reexamine the behavior of $C_n^+(\lambda)$ and $D_n^-(\lambda)$ for large λ. According to Eqs. (3.16c&d), the dominant asymptotic behavior of $C_n^+(\lambda)$ and $D_n^-(\lambda)$ is given by

$$C_n^+(\lambda) \propto \lambda^{-3/2} , \qquad D_n^-(\lambda) \propto \lambda^{-1/2} e^{i\gamma\lambda} \qquad (3.17)$$

as $|\lambda| \to \infty$ in the upper and lower lower half-planes, respectively. Comparing Eqs. (3.14) and (3.17), it is seen that the crude approximations found earlier captured the correct exponential behavior, but produced a different algebraic exponent. The new asymptotic estimates given by Eq. (3.17) are self-consistent with all the steps in the derivation of Eqs. (3.16c&d), and hence they will be used in the remainder of the analysis.

Alternative representations for $C_n^+(\lambda)$ and $D_n^-(\lambda)$ have been found utilizing different divisor functions

$$Q_2(\lambda) = \frac{[(-1)^n e^{i\gamma(\lambda + \kappa)} - 1]}{(\lambda + \kappa + n\pi/\gamma)} , \qquad (3.18)$$

$$Q_3(\lambda) = \frac{[(-1)^n e^{i\gamma(\lambda + \kappa)} - 1]}{(\lambda + \kappa - n\pi/\gamma)} , \qquad (3.19)$$

and following a procedure similar to the one used to derive Eqs. (3.16c&d) (for details see Appendix B). These alternative representations involve constant K_1 and K_2 in addition to $D_n^-(\lambda_j)$. Upon equating these different representations for $C_n^+(\lambda)$ and $D_n^-(\lambda)$, one finds a relation involving the unknown constants $D^-_n(\lambda_j)$. This relation is given by

$$\sum_{j=-\infty}^{+\infty} \frac{D_n^-(\lambda_j)}{\sqrt{\lambda_j - W_n}} = \frac{\epsilon_n b_0}{(2\pi)^{3/2} \gamma} \left[\frac{1}{\sqrt{\kappa + W_n + n\pi/\gamma}} - \frac{1}{\sqrt{\kappa + W_n - n\pi/\gamma}} \right] - \gamma K \qquad (3.20)$$

where it can be shown that $K = K_1 = K_2$.

The immediate, and reassuring, conclusion is that the solutions obtained by the three different splits are indeed unique in spite of the apparent differences in the representation. On the other hand, the fact that only a single equation involving all of the unknown constants is obtained is not an encouraging result. Attempts to find additional equations involving the unknown constants $D_n^-(\lambda_j)$ have failed. In fact, any other choice of a suitable divisor function has also led to Eq. (3.20). It should be emphasized that any of the representations for $C_n^+(\lambda)$ and $D_n^-(\lambda)$ given above satisfy the differential equation and the boundary conditions.

It should be pointed out that Eqs. (3.16c&d) reduce to the correct expressions for $C_n^+(\lambda)$ and $D_n^-(\lambda)$ in the limiting case of no-sweep (i.e., $\gamma = 0$). This can be shown, most easily, by an application of the L'Hospital's rule to these equations when $\gamma \rightarrow 0$. Upon applying the limiting process it becomes obvious that nontrivial solutions can only be obtained for $n = 0$. The final results are given by

$$C_0^+(\lambda) = - \frac{b_0}{(2\pi)^{1/2} \sqrt{\kappa + W_0} \sqrt{\lambda + W_0} (\lambda + \kappa)} , \qquad (3.21a)$$

$$D_0^-(\lambda) = \frac{b_0}{(2\pi)^{1/2} (\lambda + \kappa)} \left[1 - i \frac{\sqrt{\lambda - W_0}}{\sqrt{\kappa + W_0}} \right] \qquad (3.21b)$$

in agreement with previous investigators (see, for example, Adamczyk (1974)).

49

In the general case of nonzero sweep, it appears that the complications introduced by the swept leading edge (i.e., the exponential behavior of the functions in Eq. (3.15a)) in conjunction with the finite span effects (i.e., the three-dimensional character of the flow near the two corners $\varsigma = 0$ and $\varsigma = 1$) cannot be overcome by the usual means. It is believed that a quantitatively accurate knowledge of the behavior of the flow near the two corners should provide some guidance in the determination of the unknown constants $D_n^-(\lambda_j)$. Such knowledge may be obtained by solving the problem of a gust interacting with a semi-infinite span geometry. In order to isolate the effects of the corner in such a geometry, the leading edge must be highly swept so as to cut-off the noise field due to the main part of the span. Then, the only contribution to the noise field would come from the corner. If the gust interaction problem for the corner can be analyzed, the results could, conceivably, provide useful estimates for the magnitude of the unknown constants arising in the vane problem in the high sweep limit.

In the light of the difficulties involved in obtaining an explicit exact solution for Eq. (3.10), an approximate solution to that equation is developed instead. The details of the derivation of the approximate solution are contained in the next section.

3.2 Derivation of the Approximate Solution

In order to obtain a useful expression for $h_m(\xi,y,\varsigma)$, an additional approximation is introduced here. From the discussion of the previous section it is clear that the presence of functions with exponential behavior at infinity cause difficulties in the application of the Wiener-Hopf technique. Recall that the entire function $E_{m,n}(\lambda)$ in Eq. (3.10) decays algebraically in the upper half-plane, but grows exponentially in the lower half-plane. Moreover, recall also that the functions $C_{m,n}^+(\lambda)$ and $D_{m,n}^-(\lambda)$ were shown to behave essentially in the same manner, i.e., the former decaying algebraically in the upper half-

plane while the latter growing exponentially (at the same rate as $E_{m,n}(\lambda)$) in the lower half-plane. Now, if both $C^+_{m,n}(\lambda)$ and $D^-_{m,n}(\lambda)$ were to contain the entire function $E_{m,n}(\lambda)$ as a factor, one could substantially simplify the mathematical problem by factoring the common dependence on $E_{m,n}(\lambda)$ out of Eq. (3.10) altogether. The great simplification resulting from this factorization is that the reduced equation, then, would only contain functions with algebraic behavior at infinity in both half-planes thus, making it amenable to the arguments of Liouville's theorem. In view of this tremendous gain in simplicity, it is, therefore, assumed that, as an approximation, both $C^+_{m,n}(\lambda)$ and $D^-_{m,n}(\lambda)$ contain $E_{m,n}(\lambda)$ as a factor.

Before proceeding with the derivation of the approximate solution, the physical implications of this mathematical approximation are briefly discussed. The approximation that $C^+_{m,n}(\lambda)$ and $D^-_{m,n}(\lambda)$ both contain $E_{m,n}(\lambda)$, is equivalent to the following two approximations in the behavior of $h_m(\xi,0,\zeta)$ and $\partial h_m(\xi,0,\zeta)/\partial y$ near the leading edge. The first approximation is to assume that the spanwise variations of the edge conditions are the same as that of the gust, i.e., $e^{i\gamma\kappa\zeta}\cos m\pi\zeta$. The second one involves neglecting the "boundary layer" behavior of $\mu(\zeta)$ near the two corners $\zeta = 0$ and $\zeta = 1$ and assuming that $\mu = 1/2$ everywhere along the span. In other words, one requires:

$$h_m(\lambda,0,\zeta) \propto \xi^{1/2}\, e^{i\gamma\kappa\zeta} \cos m\pi\zeta \quad \text{as} \quad \xi \to 0^+ \tag{3.22a}$$

and

$$\frac{\partial}{\partial y} h_m(\lambda,0,\zeta) \propto \xi^{-1/2}\, e^{i\gamma\kappa\zeta} \cos m\pi\zeta \quad \text{as} \quad \xi \to 0^- . \tag{3.22b}$$

As before (see Eqs. (3.13)), taking the Fourier transform and applying the orthogonality condition (3.7c), one finds

$$C_{m,n}^+(\lambda) \propto \lambda^{-3/2} E_{m,n}(\lambda), \qquad D_{m,n}^-(\lambda) \propto \lambda^{-1/2} E_{m,n}(\lambda), \qquad (3.23)$$

Now, returning to the derivation of the approximate solution, the change of variables is introduced:

$$C_{m,n}^+(\lambda) = \tilde{C}_{m,n}^+(\lambda) E_{m,n}(\lambda), \qquad D_{m,n}^-(\lambda) = \tilde{D}_{m,n}^+(\lambda) E_{m,n}(\lambda). \qquad (3.24)$$

Note that $\tilde{C}_{m,n}^+(\lambda)$ and $\tilde{D}_{m,n}^-(\lambda)$ are algebraic in their respective half-planes. In terms of the new functions, Eq. (3.10) takes the form:

$$- \sqrt{1-\gamma^2} \sqrt{\lambda + W_n} \; \tilde{C}_{m,n}^+(\lambda) = \frac{\tilde{D}_{m,n}^-(\lambda)}{\sqrt{\lambda - W_n}} - \frac{\epsilon_{m,n} b_m}{(2\pi)^{1/2}} \frac{1}{\sqrt{\lambda - W_n}(\lambda + \kappa)}. \qquad (3.25)$$

The term on the left hand side is analytic and algebraic in the upper half-plane while the first term on the right hand side is analytic and algebraic in the lower half-plane. The last term is mixed and algebraic and must be split additively. The split can be performed by subtracting the pole at $\lambda = -\kappa$ to obtain

$$\frac{1}{\sqrt{\lambda - W_n}(\lambda + \kappa)} = \left[\frac{i}{\sqrt{\kappa + W_n}(\lambda + \kappa)} \right]^+ + \left[\frac{1}{\sqrt{\lambda - W_n}(\lambda + \kappa)} - \frac{i}{\sqrt{\kappa + W_n}(\lambda + \kappa)} \right]^-.$$

$$(3.26)$$

Upon implementing the split in Eq. (3.25) and rearranging the resulting equation, one obtains

$$-\sqrt{1 - \gamma^2} \sqrt{\lambda + W_n} \; \tilde{C}^+_{m,n}(\lambda) + \left[\frac{i}{\sqrt{\kappa + W_n} \; (\lambda + \kappa)} \right]^+$$

$$= \frac{\tilde{D}^-_{m,n}(\lambda)}{\sqrt{\lambda - W_n}} - \left[\frac{1}{\sqrt{\lambda - W_n} \; (\lambda + \kappa)} - \frac{i}{\sqrt{\kappa + W_n} \; (\lambda + \kappa)} \right]^- . \tag{3.27}$$

Now, since both sides of Eq. (3.27) decay algebraically at infinity, by Liouville's theorem the entire function $J(\lambda)$ is identically zero. Thus,

$$\tilde{C}^+_{m,n}(\lambda) = \frac{i \, \epsilon_{m,n} \, b_m}{(2\pi)^{1/2} \sqrt{1 - \gamma^2} \; \sqrt{\kappa + W_n} \; \sqrt{\lambda + W_n} \; (\lambda + \kappa)} , \tag{3.28a}$$

$$\tilde{D}^-_{m,n}(\lambda) = \frac{\epsilon_{m,n} \, b_m}{(2\pi)^{1/2} \; (\lambda + \kappa)} \left[1 - i \, \frac{\sqrt{\lambda - W_n}}{\sqrt{\kappa + W_n}} \right] . \tag{3.28b}$$

Eq. (3.28a) describes the approximate value of the coefficient in the eigenfunction expansion (i.e., Eq. (3.8a)) of $H_m(\lambda, y, \zeta)$. It is interesting to note that the above expression can be obtained from Eqs. (3.16c&d) by choosing $D^-_{\bar{n}}(\lambda_j) = 0$ for all j's except 0 and 2n, and letting

$$D^-_{\bar{n}}(\lambda_0) = -(2\pi)^{-3/2} \, n^{-1} \, \epsilon_n \, b_0, \qquad D^-_{\bar{n}}(\lambda_{2n}) = (2\pi)^{-3/2} \, n^{-1} \, \epsilon_n \, b_0 . \tag{3.29}$$

The solution for $h_m(\xi, y, \zeta)$ is obtained by applying an inverse Fourier transform to $H_m(\lambda, y, \zeta)$;

$$h_m(\xi, y, \zeta) = (2\pi)^{-1/2} \int_{-\infty}^{+\infty} H_m(\lambda, y, \zeta) \, e^{-i\lambda\xi} \, d\lambda \ . \tag{3.30}$$

The solution for $h_m(\xi, y, \zeta)$ consist of an infinite number of modes. For all modes n of $h_m(\xi, y, \zeta)$, the integrand in Eq. (3.30) contains branch points at $\lambda = \pm W_n$ representing acoustic waves. For each mode $n = m$, the integrand also contains a pole at $\lambda = -\kappa$. This pole corresponds to local hydrodynamic motion near the airfoil (i.e., no pressure fluctuations are associated with it). It is interesting to note that for zero sweep (i.e., $\gamma = 0$) $C^+_{m,n}(\lambda) \equiv 0$ for $n \neq m$. In this case the mode $n = m$ is the only acoustic mode generated in response to the oncoming gust mode m. The introduction of sweep produces cross mode transfer, i.e., the oncoming gust mode m produces acoustic motion in all mode orders. Using contour integration method, it can be shown that this solution satisfies the governing differential equation and the boundary conditions.

The quantity of most practical significance, for the purposes of this study, is the noise radiated to the farfield. Far away from the airfoil, the solution is expressed most simply in terms of the cylindrical polar coordinates corresponding to the orthogonal coordinate system (x', y, z). Thus, reverting back to (x', y, z) coordinates in Eq. (3.30) and then rewriting it in (r, θ, z) coordinate system, one finds the following expression

$$h_m(\xi, y, \zeta) = (2\pi)^{-1/2} \, \text{sgn}(\sin\theta) \sum_{n=0}^{+\infty} \left[\int_{-\infty}^{+\infty} C^+_{m,n}(\lambda) \, e^{irP(\lambda)} \, d\lambda \right] \cos n\pi z \tag{3.31a}$$

where

$$P(\lambda) = \sqrt{1 - \gamma^2} \left[-\lambda\cos\theta + i\sqrt{\lambda^2 - W_n^2} \, |\sin\theta| \right] , \tag{3.31b}$$

$$x' = r \cos\theta, \quad y = r \sin\theta, \quad z = z, \quad 0 \le r < \infty, \quad 0 \le \theta \le 2\pi \ . \tag{3.31c}$$

54

Note that for a given value of frequency and Mach number only a finite number of modes represent propagating acoustic waves. Modes for which W_n (defined by Eq. (3.8c)) is imaginary are cut-off and do not radiate energy to the farfield.

The asymptotic behavior of the modified acoustic velocity potential for large r can be evaluated by applying the method of steepest descent (Olver (1974)) to Eq. (3.31a). The saddle point of the phase $P(\lambda)$ in that equation is located at $\lambda = -W_n \cos\theta$. Deforming the integration path to pass through the saddle point as shown in Fig. (3.4) and utilizing the standard steepest descent approximations, one finds

$$h_m(r,\theta,z) = \frac{\gamma e^{i\pi/4} b_m}{(1-\gamma^2)^{3/4}} \frac{1}{\sqrt{\pi r}} \left[\sum_{n=0}^{n'} g_{m,n}(r,\theta) \cos n\pi z \right] \cos \frac{\theta}{2} , \qquad (3.32a)$$

$$g_{m,n}(r,\theta) = \epsilon_{m,n} \frac{e^{i\sqrt{1-\gamma^2} \, W_n \, r}}{\sqrt{\kappa + W_n}}$$

$$\times \left\{ \frac{f_1(\theta) \, f_2(\theta) + f_3(\theta) \, f_4(\theta)}{2 \, f_1(\theta) \, f_2(\theta) \, f_3(\theta) \, f_4(\theta)} \right\} [(-1)^{(m+n)} \, e^{if_n(\theta)} - 1] \qquad (3.32b)$$

where

$$f_n(\theta) = \gamma(\kappa - W_n \cos\theta) , \qquad (3.32c)$$

$$f_1(\theta) = f_n(\theta) + (m + n)\pi, \qquad f_3(\theta) = f_n(\theta) + (m - n)\pi ,$$

$$\qquad (3.32d)$$

$$f_2(\theta) = f_n(\theta) - (m + n)\pi, \qquad f_4(\theta) = f_n(\theta) - (m - n)\pi$$

where the index n', in Eq. (3.32a), is the largest value of n for which W_n is real.
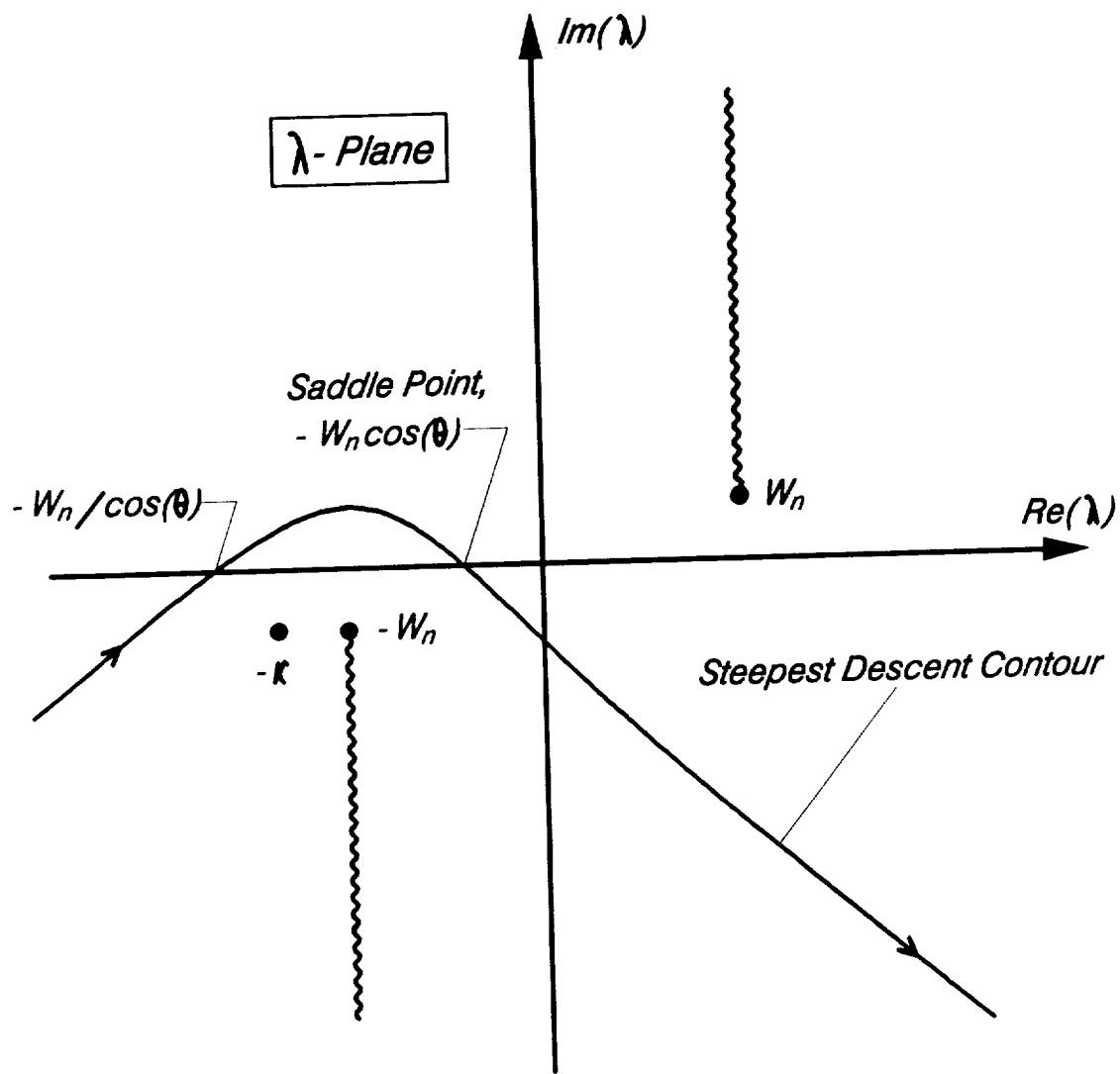
Fig. 3.4 Steepest descent path in the complex λ-plane.

56

The general features of the farfield noise radiation are easily deduced from Eqs. (3.32). For the unswept case, the farfield acoustic pressure falls as $r^{-1/2}$ and has a directivity pattern of $\cos\theta/2$. Thus, the functions $g_{m,n}(r,\theta)$ represent the modifications due to sweep. For a fixed upwash spatial mode number m, the following is observed. The effects of sweep are quite substantial when the product $\gamma\kappa$, and hence $f_n(\theta)$, is large. The major influence comes from the two factors which are enclosed by the curly and square brackets in Eq. (3.32b), respectively. The part inside the square bracket has a magnitude which oscillates between zero and two as the farfield observation angle θ is varied. This produces a modulation of the basic $\cos\theta/2$ directivity pattern. The modulation becomes more rapid as $\gamma\kappa$ increases. For fixed $\gamma\kappa$, the modulation is strongest for the low order acoustic modes (i.e., small n) since, W_n decreases with mode order. The factor enclosed by the curly bracket also modifies the directivity pattern, but at low Mach numbers the effect is fairly small since, $W_n < \kappa M_\infty$. This part primarily controls the modal amplitudes producing substantial reductions when $\gamma\kappa$ is large. For the limiting case of zero sweep angle ($\gamma = 0$),

$$g_{m,m}(r,\theta) = \frac{ib_m e^{iW_m r}}{\sqrt{\kappa + W_m}\,(\kappa - W_m \cos\theta)} \qquad \text{for} \quad n = m , \qquad (3.33a)$$

$$g_{m,n}(r,\theta) \equiv 0 \qquad \text{for} \quad n \neq m \qquad (3.33b)$$

in agreement with previous investigators (see, for example, Adamczyk (1974)).

Eqs. (3.32) express the farfield representation of the modified acoustic velocity potential h_m due to a single spatial mode m of the jth temporal harmonic of the gust upwash. Recall that the acoustic velocity potential $\phi_{j,m}$ is related to h_m through

Eq. (2.23). Thus, the total acoustic farfield generated by the jth harmonic component of the upwash can be written as

$$\phi_j(r,\theta,z,t) = \sum_{m=0}^{+\infty} h_m(r,\theta,z) \, e^{-ikx\left[(M_\infty^2 r \cos\theta)/\beta_\infty + U_\infty t\right] + 2\pi i j s \tan\psi} . \qquad (3.34)$$

So far, only the qualitative features of the farfield noise have been discussed. Using Eqs. (3.32) and (3.34), quantitative results can be obtained by calculating the time-averaged acoustic power radiated to the farfield. This quantity is computed by integrating the flux of the time-averaged farfield acoustic intensity over a suitable control volume enclosing the airfoil. In the language of the divergence theorem

$$P = \int_0^{2\pi} \int_0^1 < \vec{I} > \cdot \vec{n} \; dz \; d\theta \qquad (3.35a)$$

where P denotes acoustic power, $< \vec{I} >$ the time averaged acoustic intensity vector, and $\vec{n}$ the unit normal to the surface of the control volume. The expression for the acoustic intensity, appropriate to a moving medium, is given by (Goldstein (1976))

$$\vec{I} \equiv \left(\frac{p'}{\rho_0} + \vec{u} \cdot \vec{U}_\infty \right) \left(\rho_0 \vec{u} + \rho' \vec{U}_\infty \right) . \qquad (3.35b)$$

For convenience the control volume chosen is a circular cylinder in the Prandtl-Glauert coordinates (x',y,z) whose generators are parallel to the leading edge of the airfoil and whose axis is aligned with the leading edge itself. The upper and lower surfaces of the control volume are the upper and lower channel walls, respectively. Using these formulae, numerical values for total acoustic power, P, and the modal acoustic power, P_n can be calculated. These results are presented in the next section.

3.3 Single Vane Results and Discussion

In this section, the single finite span swept airfoil model is utilized to predict the influence of sweep on noise levels generated by gust-airfoil interaction as a function of airfoil sweep. These single airfoil results help us identify the important trends and parameters that represent the influence of sweep on noise generation. First, calculations for the simplest case of a single (spatial) mode convected gust interacting with an isolated airfoil are presented. Then, results from a parametric study of noise generated by the interaction of a rotor viscous wake with a single vane are presented.

3.3.1 Single Mode Results

In order to understand the features of the single mode solution, it is useful to note that each gust mode can be represented as the sum of two oblique plane wave gusts with gust angles Λ and $-\Lambda$, respectively. Here, Λ is the angle of the convected gust wavenumber vector relative to the streamwise direction (i.e., the x-axis). This plane wave representation allows a comparison between the finite span solution and the corresponding case for an infinite span airfoil. The infinite span solution is derived in Appendix C.

As was mentioned in the introduction, for an infinite span airfoil interacting with an oblique convected plane wave gust, there is a critical airfoil sweep angle α_{cr} beyond which no noise generation occurs. This critical sweep angle depends on the gust angle Λ and on the mean flow Mach number M_{∞}. The critical sweep angle (derived in Appendix C) for an infinite span airfoil is given by

$$\alpha_{cr} = \tan^{-1}\left[-\tan\Lambda + M_{\infty}\sqrt{1 + \tan^2\Lambda}\right], \qquad \tan\Lambda = m\pi/k_x \ . \tag{3.36}$$

59

The sweep angles required for cut-off are plotted as a function of Mach number in Fig. (3.5). The cases $\Lambda = 0, \pm 10$, and ± 20 degrees are presented. Clearly positive Λ increases the gust obliqueness as seen by the airfoil leading edge, and hence α_{cr} decreases. Conversely, negative Λ reduces the gust obliqueness, and hence α_{cr} increases. For $M_\infty = 0.4$ and sweep angles greater than $\alpha_{cr} = 21.8$ degrees, no noise will be generated by plane wave convected gusts with zero or negative Λ.

In connection with the above discussion, recall that the cut-off phenomenon can also be explained in terms of the gust spanwise trace velocity relative to the oncoming mean flow. If for a given set of parameters (i.e., Mach number, sweep angle, and gust angle) this trace velocity is subsonic the noise field will be cut-off. In terms of the relevant parameters, the gust spanwise relative trace Mach number is given by (see Appendix C for details)

$$M_{tr} = \frac{M_\infty \cos\alpha}{\sin(\alpha + \Lambda)} . \tag{3.37}$$

A graphical representation of Eq. (3.37) for $M_\infty = 0.4$ is shown in Fig. (3.6). Again, the cases corresponding to $\Lambda = 0, \pm 10$, and ± 20 degrees are presented. In this diagram, the line $M_{tr} = 1$ is the dividing boundary between the noise generation and cut-off, and hence it is the locus of the critical sweep angles as the gust angle is varied. Again, note that positive Λ decreases α_{cr} and negative Λ increases α_{cr} in agreement with the above results. In subsequent sections, Figs. (3.5) and (3.6) will often be referenced in interpreting the results from the parametric study. The discussion of finite span solution is now resumed.

3.3.1.1 Results for m = 0. This case corresponds to a plane wave gust whose wavenumber vector is parallel to the streamwise direction, since for $m = 0$, $\Lambda = 0$ (see Eq. (3.36)). The numerical results for this case are presented for the total acoustic power,

60
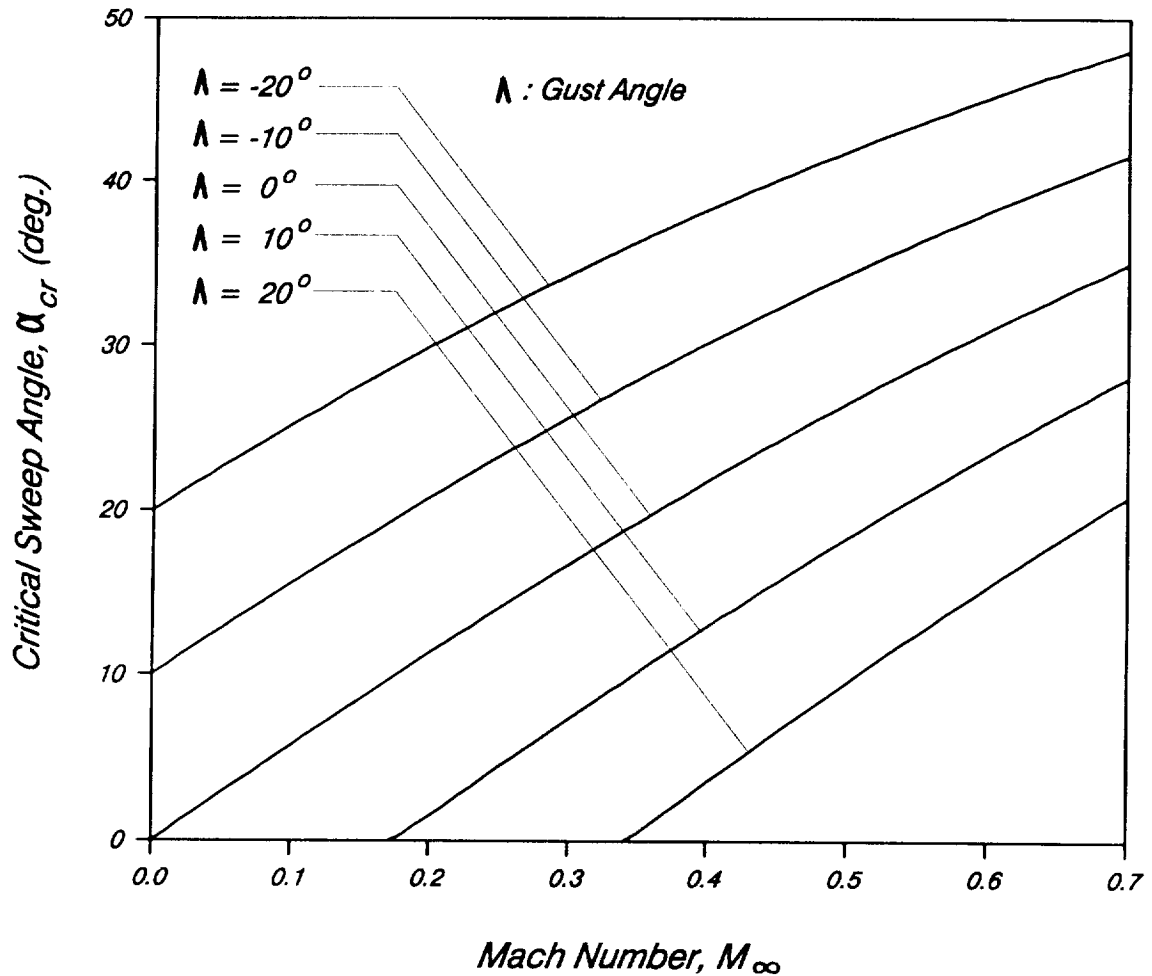
Fig. 3.5   Critical sweep angles for an infinite span airfoil interacting with an oblique
convected gust (Λ is the convected gust angle).

61

Gust Relative Trace Mach Number, M_{tr}

3.0

2.6

2.2

1.8

1.4

1.0

0.6

0.2

$\Lambda = -20^{0}$

$\Lambda = -10^{0}$

$\Lambda = 0^{0}$

$\Lambda = 10^{0}$

$\Lambda = 20^{0}$

Λ : Gust Angle

Cut-off Noise Field for $M_{tr} < 1$

0   10   20   30   40   50
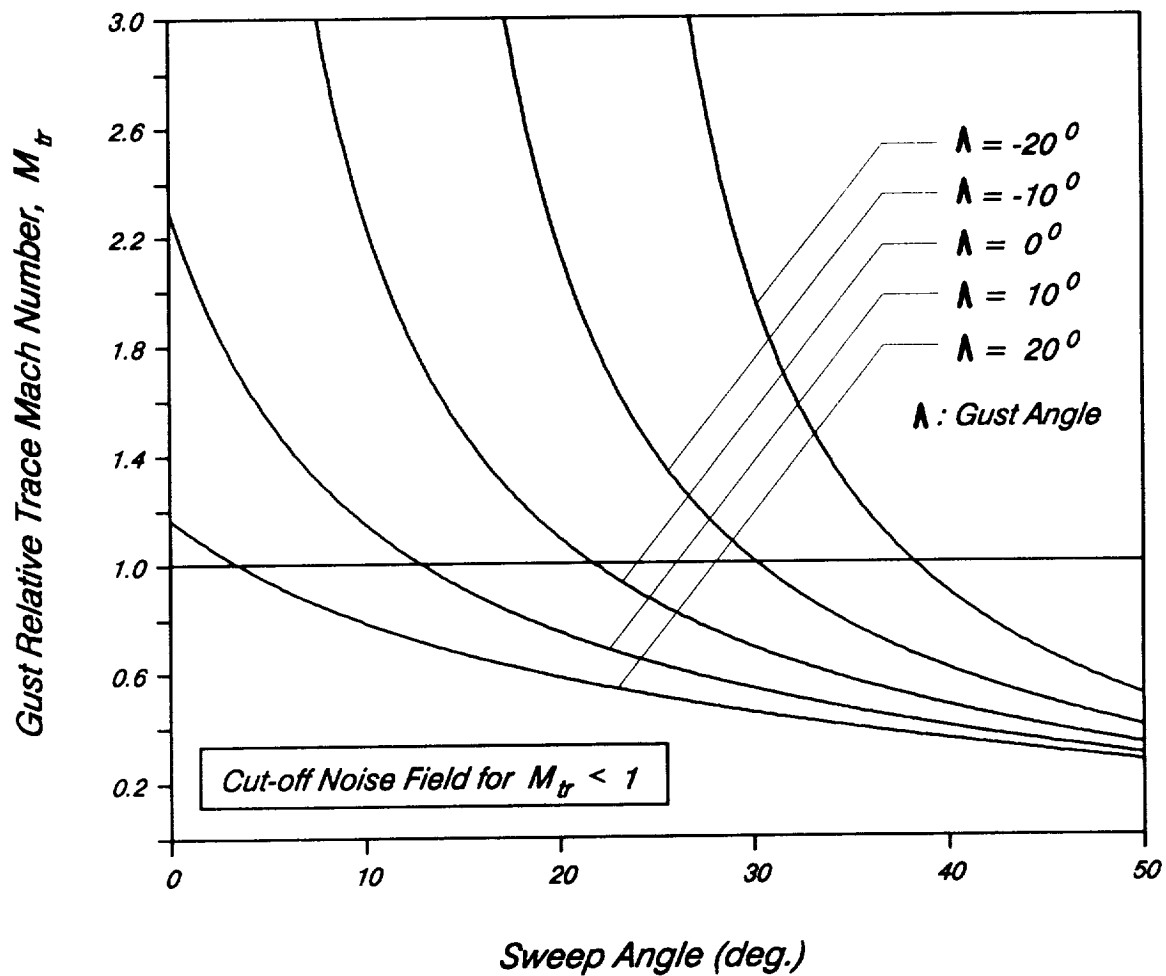
Sweep Angle (deg.)

Fig. 3.6   Variations of gust spanwise relative trace Mach number as a functions of sweep angle. Streamwise stator row Mach number is $M_{\infty} = 0.4$.

62

the modal acoustic power, and the angular distribution of modal acoustic power. The mean flow Mach number is set to $M_\infty = 0.4$ in all cases.

Fig. (3.7) displays the dependence of total acoustic power on airfoil sweep angle for a number of gust wavelengths. In each case, the power is normalized by its value at $\alpha = 0$ degrees. The infinite span result, which is independent of k_x, is also plotted for comparison. For gust angle $\Lambda = 0$ degrees, the critical sweep angle for the infinite span case is $\alpha_{cr} = 21.8$ degrees (see Fig. (3.5) or (3.6)). The infinite span airfoil generates no acoustic power for sweep angles greater than α_{cr}. The finite span acoustic power is shown for three frequencies corresponding to $k_x = 17.5$, 35, and 70. In a modern aircraft engine $k_x = 35$ corresponds to a typical blade-passing frequency (BPF) and $k_x = 70$ to its first higher harmonic. The finite span results display some reduction in the power level for sweep angles less than 20 degrees and a significant drop in the noise levels beyond α_{cr}. The decrease with sweep angles is most rapid for higher values of k_x. The finite span results, however, are consistently higher than the infinite span results. The reason for this behavior will be discussed later.

The finite span acoustic power decibel (i.e., $10 \log(P(\alpha)/P(0))$) reductions, for sweep angles in the neighborhood of α_{cr}, are plotted in Fig. (3.8). Five values of k_x ranging from 15 to 75 are displayed. For comparison, the values of k_x which correspond to the cut-on frequencies of the acoustic duct modes, n, are shown in Table 3.1. For $k_x = 15$, the second higher mode has just cut-on. Even for this relatively low frequency, a noise reduction of 7 dB occurs at $\alpha = 30$ degrees. The noise reductions are larger at higher frequencies. For $k_x = 75$, a 12 dB reduction occurs at $\alpha = 25$ degrees. Eleven radial modes are propagating in this case. At higher frequencies, the noise level initially
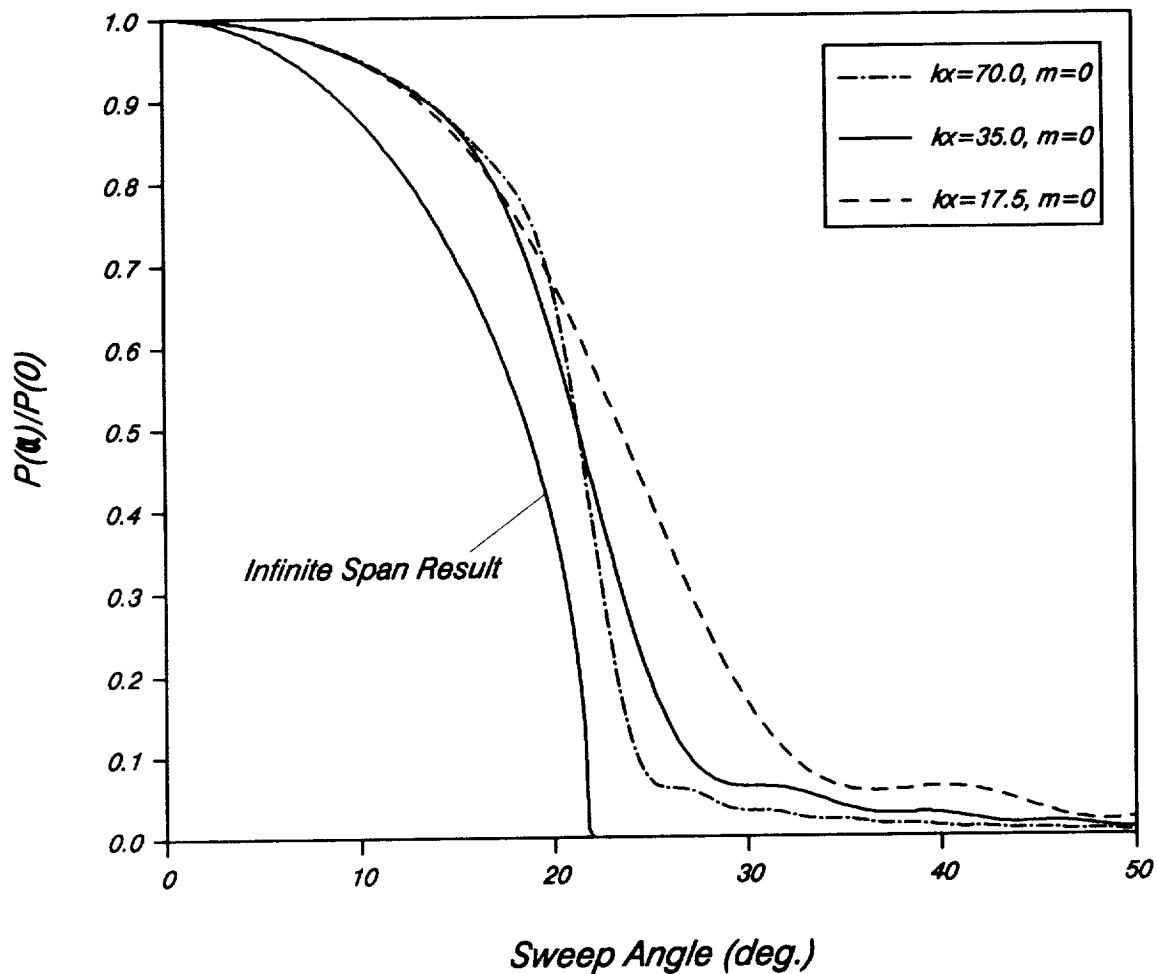
Fig. 3.7 Ratio of total acoustic power to its value at α = 0 degrees for convected gust mode m = 0. (Convected gust angle Λ = 0 degrees).

64
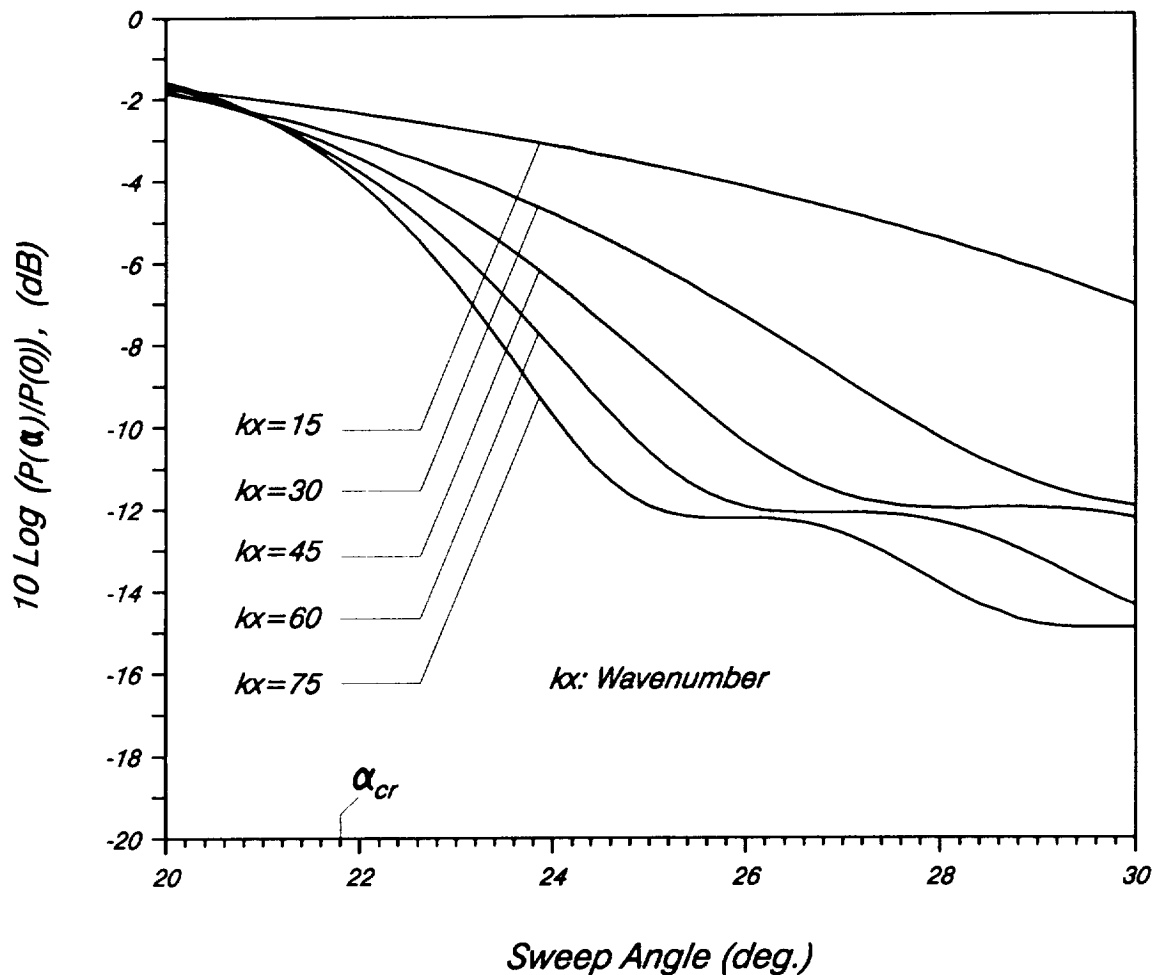
Fig. 3.8   Finite span total acoustic power ratio plotted in decibels (dB) for sweep angles greater then α_{cr}.

Table 3.1 Modal cut-on frequencies ($\omega = k_x U_\infty$) for $M_\infty = 0.4$.

$$M_\infty = 0.4$$

Mode Number	k_x
0	- -
1	7.2
2	14.4
3	21.6
4	28.8
5	36.0
6	43.2
7	50.4
8	57.6
9	64.8
10	72.0
11	79.2

falls off more rapidly with sweep angle. The noise level then reaches a short plateau before dropping further. The scale of this pattern is inversely proportional to k_x.

The approach of the finite span acoustic power to the infinite span results, as k_x increases, is illustrated in Fig. (3.9). Here, the ratio of the finite span acoustic power to the infinite span value, for sweep angles of 10, 15 , and 20 degrees is plotted. At $\alpha = 15$ degrees, for all wavenumbers above $k_x = 10$, the finite span result lies within 80% of the infinite span value. The agreement is surprising, since at this frequency only four modes are propagating. At $\alpha = 10$ degrees, the deviation from the infinite span results are even smaller. For $\alpha = 20$ degrees, the finite span power oscillates more strongly with frequency and does not appear to be approaching the infinite span results. This is not surprising, since finite span effects become more important as the critical sweep angle is approached.

The dependence on sweep angle of the acoustic power modal distribution is presented in Fig. (3.10). The case $k_x = 50$, for which seven modes are propagating, is considered. The ordinate gives the fraction of total acoustic power propagating in each mode. At $\alpha = 0$ degrees (i.e., the unswept case), all of the acoustic power is concentrated in the mode $n = 0$ which is the only propagating mode. For nonzero sweep angles the acoustic power is distributed within all of the propagating acoustic modes (in this case seven). As α is increased, the concentration of acoustic power shifts to higher order modes. The $n = 3$ mode makes the largest contribution to the acoustic power radiation for $\alpha = 15$ degrees while the largest contribution at $\alpha = 25$ degrees comes from the highest propagating mode $n = 6$. Thus, as well as decreasing the total power generation, sweep tends to concentrate the acoustic energy in higher order modes. Since higher order modes are generally absorbed more effectively by acoustic liners, this effect should be very beneficial in practical applications.
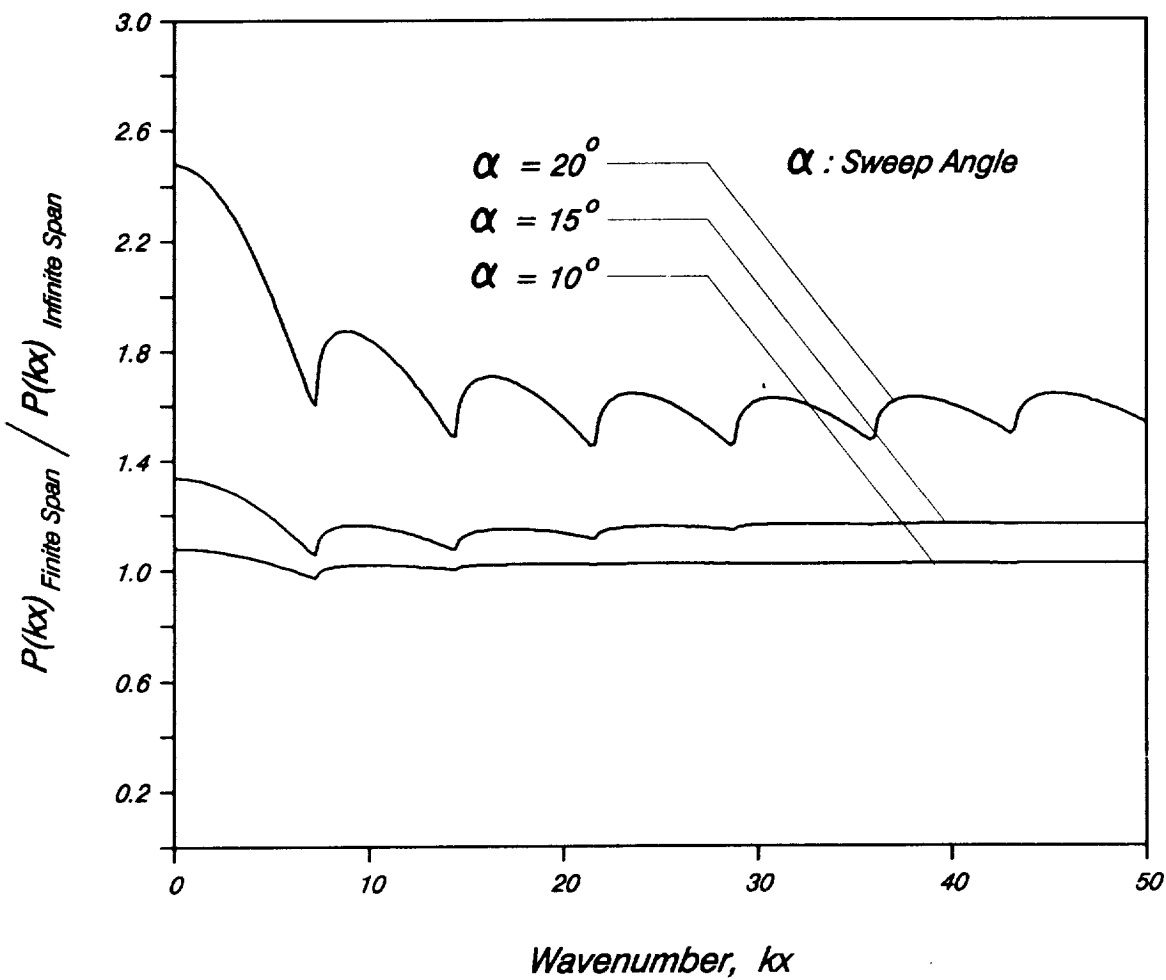
Fig. 3.9   Approach of the finite span total acoustic power to the infinite span value as a function of frequency.
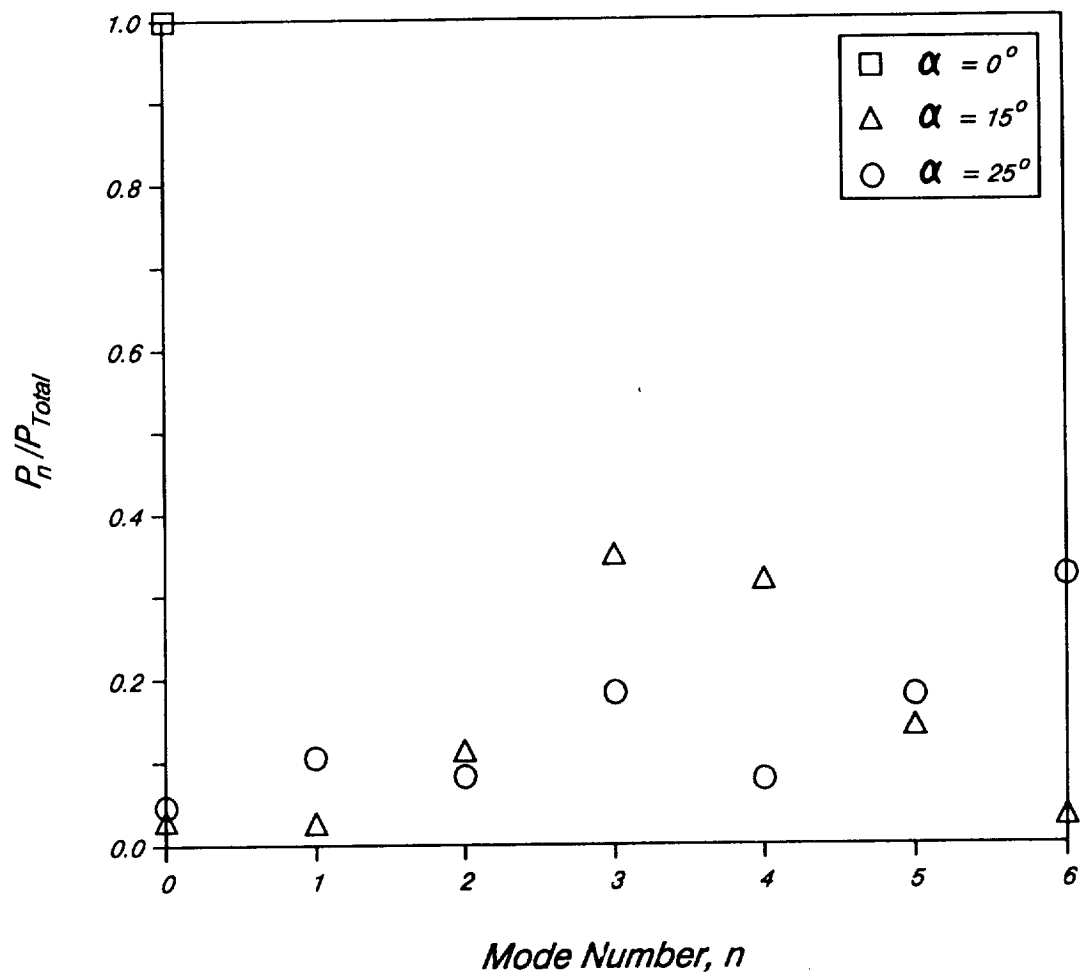
Fig. 3.10 Modal distribution of acoustic power as function of sweep angle for $k_x = 50$.

The effect of sweep on the farfield directivity patterns is quite dramatic. The case $\alpha = 15$ degrees and $k_x = 75$ is considered in Fig. (3.11). The magnitude of the modal acoustic pressure as a function of angle in the physical plane (as opposed to the Prandtl-Glauert plane), $\theta' = \tan^{-1}(y/x)$ is plotted. The directivity pattern for modes $n = 0$, $n = 5$, and $n = 10$ are illustrated. For the case considered, these correspond to the lowest, midrange, and highest order propagating modes, respectively. For comparison the directivity pattern for the unswept case is also plotted. The envelope for each of the three modes is very similar to the $\cos\theta'/2$ directivity pattern which occurs for the case of an unswept airfoil. However, the introduction of sweep has produced a modulation of the basic directivity pattern. This modulation is most rapid for the low order modes and relatively slow for the higher order modes near cut-off. The $n = 0$ and $n = 5$ patterns have seven lobes while the $n = 10$ pattern has three. Physically, the modulation occurs because the difference in acoustic path lengths, from two leading edge points to a farfield point, is dependent on the observation angle θ'. As this angle changes, the variation in the path length difference leads to alternating reinforcement and cancellation. The higher modes are oblique waves whose effective phase velocities are higher than those for the plane wave. Thus, a larger path length difference is required to produce reinforcement or cancellation and the modulation with change of observer angle is slower.

3.3.1.2 Results for m ≠ 0. Here, numerical results for the dependence of the total acoustic power on airfoil sweep for higher order gust (spatial) modes are presented. For $m \neq 0$, the gust wavenumber vector is no longer parallel to the streamwise direction (i.e., $\Lambda \neq 0$). For the sake of brevity, only results for the total acoustic power are presented here. As before, in each case the power is normalized by its value at zero sweep angle.
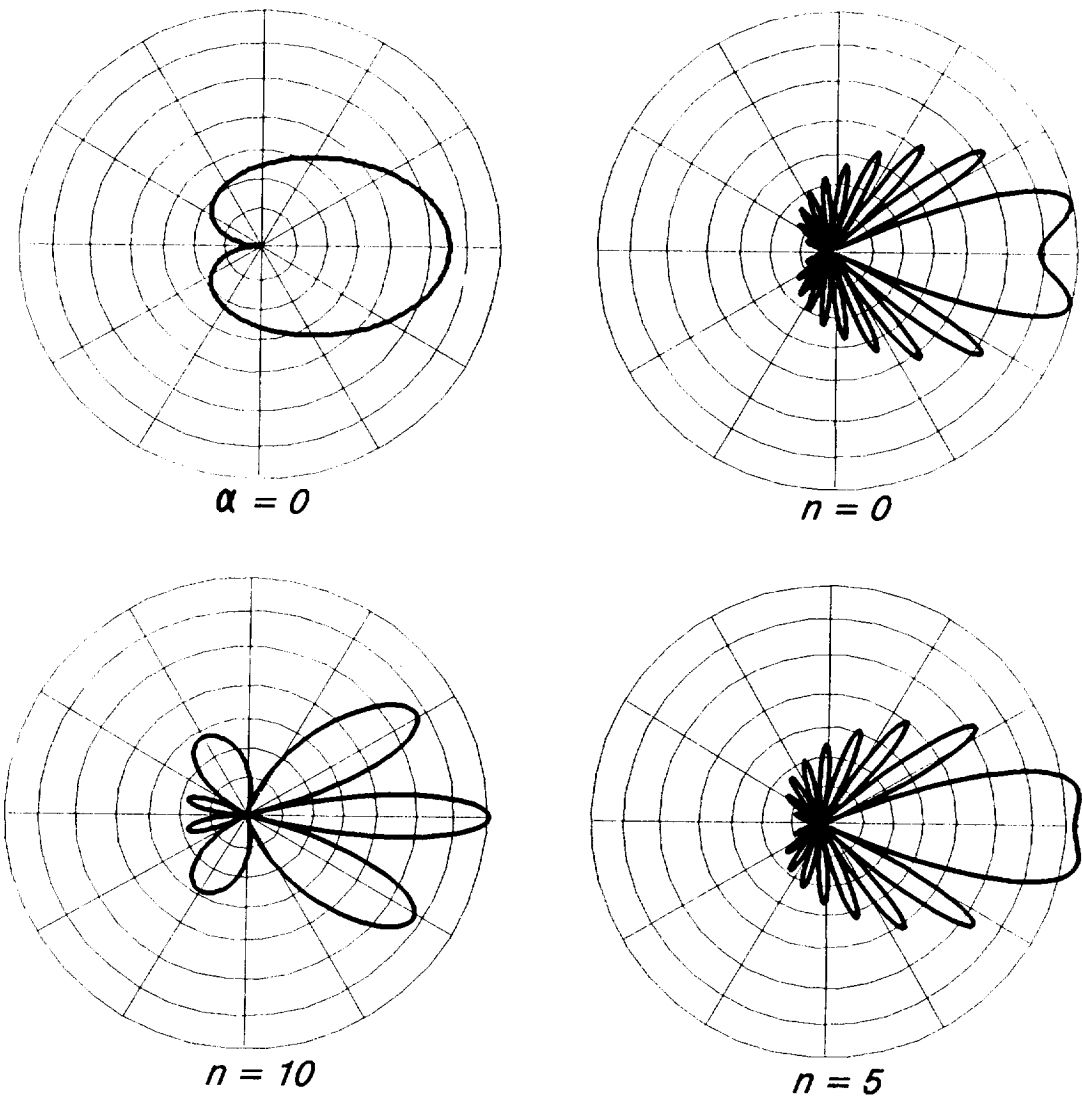
Fig. 3.11   Modal farfield pressure directivity patterns for the case $k_x = 75$ and $\alpha = 15$
degrees. Results for modes n = 0, n = 5, and n = 10 are plotted. The unswept
case (i.e., $\alpha = 0$ degrees) is also plotted for comparison.

71

Fig. (3.12) illustrates typical behavior for the case of higher mode convected gusts. Finite span results for three different modes and three different frequencies are shown. For each frequency, the convected gust mode index m falls near the middle of the range of propagating acoustic duct modes given in Table (3.1). The ratios m/k_x are identical in each case and thus, each convected gust mode can be represented as the sum of two oblique plane wave convected gusts with gust angles of $\Lambda = \pm 10$ degrees. The equivalent infinite span case is also shown for comparison. Referring to Fig. (3.5), it is seen that here the two critical sweep angles are approximately 13 and 30 degrees. The infinite span result in Fig. (3.12) shows that the noise reduction also occurs in two stages corresponding to the two critical sweep angles. The finite span results follow the same general trend with a moderate noise reduction for angles less than the smaller critical angle and a sizable reduction beyond the larger critical sweep angle. The reductions are more rapid for higher frequencies. The finite span results are again consistently above the infinite span case.

In order to examine noise generation by convected modes whose index m falls near the upper limit of the cut-on acoustic modes, three finite span cases with effective plane wave gust angles of $\Lambda = \pm 20$ degrees are presented in Fig. (3.13). Here the two critical sweep angles are approximately 4 and 38 degrees. The infinite span result again shows two distinct "humps" corresponding to the two critical sweep angles. Here, however, between 4 and 20 degrees, an increase in sweep angle actually increases the infinite span noise. The physical explanation is that, for zero airfoil sweep, gust modes with $\Lambda = \pm 20$ degrees are highly oblique to the leading edge. Increasing the airfoil sweep angle has actually made the $\Lambda = -20$ degrees gust less oblique to the leading edge, and hence raised the noise level. The finite span results again follow the general behavior of the infinite span case. At airfoil sweep angles around 30 degrees, a slight increase in noise level occurs. Beyond
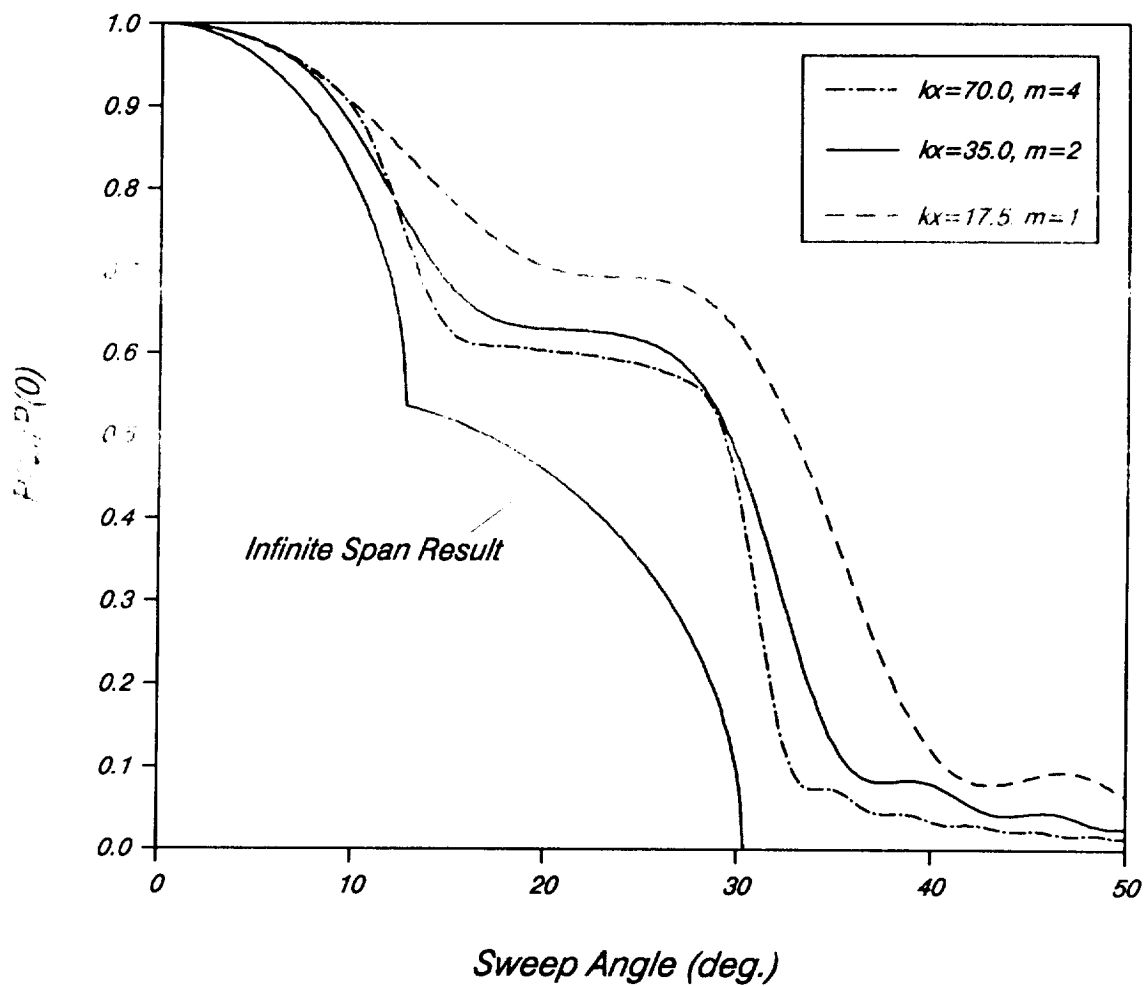
Fig. 3.12   Ratio of total acoustic power to its value at $\alpha = 0$ degrees for convected gust modes whose effective gust angles are $\Lambda = \pm10$ degrees.
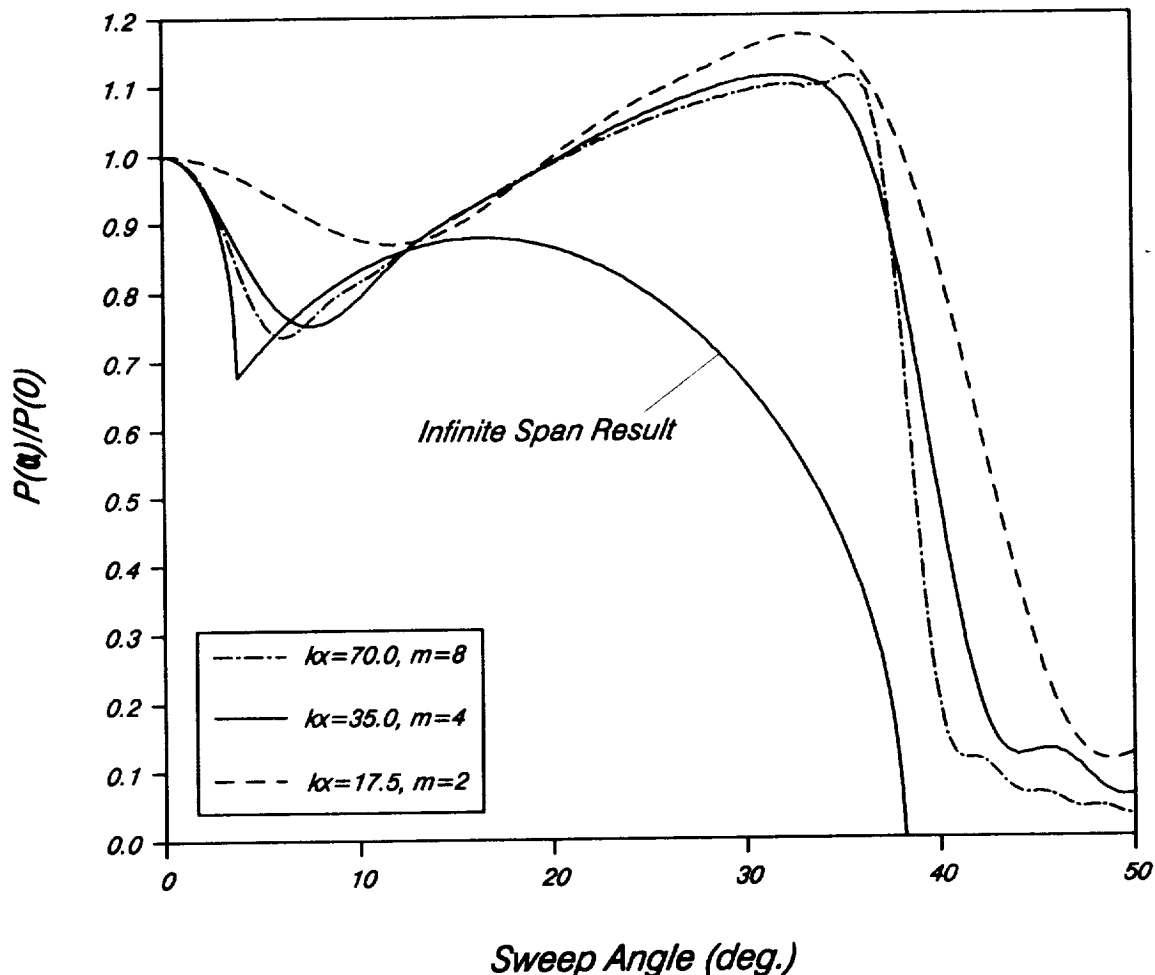
Fig. 3.13   Ratio of total acoustic power to its value at α = 0 degrees for convected gust modes whose effective gust angles are Λ = ±20 degrees.

α = 38 degrees a substantial decrease in noise level occurs with the decrease being more rapid for higher frequencies.

In Figs. (3.12) and (3.13) (as well as Fig. (3.7)), it is interesting to note that the two highest frequency finite span cases are always fairly close together, but that they show a noticeable deviation from the infinite span result. For high frequencies and sweep angles below the critical angle, one might have expected that the finite span solution would approach the infinite span result. However, the above results suggest that the high-frequency limit of the finite span solution is probably different from the infinite span case. The deviation might be explained in the following way. First, as an infinite span airfoil approaches the critical sweep angle, the effective acoustic wavelength in the plane perpendicular to the leading edge becomes large. In assessing the importance of adjacent walls, it is probably this effective wavelength which must be compared with the wall spacing. It also seems reasonable to assume that the importance of adjacent walls depends on the source directivity. A source whose acoustic power output is directed mainly at the wall will be influenced more significantly than one whose power is directed parallel to the wall. To test these ideas, the cases of swept vertical and horizontal dipole lines located between walls and with phases identical to those found for the swept airfoil were compared. The vertical dipole, whose power is mainly directed parallel to the wall, produced results that were closer to the infinite span predictions than our results shown in Figs. (3.7), (3.12), and (3.13). The horizontal dipole, whose power output is directed mainly in the y = 0 plane and perpendicular to the leading edge, produced larger deviations than those for our results. Since, in terms of power output directed towards the wall, the present noncompact airfoil source is intermediate between the vertical and horizontal dipoles, these results provide at least a partial confirmation that the above

reasoning is correct. It is also interesting to note that an airfoil compact source model would have produced predictions similar to the vertical dipole which are noticeably different from the present noncompact source results.

It is clear from the above results that the introduction of airfoil sweep produces substantial reductions in noise level in many situations. However, the magnitude of the noise reduction is strongly dependent on the details of the convected gust. Thus, in order to make realistic assessment of the effectiveness of sweep in reducing noise due to the interaction of a single stator vane with a rotor viscous wake, it is imperative to include the contributions from all gust spatial modes m. This is done in the next section.

3.3.2 Rotor Wake Results

In this section, calculations of noise generated by the interaction of rotor blade viscous wakes with a single finite span swept stator vane are presented. Since the noise reduction due to sweep is caused by destructive interference from acoustic sources on the same vane, useful information on the effectiveness of sweep can be obtained by examining the interaction of the rotor wake with a single stator vane. Since only a single vane is considered in this chapter, no information about the distribution of power within the circumferential modes is obtained. Such results, which are obtainable from a cascade model, are presented in the next chapter. The present model does provide information on the distribution of power within the radial modes. However, in the interest of brevity, here attention is focused, for the most part, on the influence of airfoil sweep on the total acoustic power.

The conditions chosen for study correspond roughly to approach operating conditions for two research fans commonly referred to as NASA ROTOR 55 and ROTOR 11. The fan diameters are both 0.5m, and their designs are typical of low-pressure ratio

76

and high-pressure ratio fans, respectively. Details of the fan characteristics can be found in Kantola and Warren (1978), and Shaw and Balombin (1981). In terms of the present study, the most important difference between the two fans is their rotor blade count, or equivalently their blade-passing frequency (BPF). ROTOR 55 has 15 blades and the operating point chosen for study corresponds to a BPF = 1700 Hz (k_x = 10.1, see Eq. (2.8b)). ROTOR 11 has 44 blades and the operating point chosen for study corresponds to a BPF = 6000 Hz (k_x = 35.4). From Table (3.1), it is seen that, at their respective blade-passing frequencies, ROTOR 55 has two propagating (radial) modes while ROTOR 11 has five propagating (radial) modes.

For the interaction of rotor viscous wakes with stator vanes, it is known that the generated noise level is strongly dependent on rotor-stator spacing and rotor-tip speed. These parameters primarily affect the magnitude and relative half-width of the gust upwash experienced by the stator vanes. Although these parameters are important in setting the absolute levels of the generated tones, parametric calculations have shown that the relative changes in levels produced by vane sweep are fairly insensitive to rotor speed and rotor wake half-width. Thus, here calculations for only one tip speed (for each fan) and rotor wake half-width are presented. For completeness, however, a few baseline results indicating the influence of wake half-width are also included.

In Fig. (3.14), the decibel variations of the total acoustic power at the BPF and its two higher harmonics as a function of rotor wake half-width, for an unswept vane, are presented. The wake half-width, δ, is normalized by $d_r \cos\psi$, where d_r is rotor blade spacing and ψ is the rotor blade stagger angle as defined in Chapter 2. The level of each harmonic is normalized by the BPF level at δ = 0.0. "Zero" wake half-width corresponds to an idealized case where the amplitudes of all of the gust harmonics are equal (see
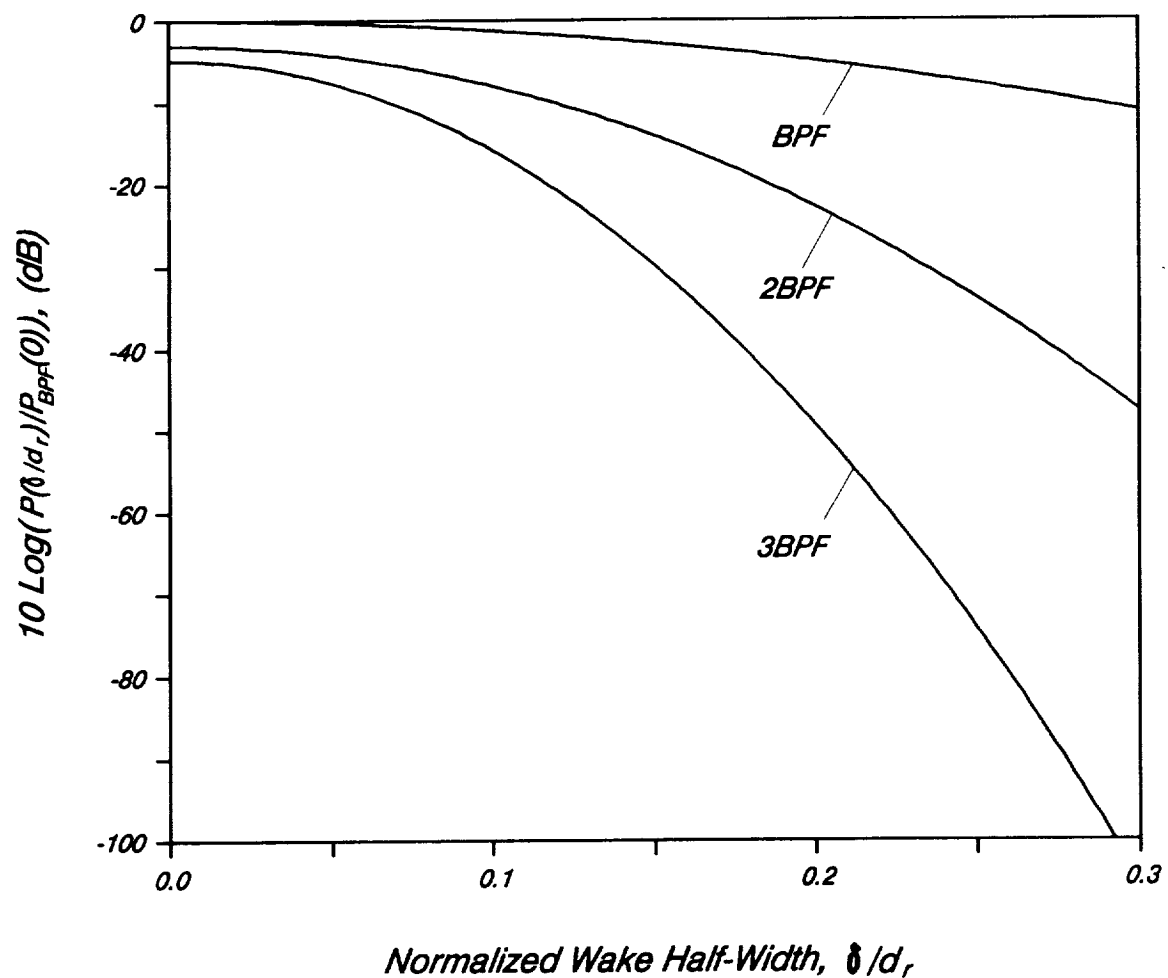
Fig. 3.14 Decibel variations of the acoustic power for the first three harmonics of BPF noise as a function of normalized wake half-width for an unswept airfoil.

Eq. (2.8b)). The noise level at the BPF and its harmonics decreases as the wake half-width is increased (say by increasing the rotor-stator spacing) with the reduction being most rapid for the higher harmonics. The reduction in the noise level is a consequence of the decreasing gust amplitudes with the widening wakes (see Eq. (2.8b)). A typical value for the normalized wake half-width, based on experimental evidence (see, for example, Shaw and Balombin (1981)), is 0.1. For this wake half-width, the BPF is separated by roughly 8 dB from its second harmonic and 16 dB from its third harmonic. In all the results presented in the remainder of this section, as well as the next chapter, the normalized wake half-width is assumed to be equal to 0.1.

Baseline results indicating the influence of the axial Mach number (at the stator row) on the generated noise levels are illustrated in Fig. (3.15). Again, decibel variations of the first three harmonics of the farfield acoustic power as a function of the Mach number, for an unswept vane, are plotted. Here, the general trends are quite similar for all three harmonics. The reduction in noise levels is a direct consequence of increasing reduced frequency (i.e., $k_x M_\infty/\beta_\infty^2$) with increasing axial Mach number. In the remainder of this work, it is assumed that $M_\infty = 0.4$, which is a typical value for approach operating conditions.

A parameter which the present study has shown to have a significant affect on the relative noise levels is the wake circumferential lean. As was mentioned in the beginning of Chapter 2, wake circumferential lean occurs because the tangential velocity between the rotor and stator generally deviates from a forced vortex design. Based on the data of Shaw and Balombin (1981) and other sources of available information, it appears that wake lean angles (Γ, defined in Chapter 2) of 20 degrees are typical. However, in view of the importance of the wake lean, results for wake circumferential lean angles of $\Gamma = 0$, 10, and
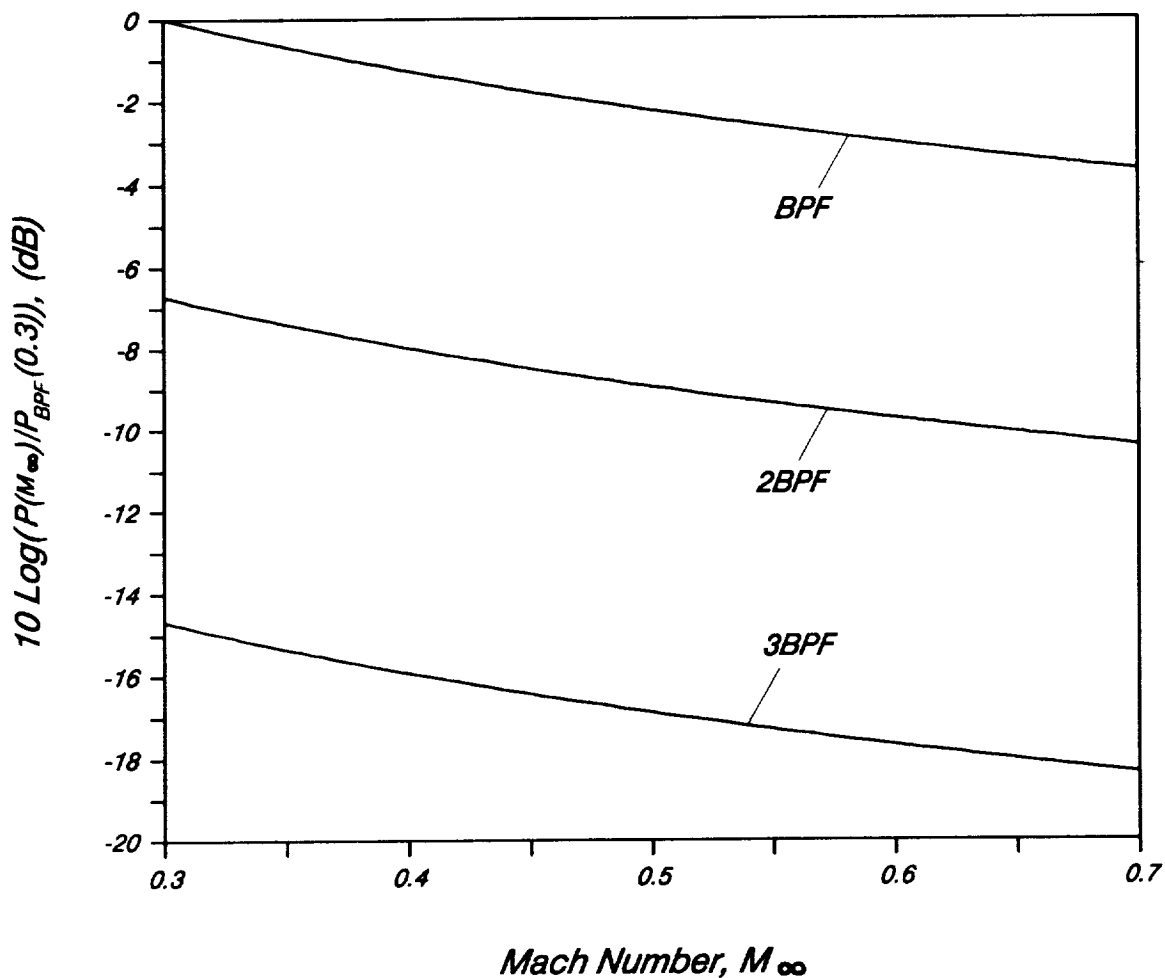
Fig. 3.15   Decibel variations of the acoustic power for the first three harmonics of the BPF noise as a function of stator row Mach number for an unswept airfoil.

30 degrees are included as well. Finally, in all the calculations in the remainder of this section, it is assumed that the wake centerline deficit velocity (see Section 2.1 for details) does not vary with the "radial" (i.e., z) coordinate. In other words, the parameter a in Eqs. (2.19) and (2.20) is set equal to zero. The influence of the wake centerline deficit velocity variations with the radial coordinate will be considered in the next chapter.

The effect of vane sweep on the noise generated by ROTOR 55 is illustrated in Figs. (3.16 - 3.20). The quantity plotted is the total acoustic power at a given harmonic of BPF, normalized by the BPF power at $\alpha = 0$, in decibels. Results for the BPF and its second and third harmonics are presented.

Fig. (3.16) shows the result for a wake with zero circumferential lean, i.e., $\Gamma = 0$. In this situation the wake upwash seen by the stator vanes consists entirely of the m = 0 convected gust spatial mode (see Eqs. (2.20)). Thus, the results in Fig. (3.16) simply correspond to decibel plots of mode m = 0 similar to those in Fig. (3.7). No substantial noise reductions are achieved until sweep angles close to the critical sweep angle are reached (recall that for this case $\alpha_{cr} = 21.8$ degrees). The noise reductions due to sweep are more pronounced for the second and third harmonics of BPF, since these harmonics correspond to higher frequencies.

The case of ROTOR 55 with a wake having a circumferential lean of 10 degrees is illustrated in Fig. (3.17). Here, substantial noise reductions are achieved for much smaller values of vane sweep. The reductions experienced by the second and third harmonics of BPF are particularly striking. For a wake with circumferential lean, the modal representation contains convected gust modes of all orders. Thus, even at fairly small sweep angles some modal components have reached their critical sweep angles.
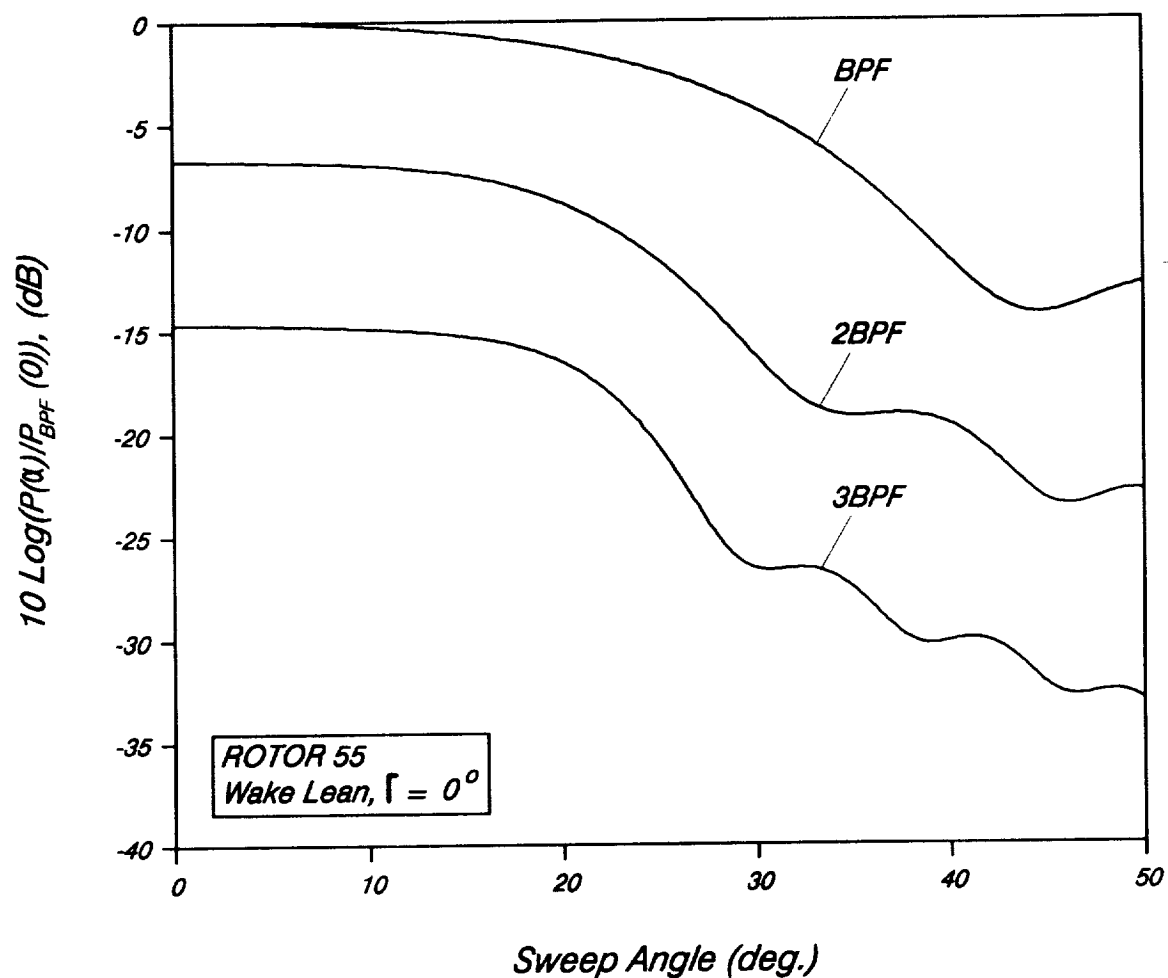
Fig. 3.16   Total acoustic power generated at the first three harmonics of BPF for ROTOR 55 with wake lean of Γ = 0 degrees.
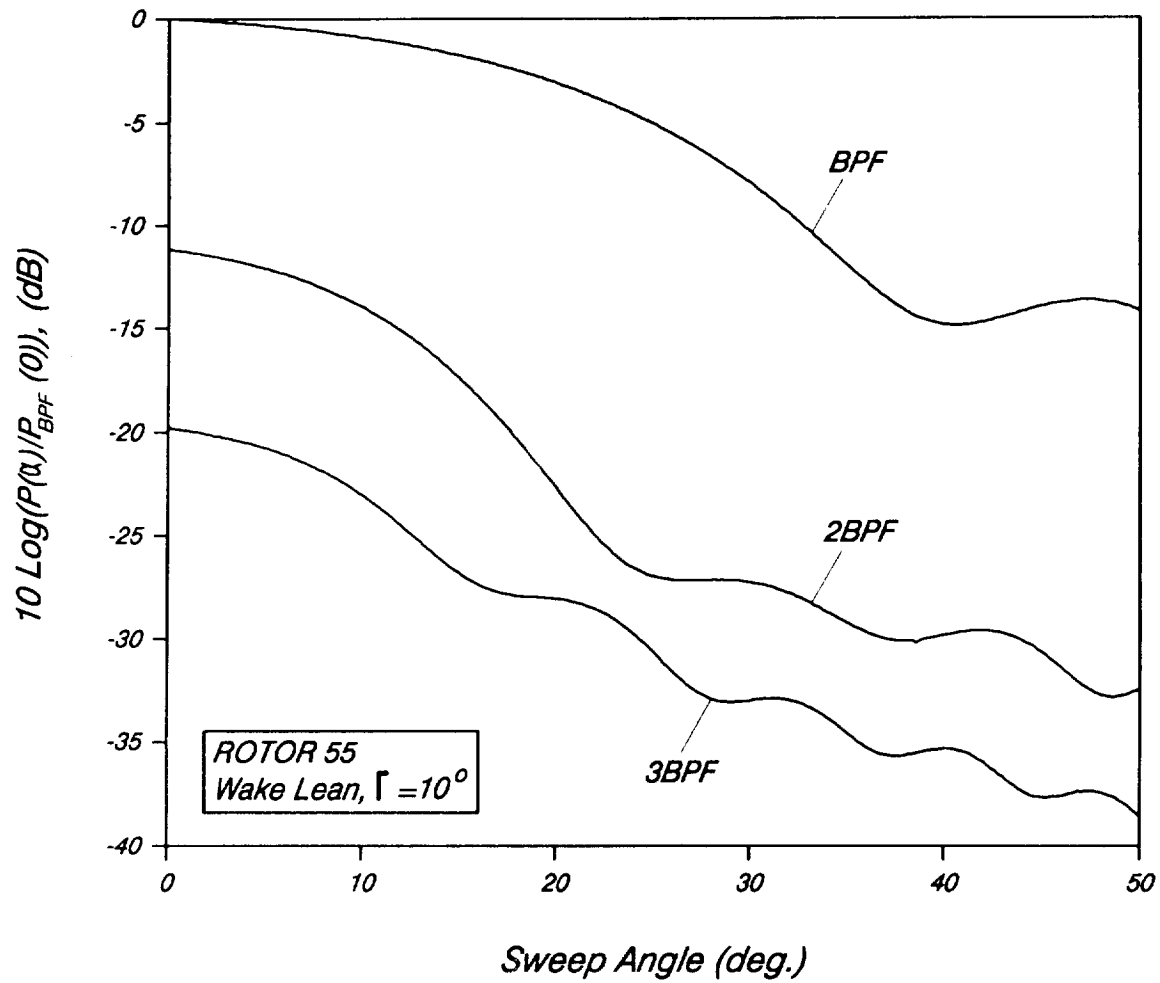
Fig. 3.17   Total acoustic power generated at the first three harmonics of BPF for ROTOR 55 with wake lean of Γ = 10 degrees.

ROTOR 55 results for wake lean of $\Gamma = 20$ degrees are presented in Fig. (3.18). This wake lean appears to be close to that which would be present in most commercial aircraft designs. For this case, the BPF shows a reduction of 10 dB at sweep angles of approximately 20 degrees. The two higher harmonics of BPF noise also show fairly substantial reductions.

Finally, the result for a wake lean of 30 degrees are illustrated in Fig. (3.19). Generally speaking, here, reductions with sweep are much less dramatic when compared with the previous case. This is particularly true for the BPF level which shows significantly slower reduction with increasing sweep angle. The main reason for this behavior can be explained in terms of the gust spanwise trace velocity. For this wake lean, only large sweep angles produce subsonic gust spanwise trace velocities, and hence appreciable noise reductions occure only for these angles. Thus, it is clear that the effectiveness of sweep is strongly influenced by wake lean.

Next, the influence of vane sweep and wake lean on the distribution of modal acoustic power is illustrated. In Fig. (3.20), the modal power information for ROTOR 55 for four different combinations of sweep and lean is plotted. The abscissa is the fraction of the total acoustic power contained in a given mode (recall that there are only two propagating radial modes in this case). The power levels are plotted versus the modal cut-off ratio[†], rather than the mode number, in conformity with the usual practice. Modes with cut-off ratios near zero are highly cut-on and quite difficult to attenuate while modes with cut-off ratios close to unity are nearly cut-off and are readily absorbed by acoustic liners. It is clear from Fig. (3.20) that both sweep and lean shift the distribution of

_____

† Actually ω/ω_{cr}, where ω_{cr} is the cut-off frequency of the mode in question. For a discussion of the concept of modal cut-off ratio see Rice (1978).
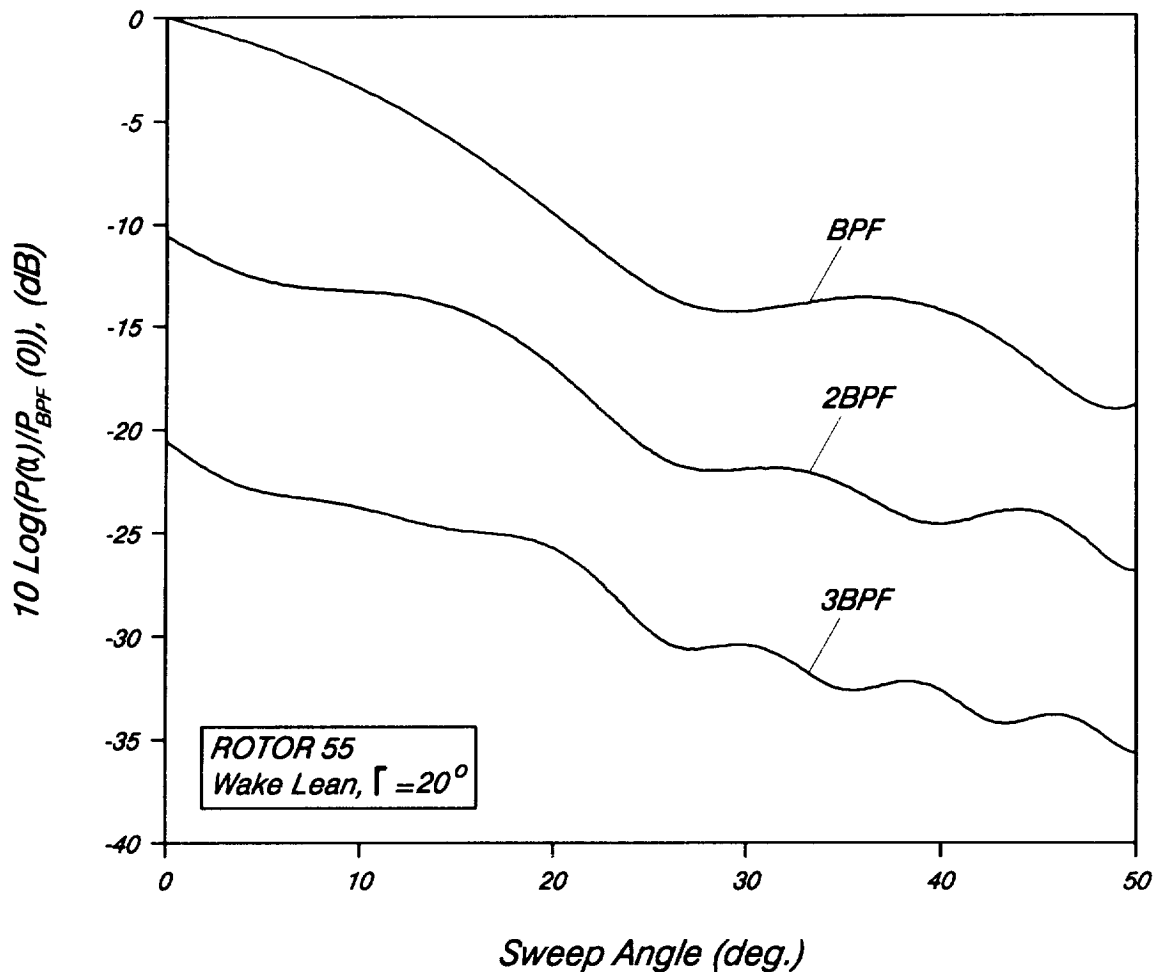
Fig. 3.18   Total acoustic power generated at the first three harmonics of BPF for ROTOR 55 with wake lean of Γ = 20 degrees.
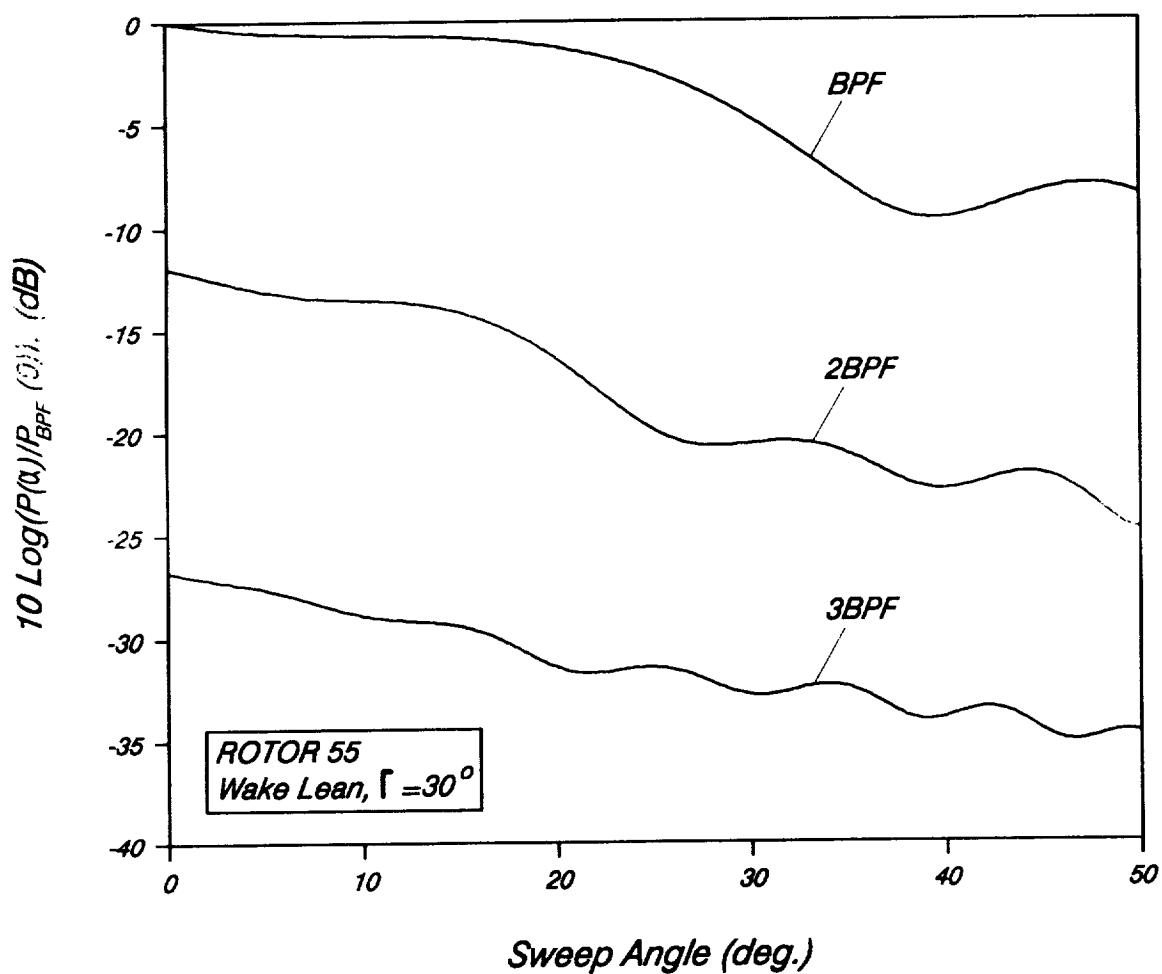
Fig. 3.19   Total acoustic power generated at the first three harmonics of BPF for ROTOR 55 with wake lean of Γ = 30 degrees.
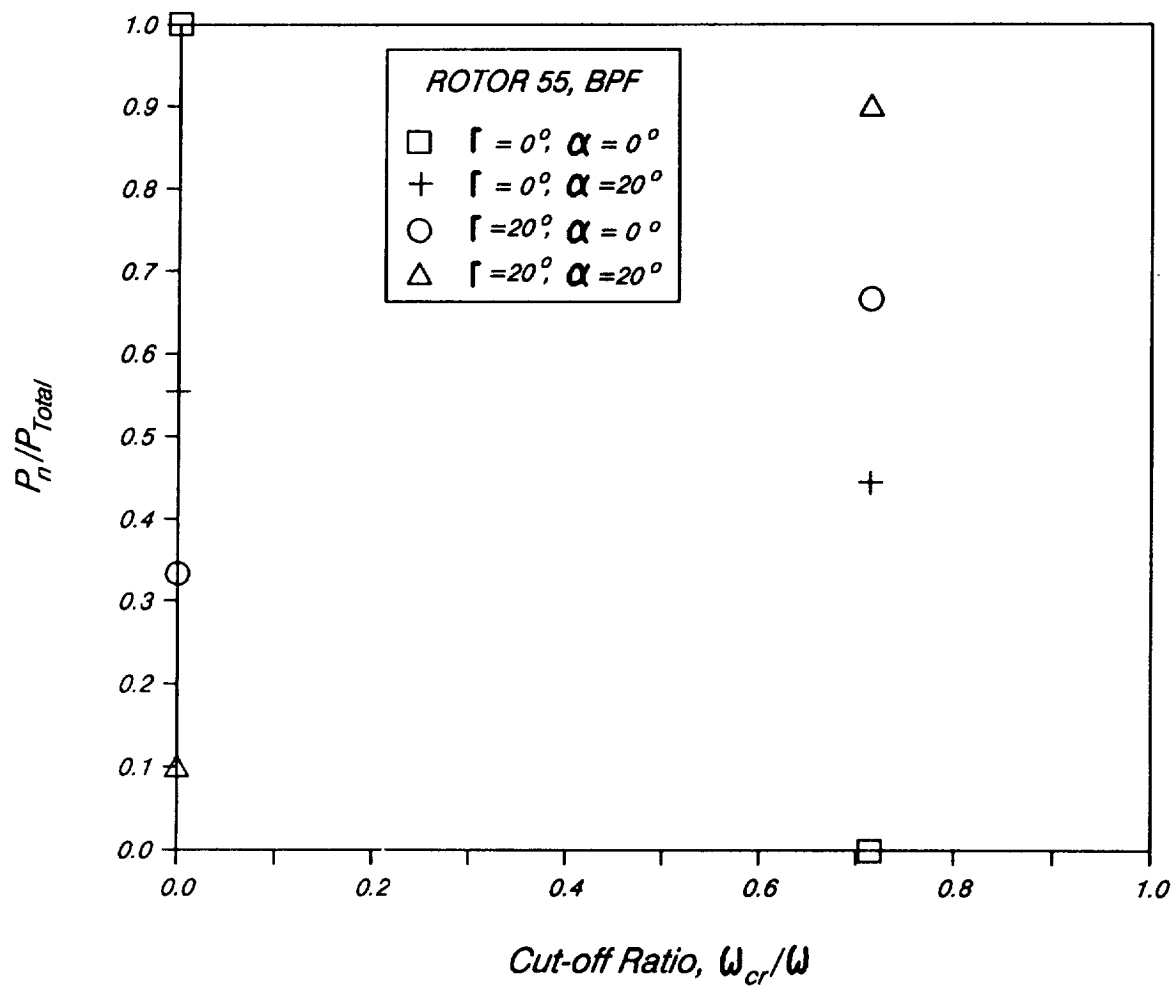
Fig. 3.20   Modal distribution of acoustic power as a function of modal cut-off ratio for ROTOR 55 at different combinations of sweep and lean.

acoustic power towards modes with higher cut-off ratios. Therefore, in addition to reducing noise levels, sweep also enhances the performance of acoustic duct liners.

The parametric results for ROTOR 11 are shown in Figs. (3.21 - 3.25). The case of a wake with no circumferential lean is presented in Fig. (3.21). As for ROTOR 55, here curves simply correspond to decibel plots of m = 0 mode results similar to those presented in Fig. (3.7). The noise level is fairly constant until sweep angles close to $\alpha_{cr} = 21.8$ degrees are reached. Then a rapid reduction in noise level occurs which is particularly dramatic for higher harmonics of BPF. For a wake with no lean, the differences in behavior between ROTOR 55 (Fig. (3.16)) and ROTOR 11 are due solely to the fact that the frequencies are much higher for ROTOR 11.

Fig. (3.22) presents results for ROTOR 11 with a wake circumferential lean of 10 degrees. Here, substantial noise reductions occur starting at sweep angles of approximately 10 degrees. At $\alpha = 15$ degrees, the power levels of second and third harmonics of BPF have decreased more than 10 dB from their zero sweep values! Recall that the modal distribution of the gust modes is influenced by both their wake circumferential lean, Γ, and by the rotor blade spacing, d_Γ (defined in Chapter 2). Since ROTOR 11 has more blades than ROTOR 55, for the same wake lean the gust mode distribution for ROTOR 11 will be weighted more heavily toward higher values of m. The differences in gust modal phase distribution and the higher frequencies for ROTOR 11 together make the noise reductions shown in Fig. (3.22) more dramatic than those in Fig. (3.17).

The case of ROTOR 11 with a wake circumferential lean of $\Gamma = 20$ degrees is presented in Fig. (3.23). Here, some noise reduction occurs at small values of the sweep angle. However, with further increases in sweep the reductions in the noise levels are not very substantial. For large sweep angles, the levels of the second and third harmonics actually
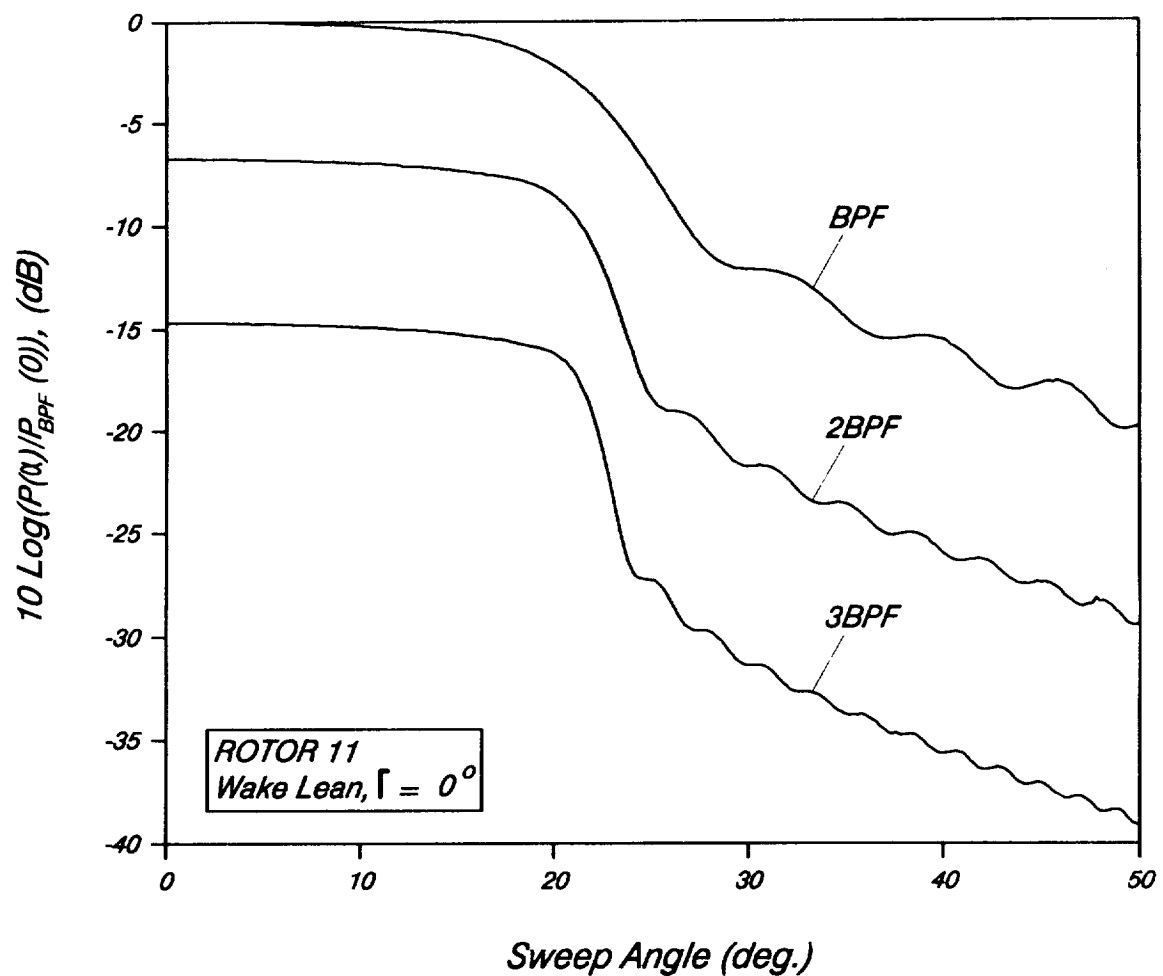
Fig. 3.21   Total acoustic power generated at the first three harmonics of BPF for ROTOR
   11 with wake lean of Γ = 0 degrees.
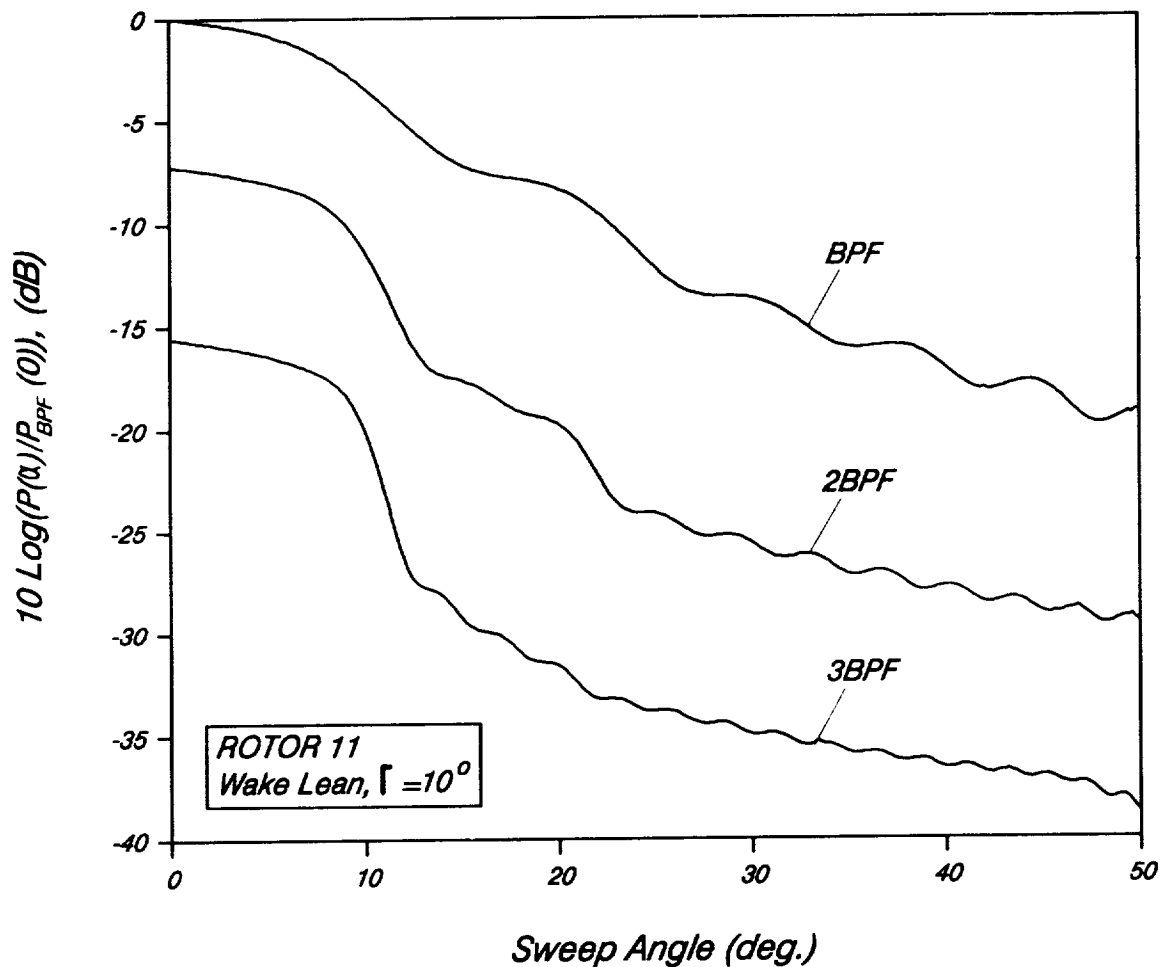
Fig. 3.22   Total acoustic power generated at the first three harmonics of BPF for ROTOR 11 with wake lean of $\Gamma = 10$ degrees.
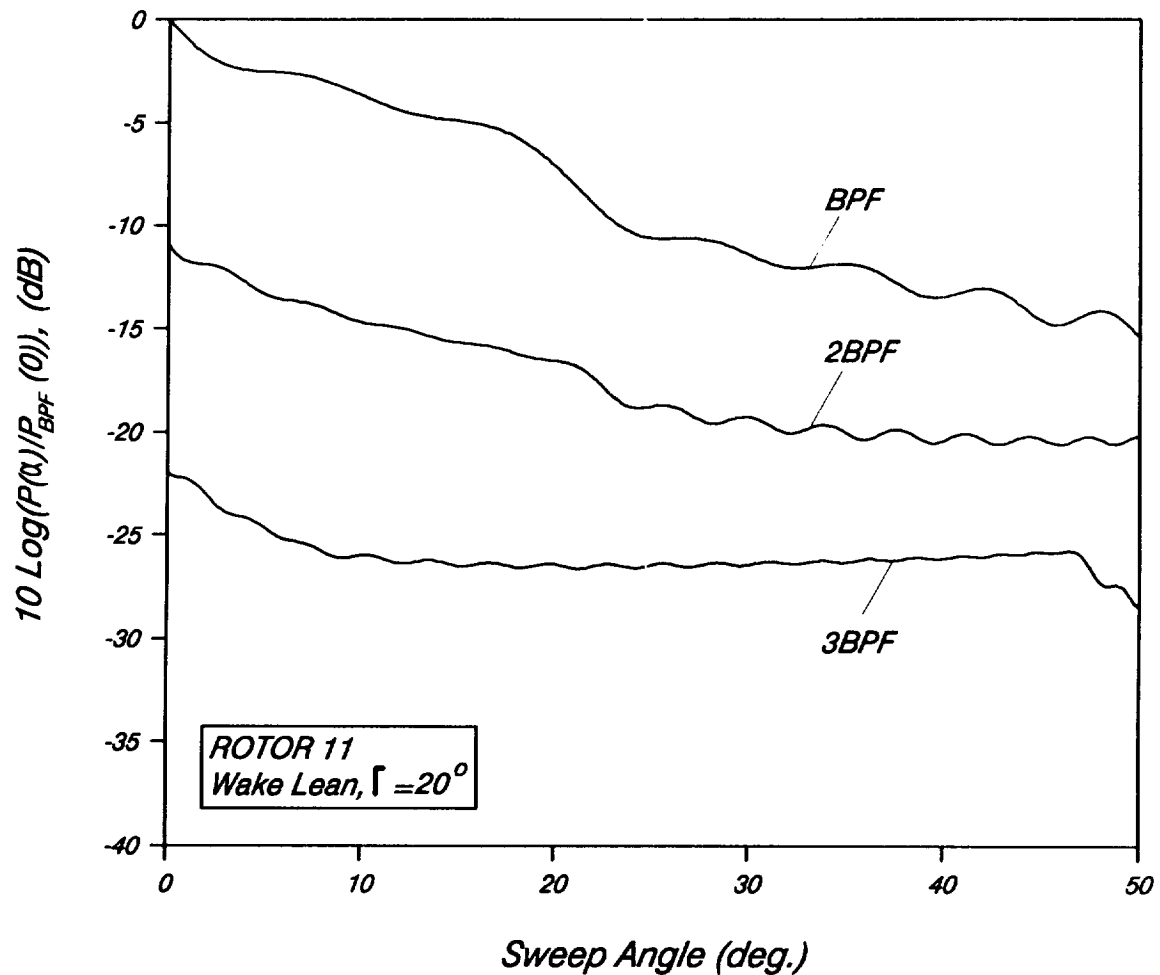
Fig. 3.23   Total acoustic power generated at the first three harmonics of BPF for ROTOR 11 with wake lean of Γ = 20 degrees.

show a slight increase. For the second and third harmonics, increasing sweep leads to supersonic spanwise gust trace velocity, and hence to an increase in noise levels.

In Fig. (3.24) the result for the wake lean of 30 degrees are presented. In this case, it is clear that sweep is not a very effective means of noise reduction. Only for large sweep angles there is an appreciable reduction on the level of the BPF noise. The level of the second harmonic initially drops slightly before starting to increase when sweep approaches large values. Over the same range, the level of the third harmonics stays essentially constant until very large sweep angles are reached when it shows a sizable reduction.

The modal distribution of acoustic power as a function of cut-off ratio for ROTOR 11 are plotted in Fig. (3.25). As before four different combinations of sweep and lean are presented. For this case there are five propagating radial modes. The effectiveness of sweep (and lean) in shifting power to modes with cut-off ratios near one is particularly obvious here.

Based on the results from both ROTOR 55 and ROTOR 11 presented so far, it is clear that the wake circumferential lean strongly influences the effectiveness of sweep. To emphasize that point, a comparison is made between the effectiveness of vane sweep in reducing the noise levels at BPF for ROTOR 11, for two cases of wake lean $\Gamma = \pm 20$ degrees. The comparison is presented in Fig. (3.26). For the wake lean of $\Gamma = +20$ degrees, all sweep angles in the range (0 to 50 degrees) result in a noticeable reduction in the level of the noise generated. In contrast, for the case of opposite wake lean, i.e., $\Gamma = -20$ degrees, vane sweep (in the same range) actually increases the noise radiated to the farfield compared with the unswept case. This effect can be most easily explained in terms of the gust spanwise trace velocity. In the present notation, for a given sweep angle,
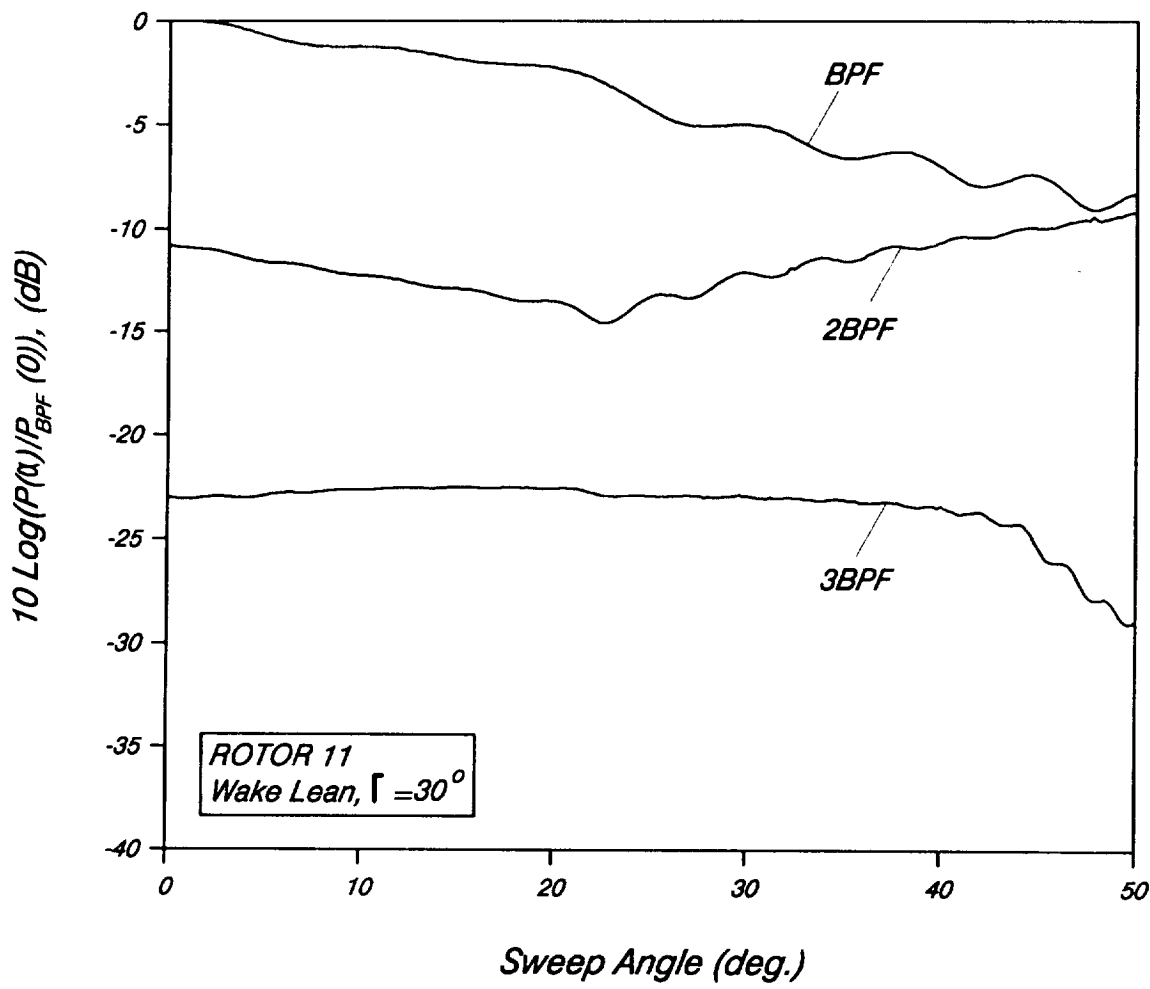
Fig. 3.24   Total acoustic power generated at the first three harmonics of BPF for ROTOR 11 with wake lean of Γ = 30 degrees.
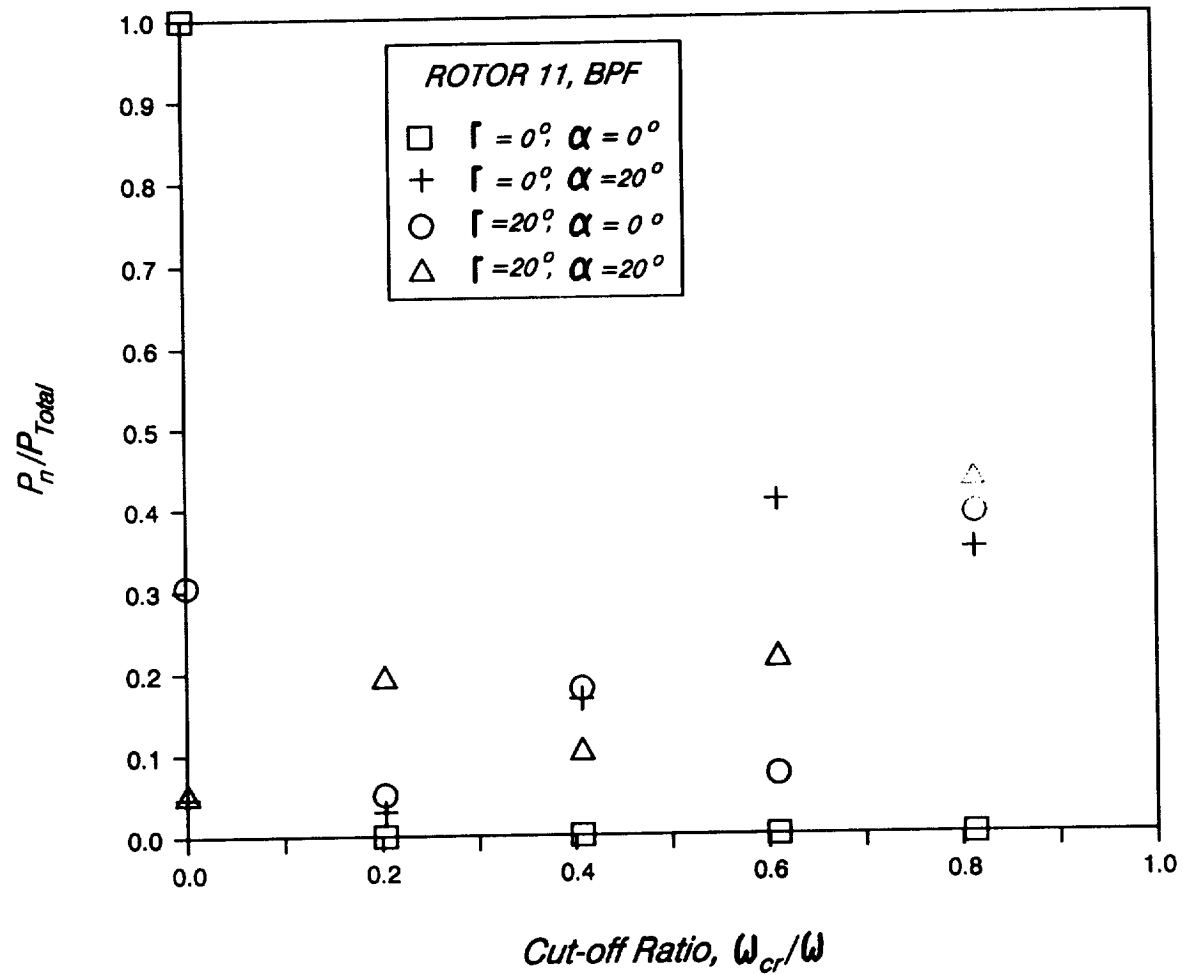
Fig. 3.25   Modal distribution of acoustic power as a function of modal cut-off ratio for ROTOR 11 at different combinations of sweep and lean.
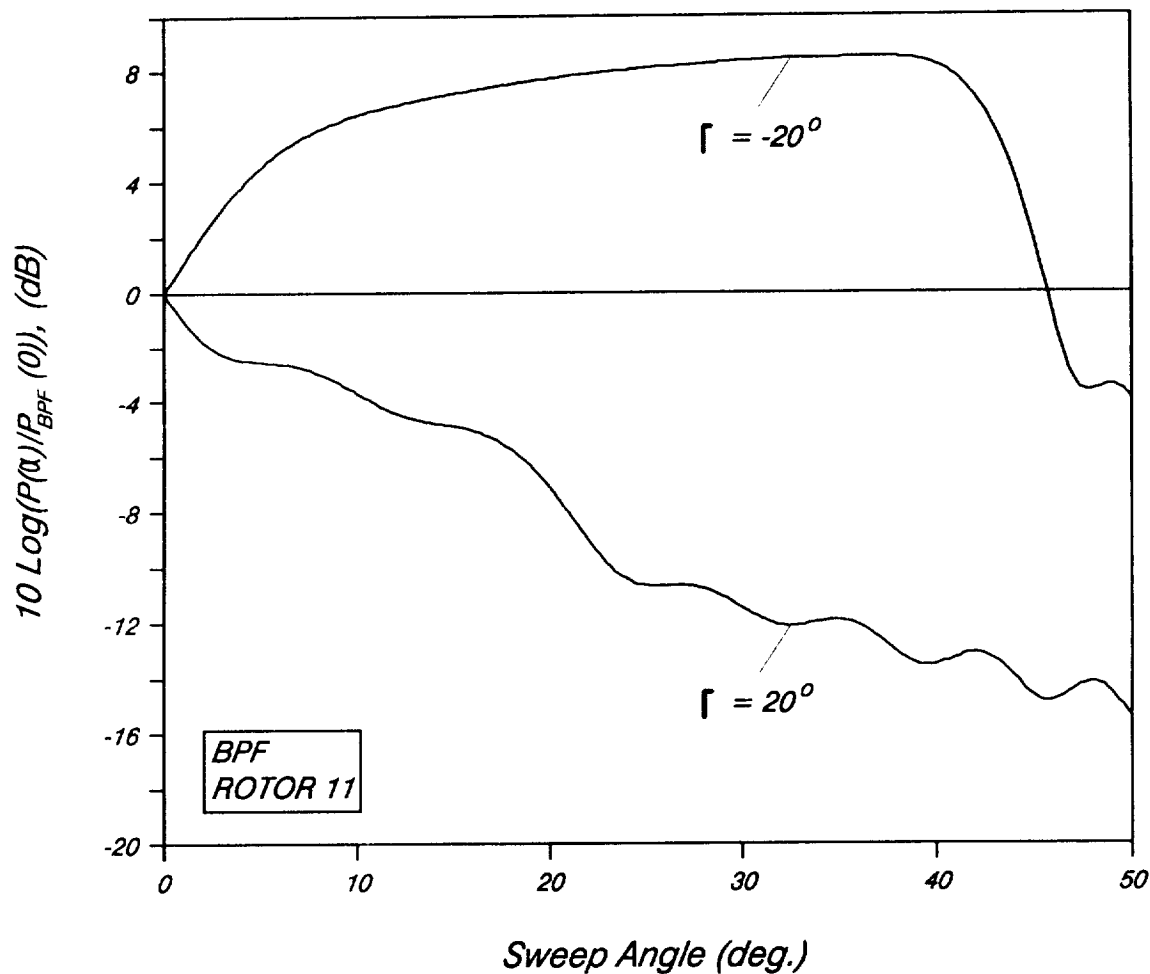
Fig. 3.26   Influence of wake lean on the effectiveness of airfoil sweep.   Results for ROTOR 11 at the BPF are illustrated.

positive wake lean (say, +20 degrees) reduces the gust relative trace velocity further below M = 1 compared to the no-sweep case and thus further enhances the effectiveness of sweep. On the other hand, negative lean (say, -20 degrees) actually causes the gust relative trace velocity to become supersonic thus, increasing the noise radiation to the farfield.

Throughout this section, the trace velocity argument has often been used to explain the general trends observed in the results. While the gust spanwise trace velocity is certainly a definite indicator of whether the generated noise field is cut-on or cut-off, it does not provide an explanation for the mechanism which is responsible for noise reduction. This mechanism is best explained in terms of an example. Consider the noise levels plotted in Fig. (3.26). At a sweep angle of, say, 30 degrees, there is roughly a 20 dB difference between the positive and negative wake lean cases. A comparison of the features of the gusts for the two cases shows that the modal content of the two gusts are very similar. In fact, as shown in Table 3.2, for this case the gust modal amplitudes are identical and the modal phases are complex conjugates. Thus, the difference must be related to the phase differences between the different gust mode orders. The crucial point is that each gust mode order generates acoustic modes of all orders. Hence, the difference in the noise levels must be in the mutual cancellation or reinforcement for a particular acoustic mode order generated by different convected gust mode orders.

To illustrate this point, the acoustic modal amplitudes generated in each of the two cases as a function of the polar angle θ are plotted in Fig. (3.27). Recall that for this case there are 5 propagating radial modes. The solid lines indicate the amplitudes corresponding to the case of Γ = -20 degrees and the dotted lines the amplitudes for the case of Γ = +20 degrees. The modal amplitudes for each acoustic mode are normalized by the same value and are plotted on the same scale to facilitate direct comparison. For the

Table 3.2 Convected Gust Modal Amplitude and Phase Information. Results for Wake Leans of Γ = +20 and Γ = -20 Degrees are Presented.

Gust Mode No.	$\Gamma = +20^o$		$\Gamma = -20^o$	
	Amplitude	Phase	Amplitude	Phase
0	0.2552E-01	0.2084E+01	0.2552E-01	-0.2084E+01
1	0.1491E-01	0.5132E+00	0.1491E-01	-0.5132E+00
2	0.2971E-01	0.2084E+01	0.2971E-01	-0.2084E+01
3	0.2106E-01	0.5132E+00	0.2106E-01	-0.5132E+00
4	0.5852E-01	0.2084E+01	0.5852E-01	-0.2084E+01
5	0.1210E+00	0.5132E+00	0.1210E+00	-0.5132E+00
6	0.9495E-01	-0.1058E+01	0.9495E-01	0.1058E+01
7	0.1978E-01	-0.2628E+01	0.1978E-01	0.2628E+01
8	0.2033E-01	-0.1058E+01	0.2033E-01	0.1058E+01
9	0.7745E-02	-0.2628E+01	0.7745E-02	0.2628E+01
10	0.1011E-01	-0.1058E+01	0.1011E-01	0.1058E+01
11	0.4405E-02	-0.2628E+01	0.4405E-02	0.2628E+01
12	0.6263E-02	-0.1058E+01	0.6263E-02	0.1058E+01
13	0.2902E-02	-0.2628E+01	0.2902E-02	0.2628E+01
14	0.4320E-02	-0.1058E+01	0.4320E-02	0.1058E+01
15	0.2075E-02	-0.2628E+01	0.2075E-02	0.2628E+01
16	0.3181E-02	-0.1058E+01	0.3181E-02	0.1058E+01
17	0.1566E-02	-0.2628E+01	0.1566E-02	0.2628E+01
18	0.2449E-02	-0.1058E+01	0.2449E-02	0.1058E+01
19	0.1227E-02	-0.2628E+01	0.1227E-02	0.2628E+01
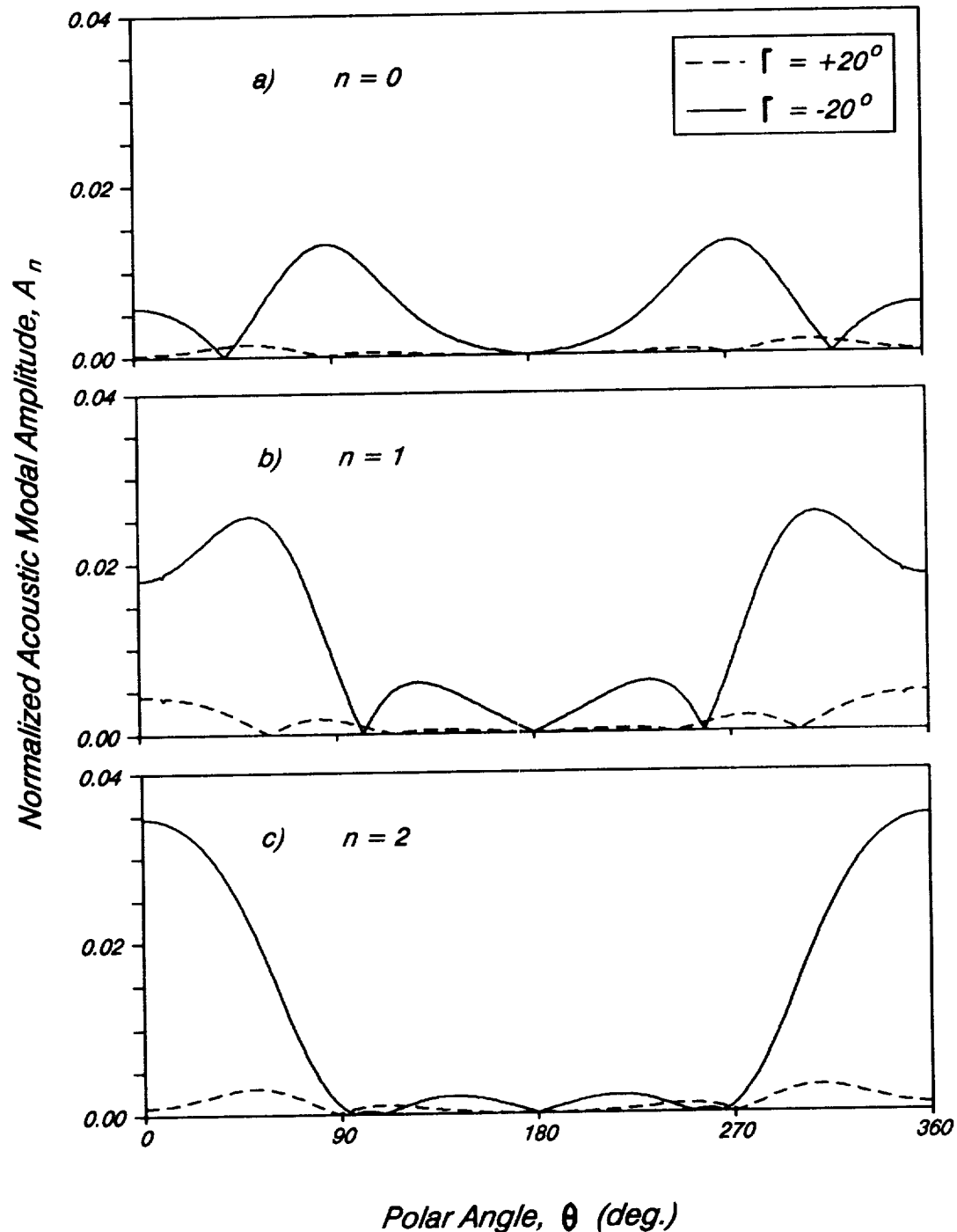
Fig. 3.27   Acoustic modal amplitudes as a function of polar angle θ. Results for wake
leans of Γ = +20 and Γ = -20 degrees are presented.
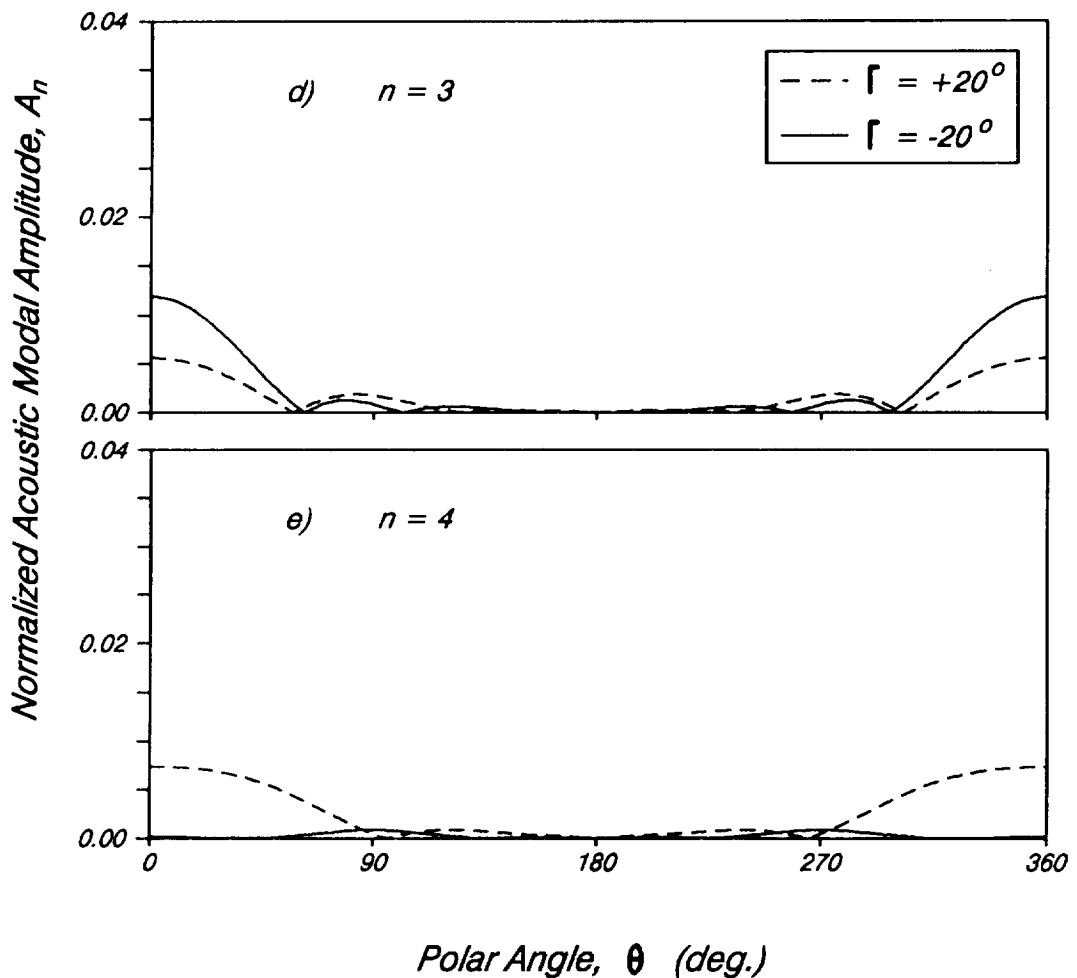
Fig. 3.27--continued.

most part, the acoustic modal amplitudes generated by the wake with negative lean are appreciably larger than those generated by the wake with positive lean. Here, mutual phase reinforcement between different gust mode orders leads to higher acoustic modal amplitudes for the wake with -20 degrees lean. In contrast, mutual phase cancellation between different gust mode orders sharply reduces the acoustic modal amplitudes for the wake with lean of +20 degrees. These results clearly show the mutual phase interaction mechanism described above.

In connection with the above discussion, it is interesting to compare the noise levels that would be produced by a gust with "random" (i.e., incoherent) modal phases with those produced by an actual gust where account is made for mutual phase interactions. For the former case, the acoustic power produced by each convected gust mode is calculated separately and the result is added to contributions from other gust mode orders without regard to mutual phase relationships. In Fig. (3.28), comparative results for the BPF noise as a function of sweep angle for a typical case of $\Gamma = 20$ degrees are presented. Clearly, over the entire range of sweep angles, the power level generated by the random gust is significantly higher than that for an actual gust indicating, once again, that the mutual phase interaction mechanism plays an important role in the noise generation/reduction process.

In summary, the present parametric calculations indicate that vane sweep can produce substantial reductions of noise generated by the interaction of stator vanes with the rotor viscous wake. It is found that wake lean significantly influences the effectiveness of sweep. Vane sweep must be chosen to enhance the natural phase lag caused by wake lean. For example, for a Mach number of 0.4, in the case of a wake with no lean roughly 25 degrees of vane sweep is required to produce substantial noise reductions while for

100
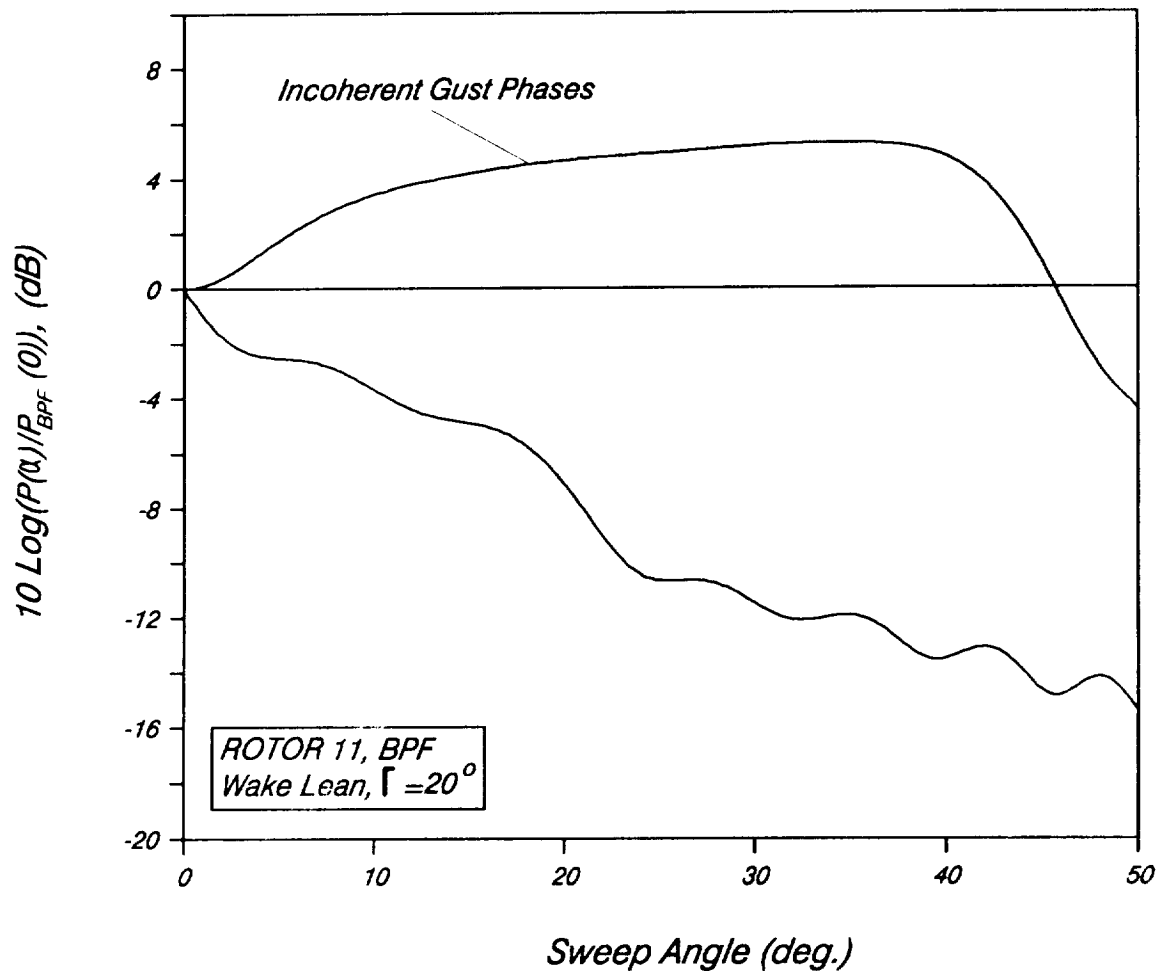
Fig. 3.28   Influence of gust modal phase interactions on the generated noise levels as a
function of sweep. Results for ROTOR 11 at the BPF and wake lean of $\Gamma = 20$
degrees are presented.

101

a wake with 20 degrees of lean noise reductions on the order of 10 dB were found for sweep angles as small as 5 degrees. Thus, based on these preliminary results, it appears that vane sweep is a promising means of reducing rotor-stator interaction noise. Quantitative assessments of the effectiveness of vane sweep in reducing rotor-stator interaction noise in realistic situations will be presented in the next chapter.

CHAPTER 4

CASCADE MODEL AND
PARAMETRIC STUDY OF ROTOR-STATOR INTERACTION NOISE

In this chapter, an approximate solution to the problem of the noise generated by the interaction of a convected gust with a cascade of finite span swept airfoils is first developed. Then this solution is utilized in a parametric study to assess the effectiveness of vane sweep in abating rotor-stator interaction noise. Finally, a summary of conclusions drawn from this study is presented.

4.1 Approximate Cascade Solution

In mathematical terms, the problem of noise generated by gust-cascade interaction is equivalent to the reflection and transmission of electromagnetic (or acoustic) waves by an infinite set of parallel plates. In the context of the electromagnetic wave reflection and transmission problem, Carlson and Heins (1946), Heins and Carlson (1947), and Heins (1950) used a Green's function formulation in conjunction with the Fourier transform method and the Wiener-Hopf technique to obtain a solution. More recently, Mani and Horvay (1970) used Fourier transforms and the Wiener-Hopf technique in a dual integral equation formulation to find a solution to the problem of reflection and transmission of acoustic waves by a blade row. In either case, the Wiener-Hopf formulation involves finding a multiplicative split of a function which essentially represents the periodicity of the solution in the lateral (in this notation the y-) direction. The split is carried out utilizing the infinite product factorization of that function into two parts that are analytic in the upper and lower halves of the transform plane, respectively.

103

Unfortunately, the solution obtained by either of the two formulations mentioned above is computationally inefficient to use at high frequencies. The inefficiency at high frequencies is due to the slow convergence rate of the infinite product factors involved in the solution representation. As the frequency parameter is increased a larger number of terms in the infinite product factors must be taken into account for the solution to converge. In view of the difficulties involved in using a solution obtained by the methods mentioned above, a high-frequency approximate solution has been developed which is computationally far more efficient.

In developing an approximate high-frequency solution for the cascade problem, advantage is taken of the weak coupling between adjacent airfoil leading edges. This is similar to the approximation introduced in the single vane solution of Chapter 3. Recall that there the coupling between the leading- and trailing-edge responses was neglected. The basic idea of weak coupling between adjacent leading edges is illustrated in Fig. (4.1). The interaction of the convected gust with a particular airfoil generates acoustic waves (or, equivalently, acoustic rays) which emanates from the airfoil leading edge. These acoustic rays either propagate directly to the farfield or are reflected by the surfaces of the adjacent airfoils. In addition, one ray strikes the leading edge of each adjacent airfoil and is diffracted. The diffracted field is weaker by $O(k_x^{-1/2})$ as compared to the direct and reflected fields, and hence can be neglected for sufficiently high frequencies. For the upstream radiated noise the reflected waves can also be ignored. Thus, an approximate solution for the problem of upstream radiated noise from a cascade can be developed by simply adding the acoustic farfields emanating from the infinite row of leading edges. In this work, attention is focused on the upstream radiated noise only, and hence the
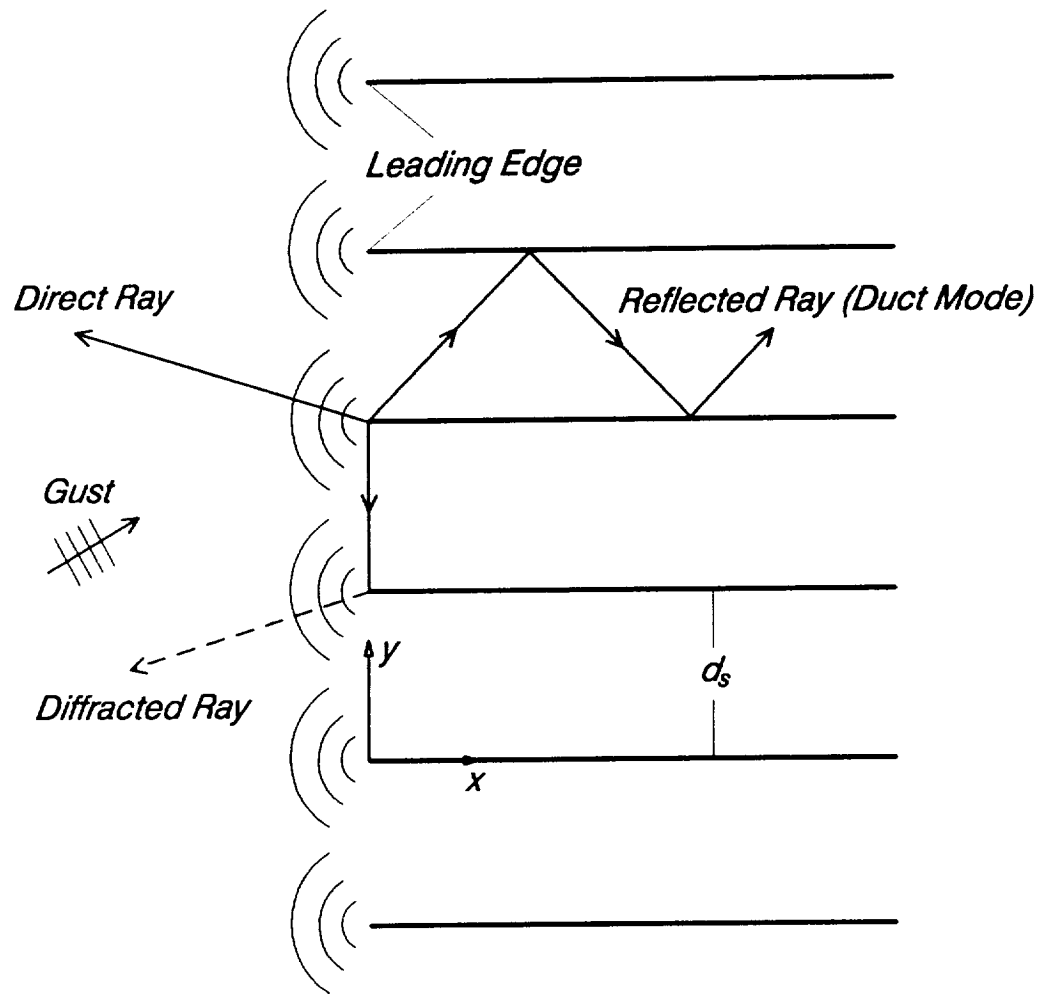
Fig. 4.1   Noise radiation for an airfoil cascade as a sum over the individual airfoil noise
fields.   The direct and reflected rays (solid lines) and diffracted rays (dashed
lines) are illustrated.   Here only the orthogonal coordinate system is shown (z is
out of the paper).

downstream radiated noise is not considered. However, for completeness, some general comments on ways to account for the downstream radiated noise are included in Chapter 5.

Consider an infinite row of finite span swept airfoils interacting with a convected gust. Let the gust be described by

$$v_m(x,y,z,t) = b_m \, e^{i(k_x \, x \, + \, k_y \, y \, - \, k_x \, U_\infty \, t)} \cos m\pi z \tag{4.1}$$

where the coordinate system (x,y,z) is chosen to coincide with the zeroth airfoil. The transverse spacing between the adjacent airfoils is d_s. The cascade is assumed to have zero stagger angle, and hence the local coordinate system of the qth airfoil is related to that of the zeroth airfoil by

$$x_q = x, \qquad y_q = y - qd_s, \qquad z_q = z, \qquad q = 0, \pm 1, \pm 2, \cdots . \tag{4.2}$$

In the local coordinate system of the qth airfoil then, the convected gust acquires the form

$$v_m(x_q,y_q,z_q,t) = b_m \, e^{i(k_x \, x_q \, + \, k_y \, y_q \, - \, k_x \, U_\infty \, t)} \, e^{ik_y \, qd_s} \cos m\pi z_q . \tag{4.3}$$

This is similar to Eq. (4.1) referred to the coordinate system of the zeroth airfoil, but modified by a phase shift factor. The isolated airfoil solution for qth airfoil must also be related to the solution for zeroth one, denoted here by $\phi_{m,o}(x,y,z,t)$, by the same phase factor. Hence, one can write

$$\phi_{m,q}(x_q,y_q,z_q,t) = \phi_{m,o}(x,y_q,z) \, e^{iqk_y d_s} . \tag{4.4}$$

Upon summing the contributions from all airfoils and using Eq. (4.4), the cascade solution is given by

$$\Phi_m(x,y,z,t) = \sum_{q=-\infty}^{+\infty} \phi_{m,o}(x,y_q,z) \, e^{iqk_y d_s} . \tag{4.5}$$

106

If the mutual interactions between airfoils are neglected, $\phi_{m,o}(x,y,z,t)$ is given by the isolated airfoil solution derived in the previous chapter (i.e., Eqs. (3.32) and (3.34)). Equation (4.5), then, represents a high-frequency approximate solution to the problem of a convected gust interacting with a cascade of finite span swept airfoils.

While, in principle, it is possible to compute the infinite sum in Eq. (4.5) directly, in practice this approach is not very useful. The difficulty is apparent simply by noting that, as the observation point moves further upstream, an increased number of airfoil leading edges are approximately the same distance away from the observation point and thus make non-negligible contributions to the infinite sum. In order to avoid this difficulty, the Dirac delta function is utilized to represent the infinite summation inside an integral. One can then rewrite the sum in an eigenfunction expansion and evaluate the remaining integral by the method of the steepest descent for large upstream distances. The advantage of this approach is that only a finite number of circumferential eigenfunctions correspond to propagating modes. This occurs, because beyond moderate distances upstream of the cascade, the contributions from the cut-off modes are negligible and the infinite summation is effectively replaced by a finite sum over the cut-on modes.

Upon introducing the Dirac delta function, Eq. (4.5) may be re-expressed as

$$\Phi_m(x,y,z,t) = \sum_{q=-\infty}^{+\infty} \int_{-\infty}^{+\infty} \phi_{m,o}(x,Y,z) \, e^{ik_y q d_s} \, \delta(Y - y + q d_s) \, dY \qquad (4.6)$$

where Y is a dummy variable.

Next, the order of integration and summation is reversed. Then, using the Poisson sum formula, the infinite series of delta functions can be written in terms of an eigenfunction expansion in the y-direction (i.e., circumferential). The result is given by

$$\sum_{q=-\infty}^{+\infty} e^{ik_y qd_s} \, \delta(Y - y + qd_s) = \frac{1}{\sqrt{2\pi} \, d_s} \sum_{l=-\infty}^{+\infty} e^{i(k_y + 2\pi l/d_s)(y - Y)} \, . \tag{4.7}$$

Upon substituting the eigenfunction expansion into Eq. (4.6) and reversing the order of summation and integration again, one obtains

$$\Phi_m(x,y,z,t) = \frac{1}{\sqrt{2\pi} \, d_s}$$

$$x \sum_{l=-\infty}^{+\infty} e^{i(k_y + 2\pi l/d_s)y} \int_{-\infty}^{+\infty} \phi_{m,o}(x',Y,z) \, e^{-i(k_y + 2\pi l/d_s)Y} \, dY \, . \tag{4.8}$$

Next, the Prandtl-Glauert coordinate system (x',y,z) defined in the previous Chapter 2 (see Eq. (2.22)) is introduced. Substituting for $\phi_{m,o}(x',Y,z)$ from Eqs. (3.32) and (3.34), and grouping terms together, the following expression is obtained

$$\Phi_m(x',y,z,t) = \frac{\gamma \, b_m \, e^{i\pi/4}}{2\pi d_s \, (1-\gamma^2)^{3/4}} \sum_{l=-\infty}^{+\infty} \sum_{n=0}^{n'} \epsilon_{m,n} \frac{\cos n\pi z}{\sqrt{\kappa + W_n}}$$

$$x \int_{-\infty}^{+\infty} |sgn(Y)| \, D_{m,n,l}(\theta) \, e^{i\sqrt{1-\gamma^2} \, W_n \, \sqrt{x'^2 + Y^2}} \, e^{-i(k_y + 2\pi l/d_s)Y} dY \tag{4.9}$$

Here, $D_{m,n,l}(\theta)$ represents all the θ-dependence of $\phi_{m,o}(x',y,z,t)$ as given by Eqs. (3.32) and (3.34). Note that, since $(r,\theta) = ((x'^2 + Y^2)^{1/2}, \tan^{-1}(Y/x'))$, θ, and consequently $D_{m,n,l}(\theta)$, depend on the variable Y.

Now, for large negative x', i.e., far upstream of the cascade row, the asymptotic behavior of the last integral may be obtained by the method of steepest descent. Since the procedure is rather routine, only the final result is quoted here. It is given by

108

$$\Phi_m(x',y,z,t) = \sum_{n=0}^{n'} \sum_{l=l_1}^{l_2} \epsilon_{m,n} \frac{i\gamma \, b_m}{2\sqrt{2\pi} \, d_s \, (1-\gamma^2)^{3/4}} \frac{\cos n\pi z}{\sqrt{\kappa + W_n}} D_{m,n,l}(\theta_s)$$

$$\times e^{i(-\sigma x' + \tau y) - ik_x U_\infty t + 2\pi ij s \tan \psi} , \qquad (4.10a)$$

$$\sigma = \sqrt{k_x^2 \frac{M_\infty^2}{\beta_\infty^2} - (n\pi)^2 - \tau^2} + k_x \frac{M_\infty^2}{\beta_\infty} ,$$

$$\tau = k_y + \frac{2\pi l}{d_s} , \qquad (4.10b)$$

$$\theta_s = \sqrt{\frac{(k_x M_\infty/\beta_\infty)^2 - (n\pi)^2}{(k_x M_\infty/\beta_\infty)^2 - (n\pi)^2 - \tau^2}}$$

where $\theta_s = \tan^{-1}(Y_s/x')$ represents the saddle point. The limits l_1 and l_2 include all values of l for which σ is real. It is clear now that for a point at upstream farfield only a finite number of circumferential modes are cut-on (i.e., propagate). Note that Eqs. (4.10) describe a finite sum of oblique plane acoustic waves. Thus, an infinite number of cylindrical acoustic waves emanating from the leading edges of the airfoils have combined to form a finite number of plane acoustic waves.

Equations (4.10) represent the approximate high-frequency solution for the upstream radiated noise generated by the interaction of a convected gust with a cascade of finite span swept airfoil. This cascade model is utilized in the next section in a parametric study to assess the effectiveness of vane sweep in reducing rotor-stator interaction noise in realistic situations.

109

4.2 Parametric Study

In this section, calculations of noise generated by the interaction of rotor viscous wakes with swept stator blades are presented. The calculations presented are typical of a turbofan engine at approach operating conditions. For all calculations presented, the Mach number through the stator row is $M_{\infty} = 0.4$. Conditions are chosen such that the blade-passing frequency (BPF) is cut-on. In most cases, results for the first three harmonics of BPF are presented. As in Chapter 3, the acoustic power results are presented in terms of ratios and thus the results are independent of the magnitude of the wake deficit and of its half-width.

A number of rotor blade and stator vane combinations were investigated. Detailed results for the first three harmonics of the BPF acoustic power of a representative combination, a 22 blade rotor and a 14 vane stator referred to as 22 - 14 case, are chosen for presentation. For cases involving similar blade/vane ratios, but different counts, the general trends follow those presented for the single vane model (in Chapter 3) where comparisons were made between cases involving 15 and 44 rotor blades. The number of rotor blades (or equivalently the frequency) does not affect the general trends, but the changes with sweep are more accentuated as the blade count increases.

Before proceeding with the discussion of the 22 - 14 case, some comparisons between the results of the single vane model and a cascade simulation having 44 rotor blades and 1 stator vane, referred to as 44 - 1 case, are presented. These calculations serve to validate the cascade model as well as to point out trends in a simplified setting. The calculations presented in Chapter 3 considered the total power generated by an isolated swept stator blade, i.e., the intensity was integrated over θ from 0 to 2π. Since the present

110

cascade model considers only upstream radiated noise, in the single vane results presented here the integration was restricted to the forward arc, $\theta = \pi/2$ to $3\pi/2$.

Figures (4.2 - 4.6) are comparisons of the single vane model and the 44 - 1 case for different wake circumferential leans. In each figure, total acoustic power as a function of sweep angle for the first three harmonics of the BPF is plotted. The ordinate is the decibel level of the ratio of the acoustic power at sweep angle α relative to its value for the BPF at $\alpha = 0$. Isolated vane results are plotted as dotted lines. It is seen that the general trends for the single vane and the 44 - 1 model are very similar, with the cascade result exhibiting fairly small undulations about the single vane result. The amount of undulations is a function of the number of modes involved. Strong undulations are found when only a few propagating modes are present and as the number of propagating modes increases this feature disappears. This behavior may be described as follows. The total power for a given harmonic of BPF is the sum of the modal power contained in each of the propagating modes. The amplitudes of these modes oscillate as phase variations due to sweep cause constructive and destructive interference. These phase variations are dependent on the order and direction of propagation of the mode and thus as the number of modes increases these effects average out reducing the amplitude of the oscillations. The rapidity of the oscillations increases with frequency, since the wavelength becomes shorter and a given shift in physical location represents a larger phase shift. These effects are particularly apparent when the behavior of the acoustic power level at BPF is contrasted with that of its higher harmonics. In comparison with the BPF, the second and third harmonic components have twice and thrice as many propagating circumferential modes, respectively. As a result, while the number of undulations about the corresponding

111

single vane results have doubled and tripled, their amplitudes have decreased proportionally. Hence, one can view the single vane result as a limit for which an infinite number of circumferential modes propagate.

In Fig. (4.2) the power levels corresponding to the case of zero wake lean (i.e., $\Gamma = 0$ degrees) are plotted. The trends are quite similar for all three harmonics. Here sweep does not produce significant noise reductions until α exceeds 20 degrees. Recall that, for an infinite span airfoil, the critical sweep angle which produces a subsonic spanwise gust trace velocity is $\alpha_{cr} = 21.8$ degrees (see Fig. 3.6).

The results for the case of $\Gamma = 10$ degrees are shown in Fig. (4.3). Here, wake lean produces a phase lag at the tip relative to the hub and the introduction of sweep enhances this phase lag. Small sweep angles produce subsonic spanwise trace velocities, and hence the noise level is reduced. For this case, 10 degrees of sweep leads to roughly 10 dB reductions in the level of all three harmonics.

The case $\Gamma = 20$ degrees, shown in Fig. (4.4), corresponds to a wake lean typical of many turbofan designs. Here the noise reductions begin as soon as sweep is introduced. However, the overall reductions are less dramatic. In this case, the reductions due to sweep in the power level of some modal components are more or less offset by the increases in the power level of the others resulting in only moderate overall reductions.

Increasing the wake lean further actually begins to nullify the effectiveness of sweep in reducing the noise. This point is illustrated in Fig. (4.5) where wake lean is 30 degrees. Here the reductions in noise levels barely exceed 8 dB for any of the three harmonics over the entire range of displayed sweep angles. The level of the second harmonic actually increases as the sweep is increased beyond 20 degrees. In this case

112
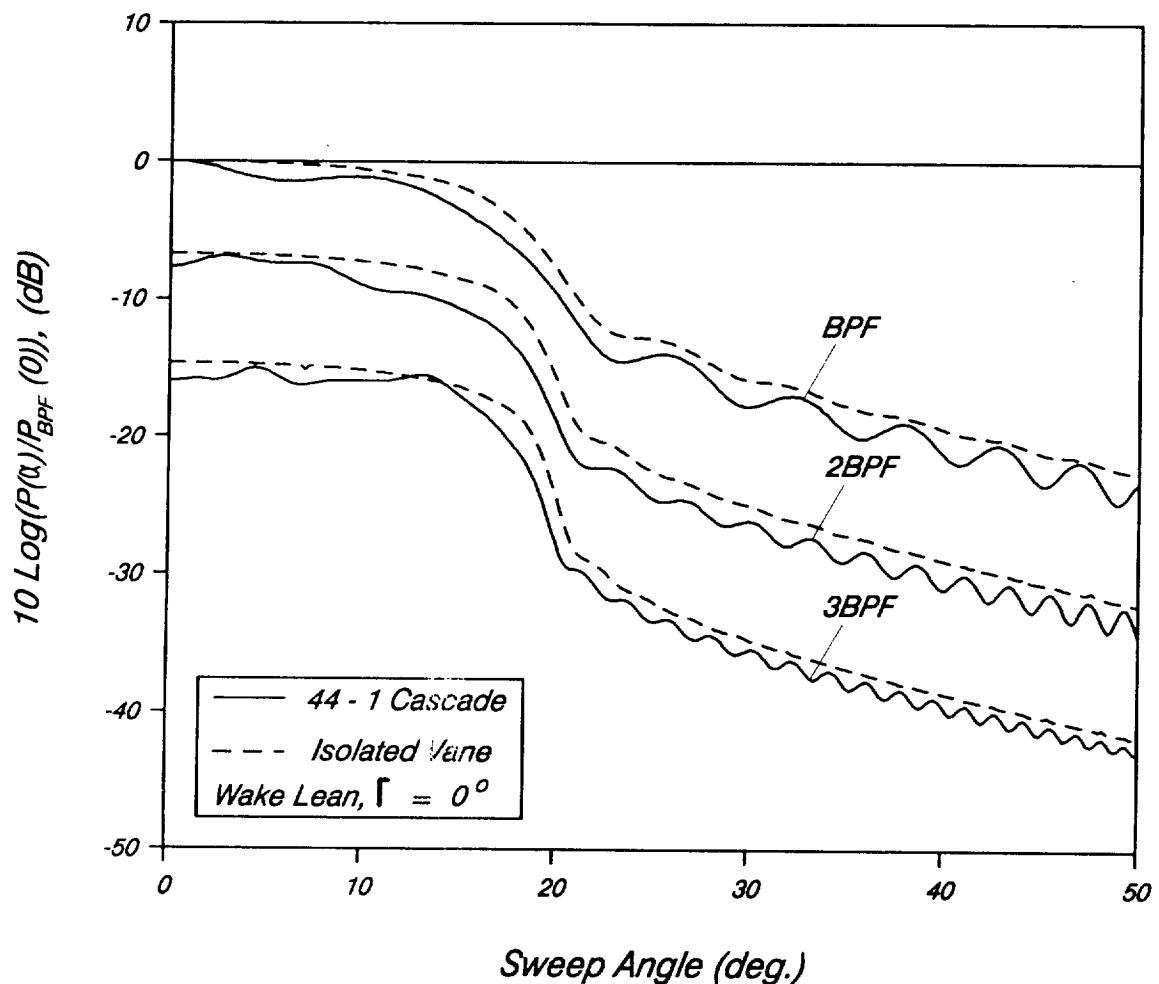
Fig. 4.2   Acoustic power generated by 44 - 1 cascade at the first three harmonics of BPF with a wake lean of $\Gamma = 0$ degrees. The acoustic power generated by an isolated airfoil is shown as a dashed line for comparison.

113
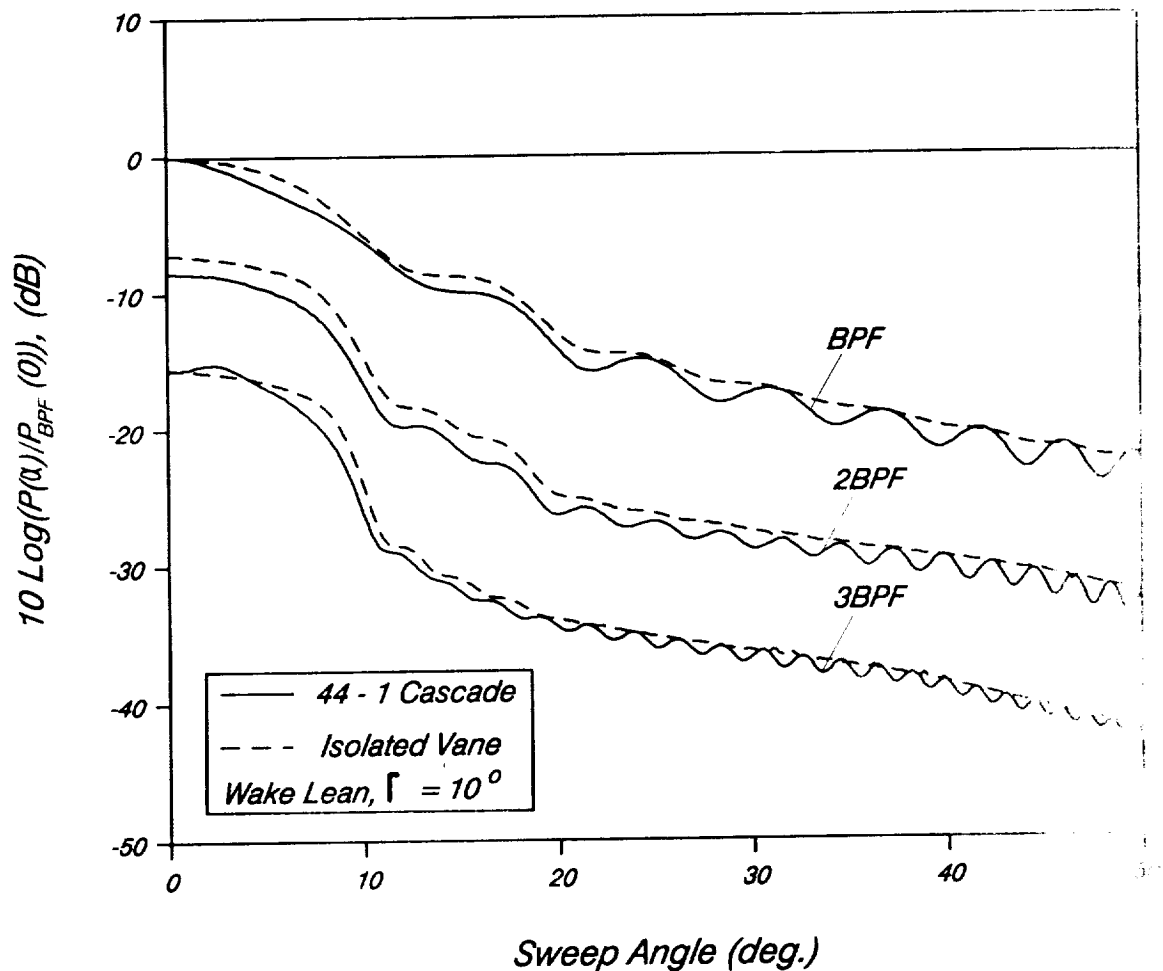
Fig. 4.3   Acoustic power generated by 44 - 1 cascade at the first three harmonics of
with a wake lean of $\Gamma = 10$ degrees. The acoustic power generated by
isolated airfoil is shown as a dashed line for comparison.

114
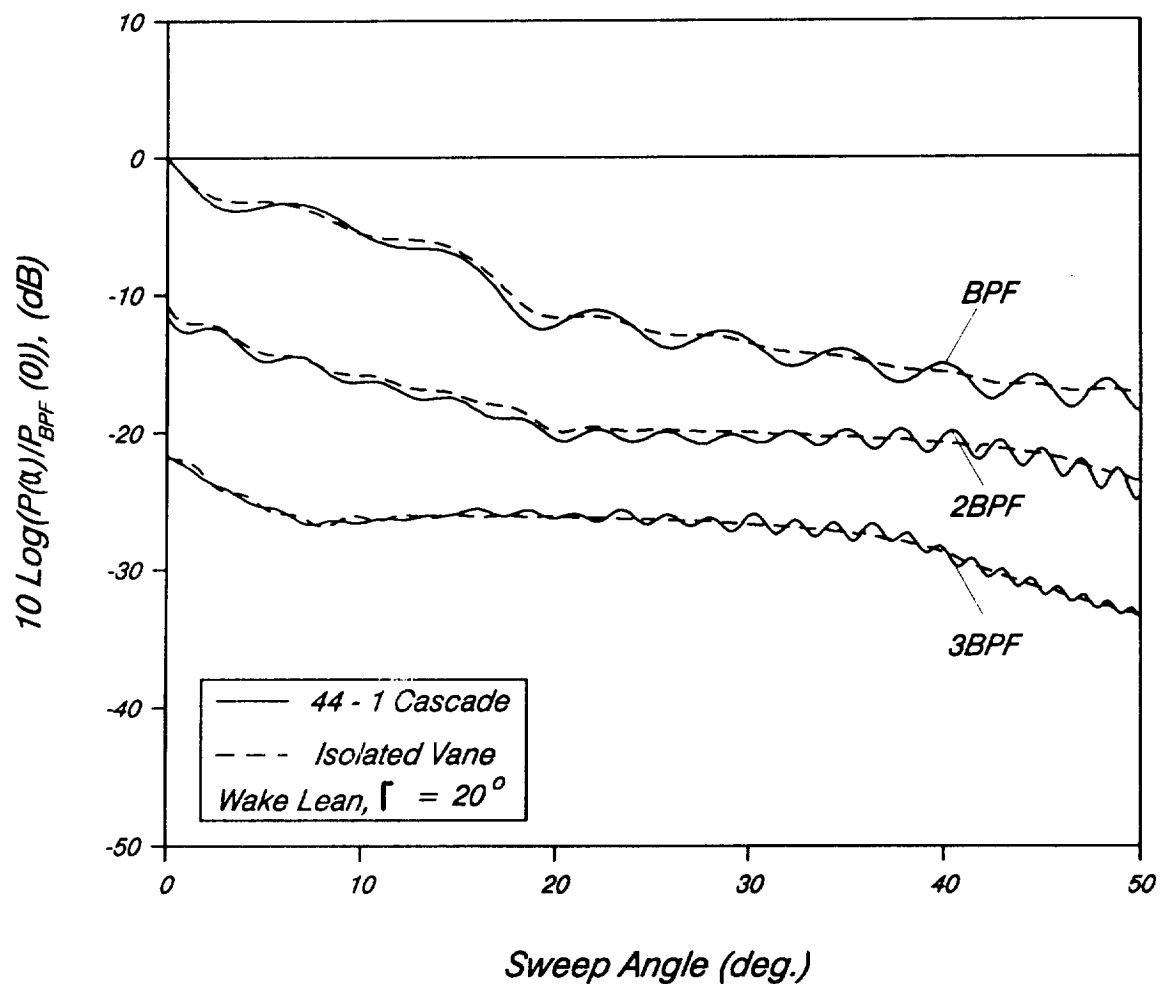
Fig. 4.4   Acoustic power generated by 44 - 1 cascade at the first three harmonics of BPF
with a wake lean of Γ = 20 degrees. The acoustic power generated by an
isolated airfoil is shown as a dashed line for comparison.

115
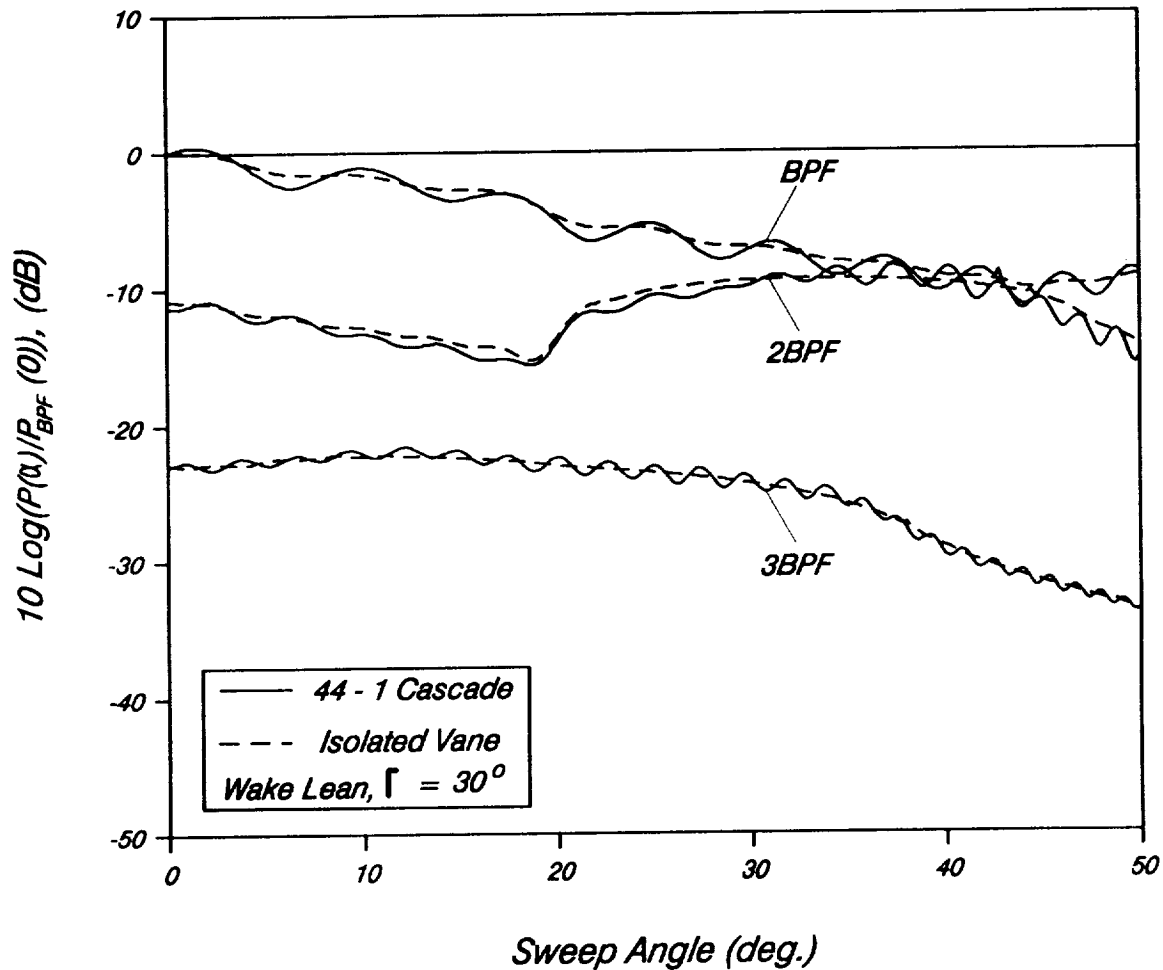
Fig. 4.5   Acoustic power generated by 44 - 1 cascade at the first three harmonics of BPF with a wake lean of Γ = 30 degrees. The acoustic power generated by an isolated airfoil is shown as a dashed line for comparison.

the wake orientation is such that moderate values of sweep actually reduce the phase variations along the vane leading edge (i.e., make the spanwise trace velocity supersonic). Thus, it is clear, once again, that the wake lean has a critical influence on the effectiveness of sweep as a means of noise reduction.

To emphasize this point, the acoustic power levels for a wake lean of -20 degrees are presented in Fig. (4.6). Here sweep produces noise reductions only for α larger than 35 degrees. In fact, for $0 \leq \alpha \leq 35$ degrees, the noise level shows a dramatic increase over the unswept case for each of the three harmonics displayed. It is only when large sweep angles are reached that the trace velocity along the leading edge becomes subsonic and substantial noise reductions occur. It is interesting to note that, in this case, negative vane sweep angles (root aft of tip) would produce substantial noise reductions.

Next, the results from the 22 - 14 case study are presented. As before, the decibel variations of the total acoustic power as a function of sweep for the first three harmonics of BPF noise are shown (see Figs. (4.7 - 4.11)). The general trends follow those illustrated in Figs. (4.2 - 4.6), but the pattern of oscillations is now more pronounced, since for this configuration the number of propagating modes is very small. There are, in fact, only two circumferential mode orders generated at BPF, i.e., $l = 8$ and -6 (in contrast, for 44 - 1 case there are over forty propagating circumferential modes at BPF). The hub-to-tip ratio is 0.5, leading to two cut-on radial modes for $l = 8$ mode and three cut-on radial modes for $l = -6$ mode. Here, the phase variations do not average out and thus, interference effects lead to larger amplitude oscillations.

The results for the 22 - 14 case with zero wake lean are shown in Fig. (4.7). Here, the noise level actually increases as sweep is introduced until sweep reaches about

117
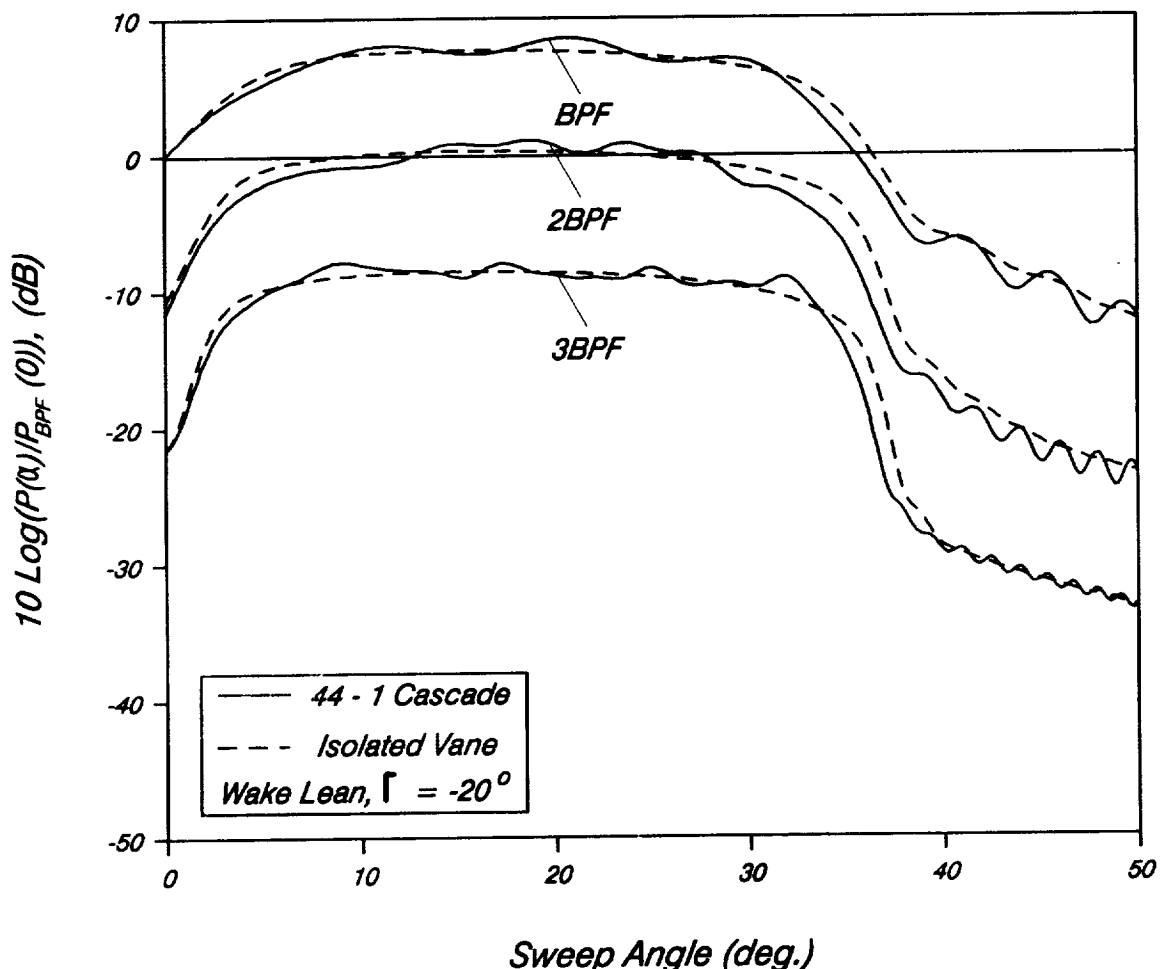
Fig. 4.6   Acoustic power generated by 44 - 1 cascade at the first three harmonics of BPF
with a wake lean of $\Gamma = -20$ degrees.   The acoustic power generated by an
isolated airfoil is shown as a dashed line for comparison.

118
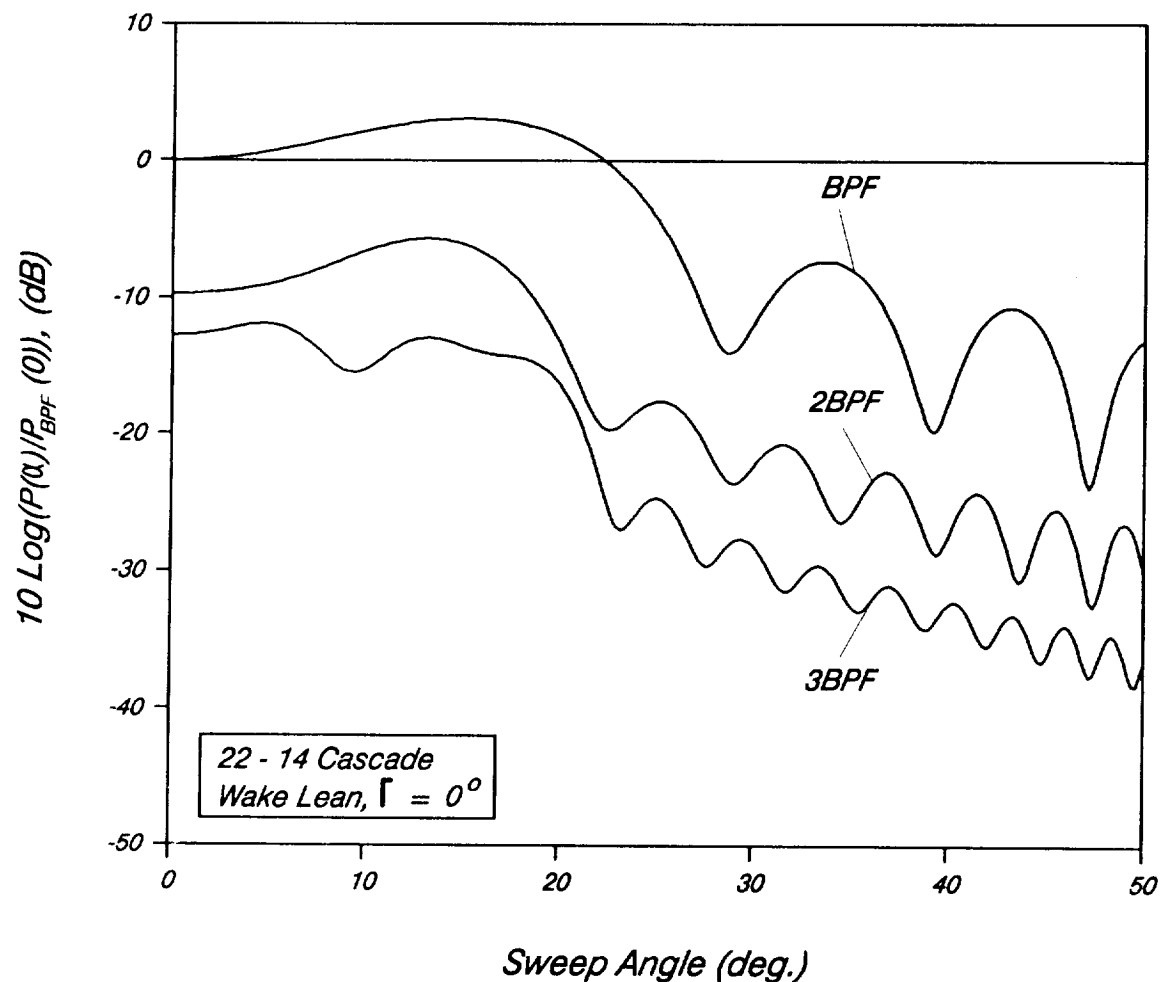
Fig. 4.7   Acoustic power generated by 22 - 14 cascade at the first three harmonics of
BPF with a wake lean of Γ = 0 degrees.

119
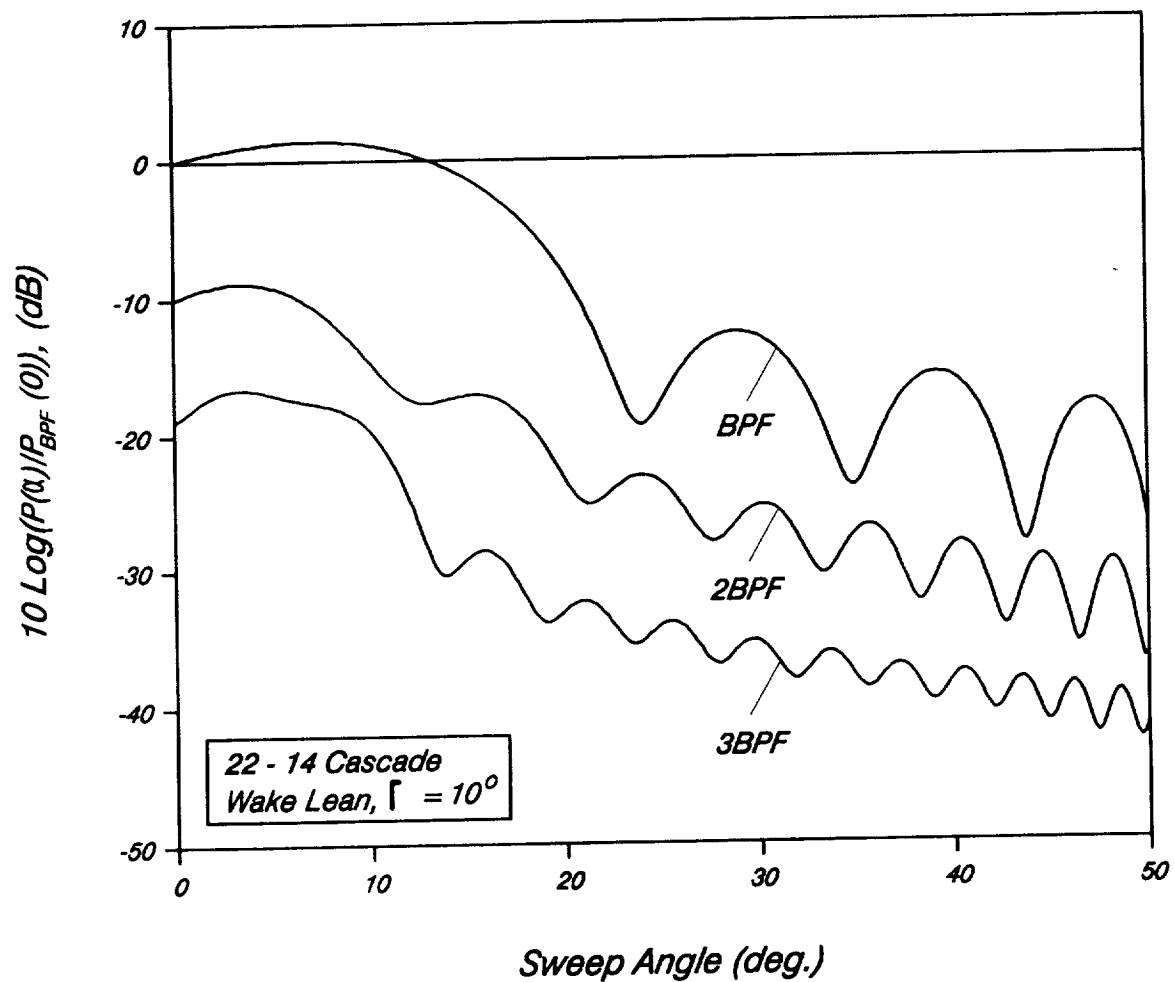
Fig. 4.8   Acoustic power generated by 22 - 14 cascade at the first three harmonics of BPF with a wake lean of Γ = 10 degrees.

120
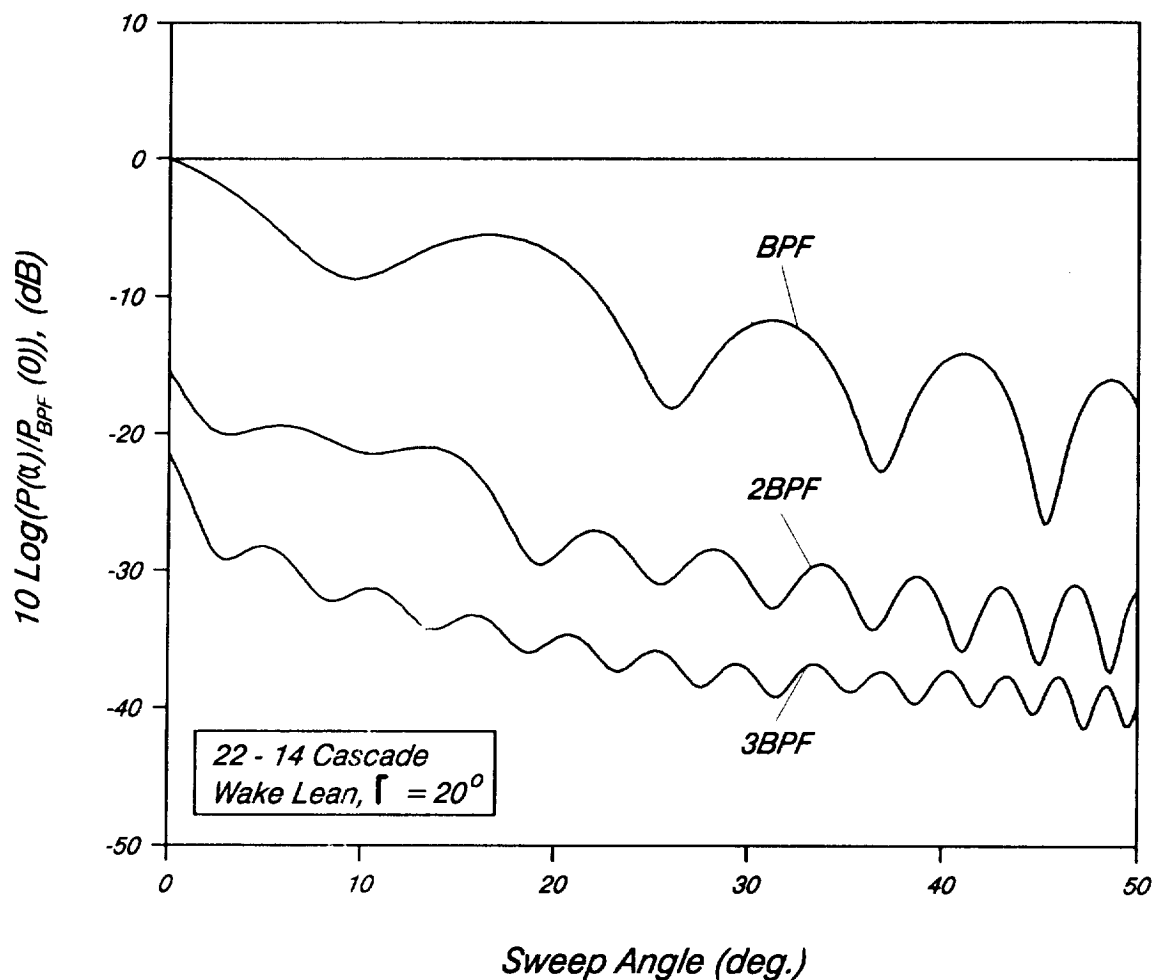
Fig. 4.9   Acoustic power generated by 22 - 14 cascade at the first three harmonics of BPF with a wake lean of Γ = 20 degrees.
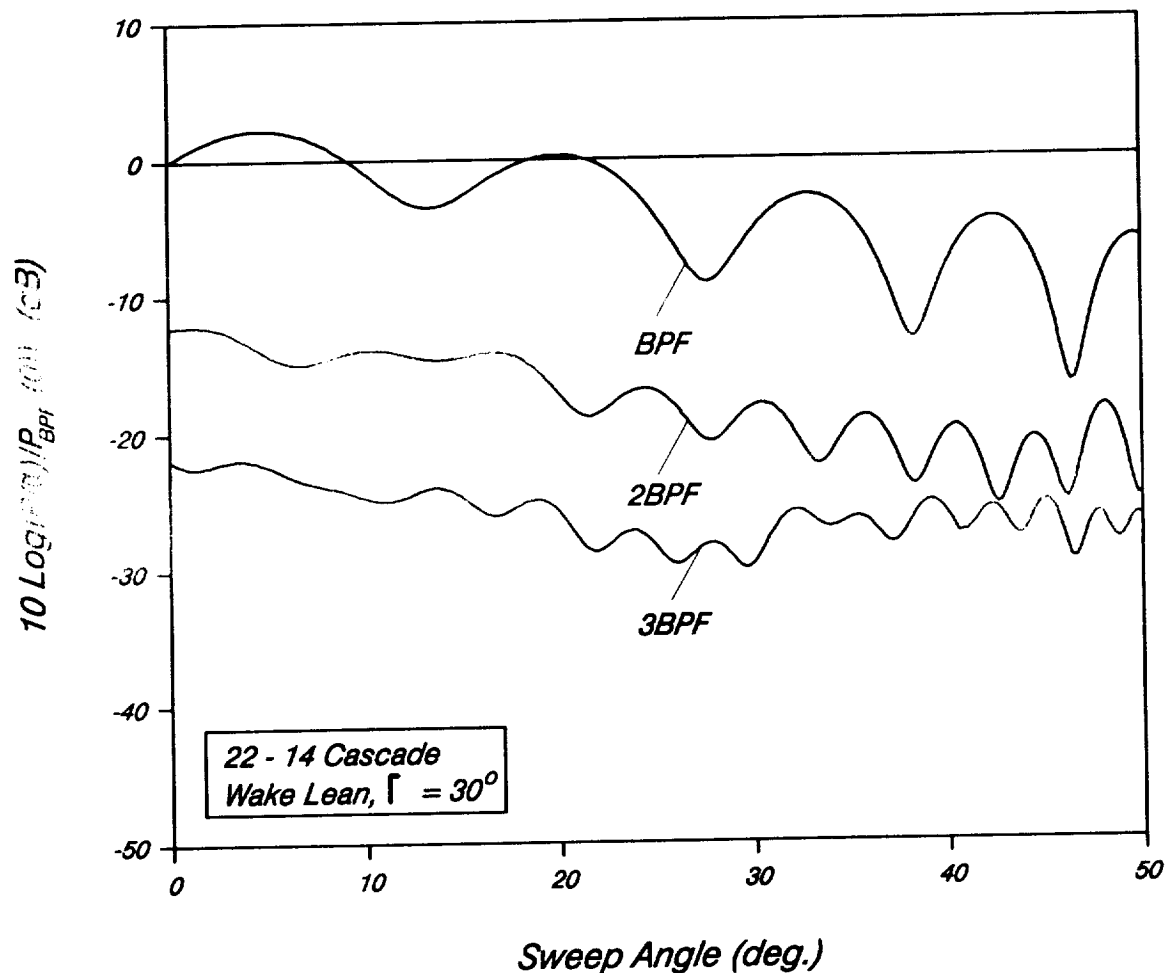
Fig. 4.10   Acoustic power generated by 22 - 14 cascade at the first three harmonics of
BPF with a wake lean of Γ = 30 degrees.
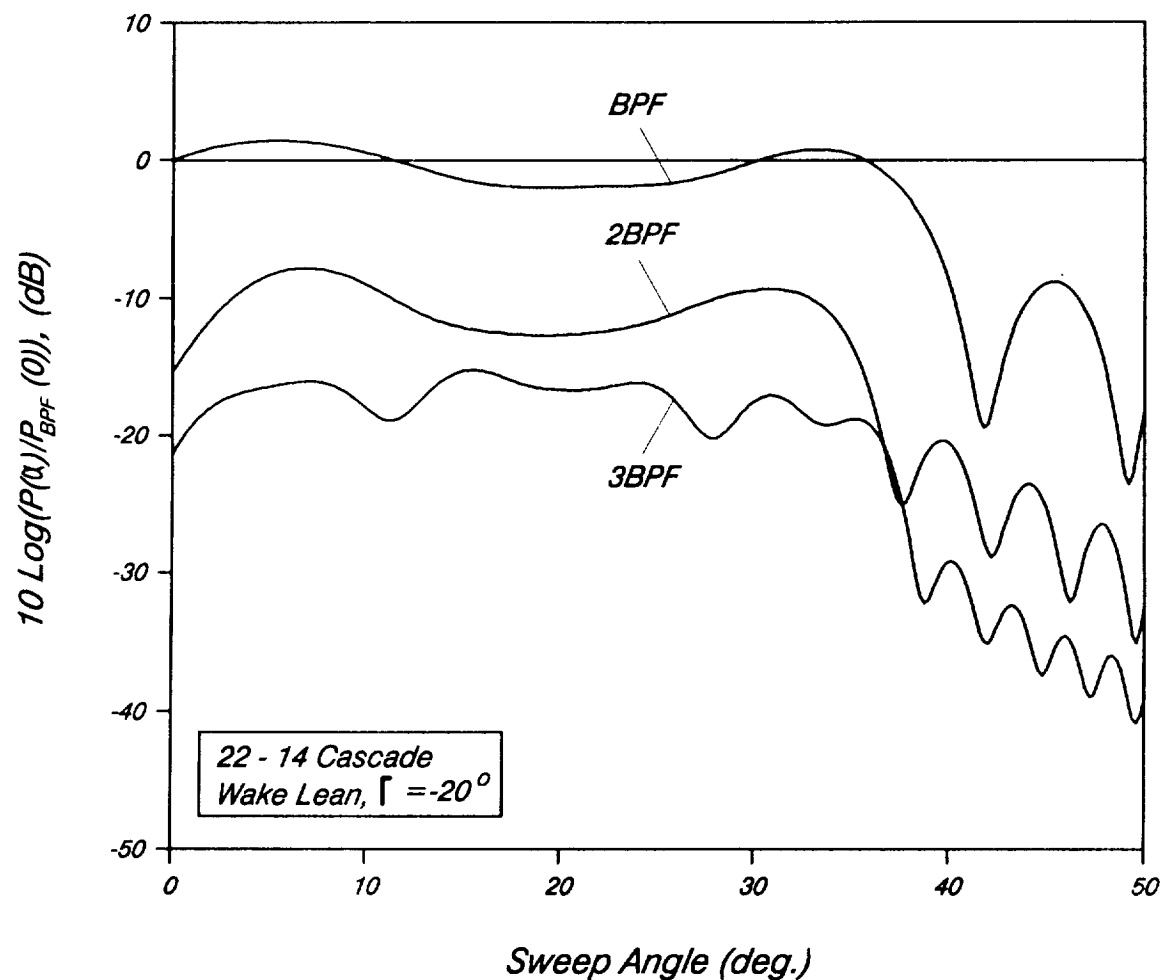
Fig. 4.11   Acoustic power generated by 22 - 14 cascade at the first three harmonics of BPF with a wake lean of Γ = -20 degrees.

20 degrees when fairly sizable reductions begin to occur in the levels of all three harmonics. As before, for moderate wake leans, i.e., 10 - 20 degrees, sweep is a particularly effective means of noise reduction (see Figs. (4.8 - 4.9)), while for larger wake leans, say, Γ = 30 degrees, it ceases to be very useful (see Fig. (4.10). For completeness, results for a wake lean of -20 degrees are displayed in Fig. (4.11).

The results from the two cascade studies (Figs. (4.2 - 4.11)), and indeed, the corresponding results from the isolated vane model, demonstrate that wake lean significantly affects the noise level, and hence it is of interest to examine the variations with respect to this parameter. In Fig. (4.12), the 22 - 14 case for zero vane sweep is considered. The first three harmonics of the BPF acoustic power are plotted as a function of rotor wake circumferential lean normalized by the power at BPF and Γ = 0 degrees. The acoustic power levels decrease rather slowly with increasing wake lean angle until lean angles greater than 20 degrees are reached. This behavior is consistent with the trace velocity arguments given before. It is interesting to note that the wake circumferential lean is produced by swirl velocities behind the rotor which deviate from a forced vortex design, and hence the wake circumferential lean is approximately a linear function of distance behind the rotor. Thus it seems likely that at least part of the experimentally observed noise reductions with spacing are due to wake lean rather than to the decay of the wake deficit velocity.

The sensitivity of the results to "radial" variations in the amplitude of the wake deficit velocity is also investigated. Such variations would arise from the radial distribution of fan loading, among other factors. For simplicity, linear variations with z were considered. Figure (4.13) represents typical results. The dashed curve corresponds to a

The y-axis is labeled $10 \, Log(P(\Gamma)/P_{BPF}(0))$, (dB) with values 10, 0, -10, -20, -30, -40, -50.

The x-axis is labeled *Wake Lean (deg.)* with values 0, 10, 20, 30, 40.

Curves labeled: *BPF*, *2BPF*, *3BPF*

Box label:
22 - 14 Cascade
Unswept Case, $\alpha = 0^{o}$
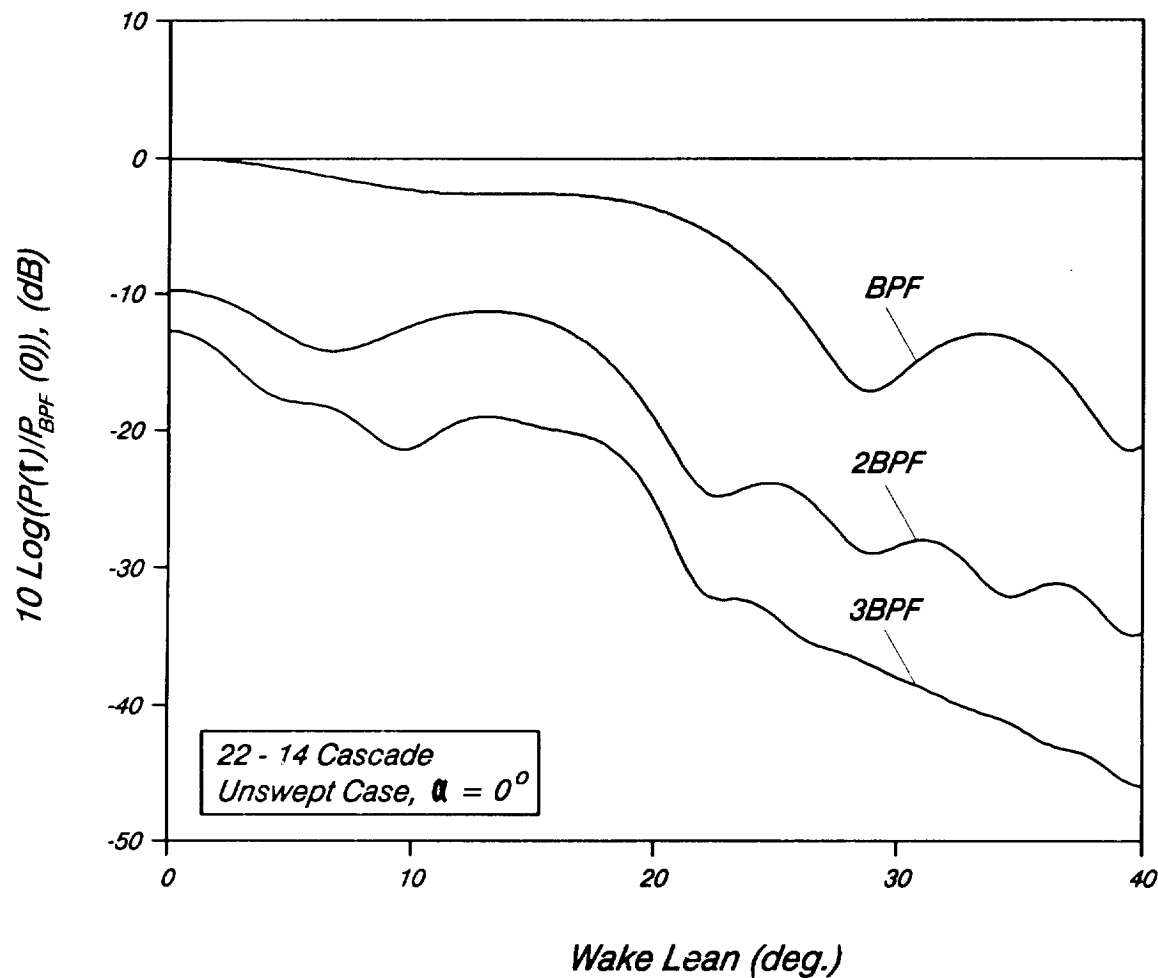
Fig. 4.12   Variation of acoustic power for the first three harmonics of BPF   for 22 - 14 cascade as a function of wake lean. The case for sweep angle $\alpha = 0$ degrees is presented.
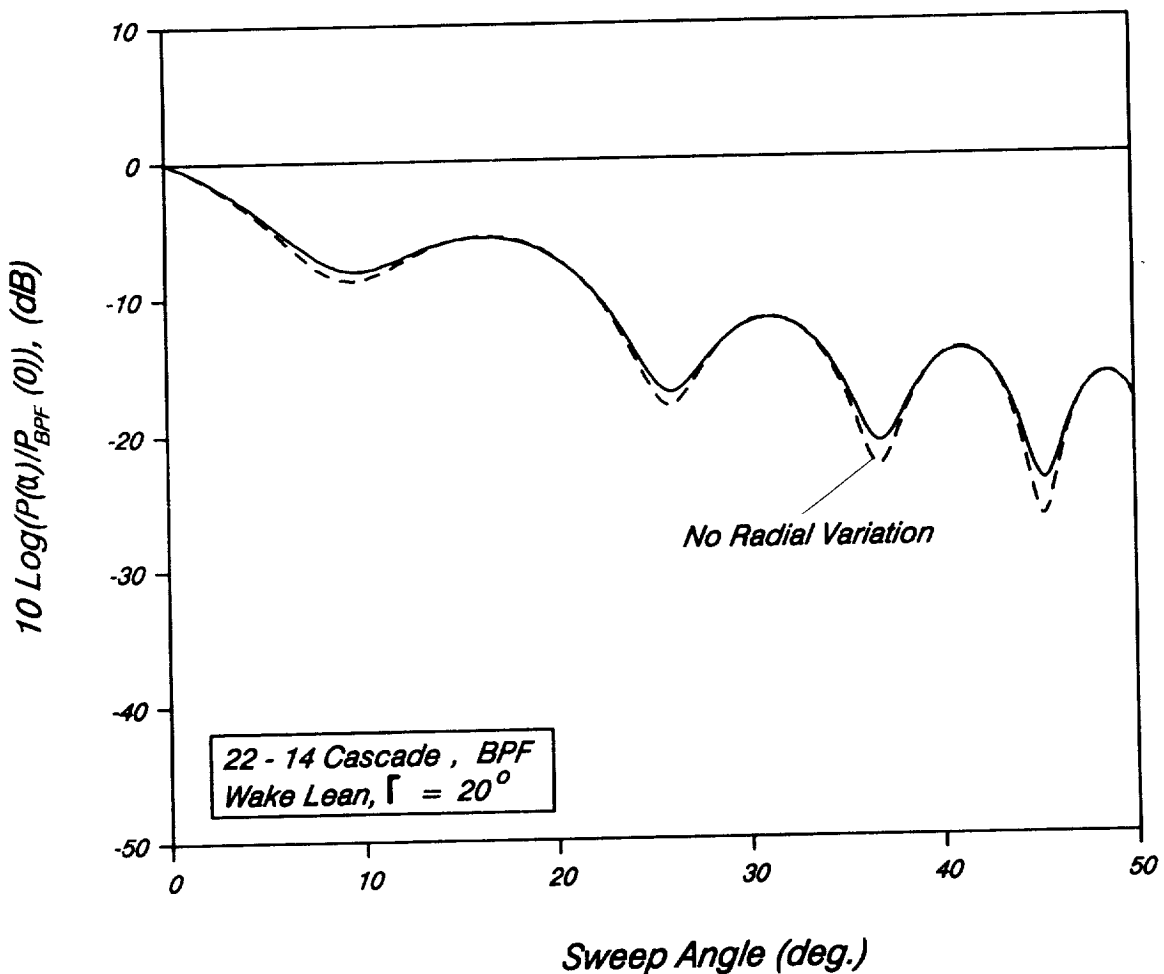
Fig. 4.13   Influence of radial variation in wake deficit velocity on BPF acoustic power for 22 - 14 cascade. No radial variation (dashed curve) and linear variation (solid curve) are plotted. The case for a wake lean of Γ = 20 degrees is presented.

wake deficit velocity that is independent of z, for which the result is identical to that in Fig. (4.9). The solid curve corresponds to the case of a hub deficit velocity that is twice the tip deficit velocity. The spanwise average deficit was the same in both cases. It is seen that the results are very similar, with the variation in deficit velocity only influencing the magnitude of the dips. The opposite case of a tip deficit twice that of the hub was also calculated and the results were virtually identical to the solid line in Fig. (4.13). Both curves were normalized by the same constant and thus, it is evident that the total power level is insensitive to the radial variations in deficit velocity.

An additional advantage of vane sweep, which was alluded to earlier, is that the sound field produced has a lower percentage of well cut-on modes. To illustrate this effect, in Fig. (4.14) the proportion of power in a given mode as a function of its cut-off ratio, ω_{cr}/ω is plotted. As before, ω_{cr} is the cut-off frequency of the mode in question. For zero vane sweep and zero lean, it is seen that only two of the five modes are strongly excited and both these modes are well cut-on When the sweep angle is increased to 20 degrees while holding the wake lean at $\Gamma = 0$, there is a dramatic shift towards modes much closer to cut-off. The introduction of wake lean also produces a shift towards cut-off, as can be seen from the other two cases in Fig. (4.14). As was indicated before, these shifts in the modal power distribution can be quite important, since acoustic duct liners generally produce more attenuation for modes close to cut-off.

In summary, a theoretical model for the interaction of rotor viscous wakes with a cascade of swept stator vanes is developed. Parametric calculations have been carried out to assess the influence of stator vane sweep on this noise source. The results indicate that, over a fairly wide range of conditions, sweep is beneficial in reducing noise levels. One
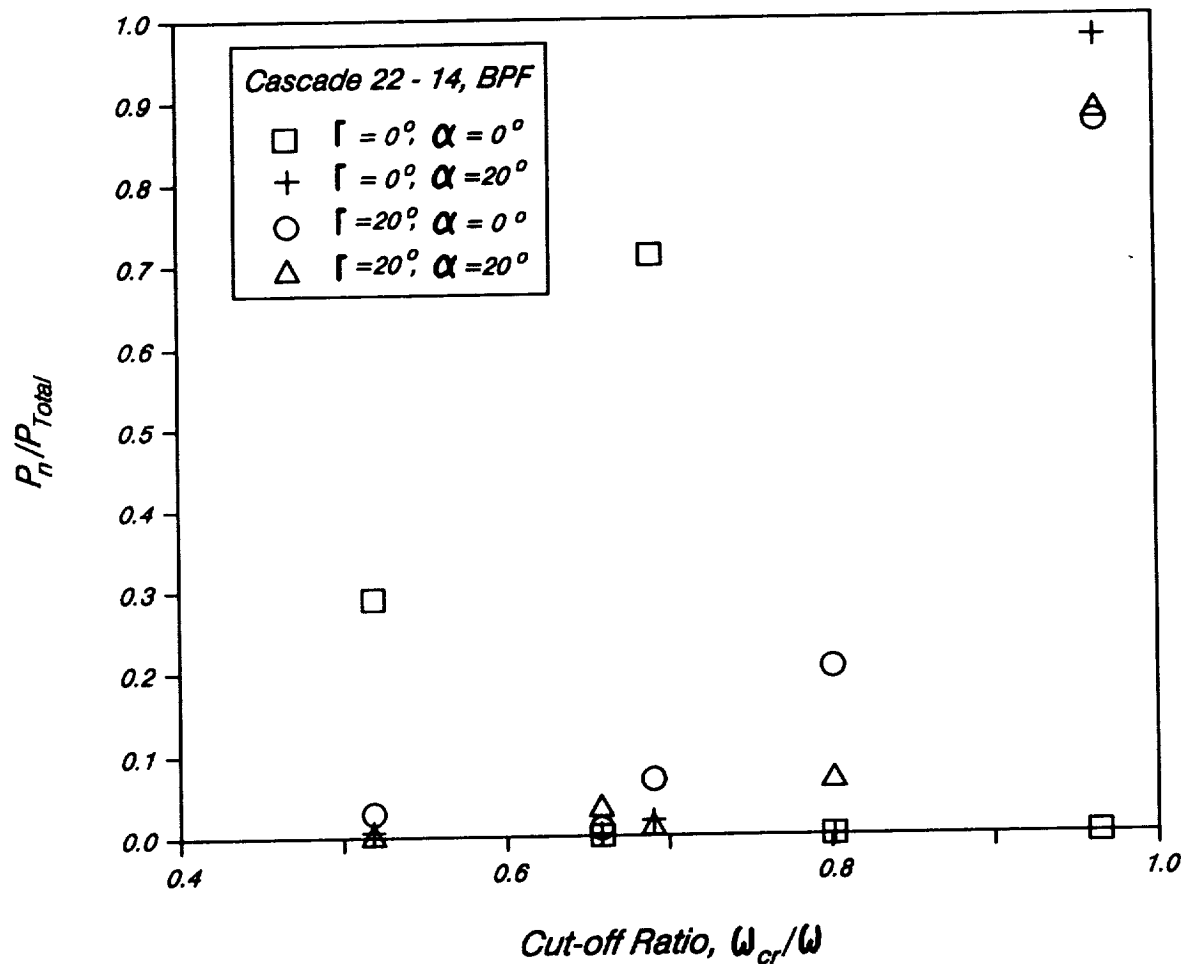
Fig. 4.14   Modal distribution of BPF acoustic power for 22 - 14 cascade as a function of cut-off ratio for different combinations of sweep and lean.

conclusion of particular importance is that wake circumferential lean substantially influences the results. The orientation of the vane sweep must be chosen judiciously to enhance the natural phase lags caused by wake lean, in which case rather small sweep angles can substantially reduce the noise level. It is found that the benefits of sweep are fairly insensitive to radial variations in the magnitude of the wake deficit.

CHAPTER 5

CONCLUSIONS AND RECOMMENDATIONS FOR FUTURE EXTENSIONS

In this chapter, the conclusions from this study and recommendations for future extensions of this work are summarized.

5.1 Summary of Important Conclusions

In this work, a theoretical model to quantify the influence of vane sweep on rotor-stator interaction noise is developed. The analysis is based on a direct formulation of the problem instead of the classical separation into aerodynamic and acoustic parts. In a mathematical approach, the rotor-stator interaction is modeled by a convected velocity disturbance (i.e., a gust), representing the rotor viscous wake, encountering a cascade of finite span swept airfoils, representing the row of swept stator vanes. The interaction of the convected gust with the airfoil cascade results in generation of an acoustic disturbance. The small-amplitude character of the disturbances allows a linearization of the equations of motion which, after some manipulation, lead to a convected wave equation for the velocity potential of the acoustic disturbance. This formulation is presented in Chapter 2.

In Chapter 3, the kernel problem of a single finite span swept airfoil interacting with a convected gust is analyzed. Taking advantage of the high-frequency character of the gusts of practical interest, an approximate solution to the kernel problem is obtained by ignoring the small contribution of the trailing edge to the noise field. It is shown that the farfield character of the single vane solution is strongly influenced by leading edge sweep. A detailed parametric study of the single vane solution is then carried out. The results indicate that airfoil sweep is indeed beneficial in reducing the noise levels generated by gust-airfoil interaction. However, the most important conclusion from that parametric

study is that the effectiveness of sweep is greatly influenced by the rotor wake twist or circumferential lean.

Utilizing the kernel solution for a single vane, an approximate high-frequency cascade model is developed in Chapter 4. In developing the approximate cascade solution, advantage has been taken of the weak coupling between adjacent leading edges in much the same way that the leading- and trailing-edge decoupling is utilized in the single airfoil case. Considering only the upstream radiated noise, the farfields from an infinite number of airfoils is summed to obtain the approximate cascade solution. The resulting infinite summation is then manipulated into the form of a finite sum of propagating circumferential modes.

The approximate cascade model is used to assess and quantify the effectiveness of vane sweep in reducing rotor-stator interaction noise. As far as the effectiveness of sweep and the influence of wake lean on it are concerned, the results from the cascade parametric calculations essentially confirm the single vane results and conclusions. An additional advantage of vane sweep which is identified in the single vane model, and verified in the cascade simulations, is that the sound field generated by a swept cascade has a lower percentage of well cut-on modes. In other words, sweep shifts the modal power distribution towards the modes near cut-off. This is an important effect, since acoustic duct liners are most efficient in attenuating modes near cut-off. Hence, the use of acoustic duct liners in conjunction with vane sweep could prove quite beneficial in reducing rotor-stator interaction noise. Finally, it is shown that the radial variations of the rotor wake centerline deficit velocity have little influence on the efficiency of vane sweep as a mechanism for reducing rotor-stator interaction noise.

5.2 Recommendations for Future Extensions

Regarding the continuation of this investigation, there are several important issues which should be addressed. Four such issues which deserve attention are briefly discussed below. They are presented in an order which reflects the amount of work required to analyze each one.

An interesting question to answer is how efficient the vane sweep is in reducing rotor-stator interaction noise compared with other methods. In particular, a comparison with the Tyler and Sofrin (1961) cut-off involving an appropriate choice of blade/vane count ratio should be very interesting. There are relative advantages to both approaches. The Tyler-Sofrin cut-off is complete, but in practice is limited to the blade-passing frequency (BPF). The cut-off effect due to sweep, while not complete, applies equally to all harmonics of BPF. Results from such a comparison would be of a great deal of interest to aircraft engine manufacturers.

An extension of the current theory which would improve its utility as a design tool is the inclusion, in the rotor gust model, of tip vortices from the fan blades. This can be done by modeling the rotor blade tip vortices by a row of isolated potential vortices with an appropriate spacing. Then, using an eigenfunction expansion of this representation in the "radial" coordinate, one can account for the effect of the tip vortices in terms of an equivalent infinite sum of the convected gusts used in the present analysis.

As was mentioned earlier, an important influence of vane sweep is to shift the modal power distribution towards the modes near cut-off where acoustic duct liners are most efficient in absorbing sound. Hence, a logical extension of the current theory is to account for the presence of acoustically compliant walls in this model. This can be done by introducing an acoustic-impedance (which is a measure of the sound-reflecting

132

properties of the wall) for the channel walls. Mathematically, the inclusion of the compliant walls requires a straightforward modification of the eigenfunction expansion in the radial coordinate. The resulting model could be used in a parametric study to find the best sweep/impedance combination for a given set of gust parameters.

Finally, in order to have a complete rotor-stator noise model, the current theory should be extended to include the downstream radiated noise. This extension requires a substantial effort whose main elements are outlined below. Consider the reflected rays (see Fig. 4.1) inside the rectangular ducts formed by the adjacent airfoils and channel walls. For each such duct, the no-flow condition through the channel walls is already satisfied by the leading edge solution. For the walls formed by the adjacent airfoils, the no-flow condition can be satisfied by a superposition of an infinite set of images as shown in Fig. (5.1). The two resulting infinite sums can be manipulated into an expression involving only a finite number propagating acoustic modes for each duct.

Next, the condition of continuity of pressure across the wake sheets (i.e., shed vorticity sheets) extending from the two adjacent trailing edges must be enforced. This can be accomplished as follows. Each trailing edge problem can be considered as a semi-infinite chord problem in which the airfoil chord extends to the upstream infinity. The solution to that problem must cancel the pressure jump of the duct solution across the wake sheet. The procedure to find such a solution follows the same general approach utilized in Chapter 3. Here, however, the leading-edge correction is neglected. Then, the two trailing-edge solutions are combined with an infinite image system to satisfy the no-flow condition through the channel walls.

Finally, a solution which satisfies both the no-flow condition inside the duct and the continuity-of-pressure condition across the two trailing-edge wake sheets can be

133

Images

Trailing Edge   Wake Sheet

Duct Walls   Direct Ray

Duct Modes   Diffracted Ray

Leading Edge
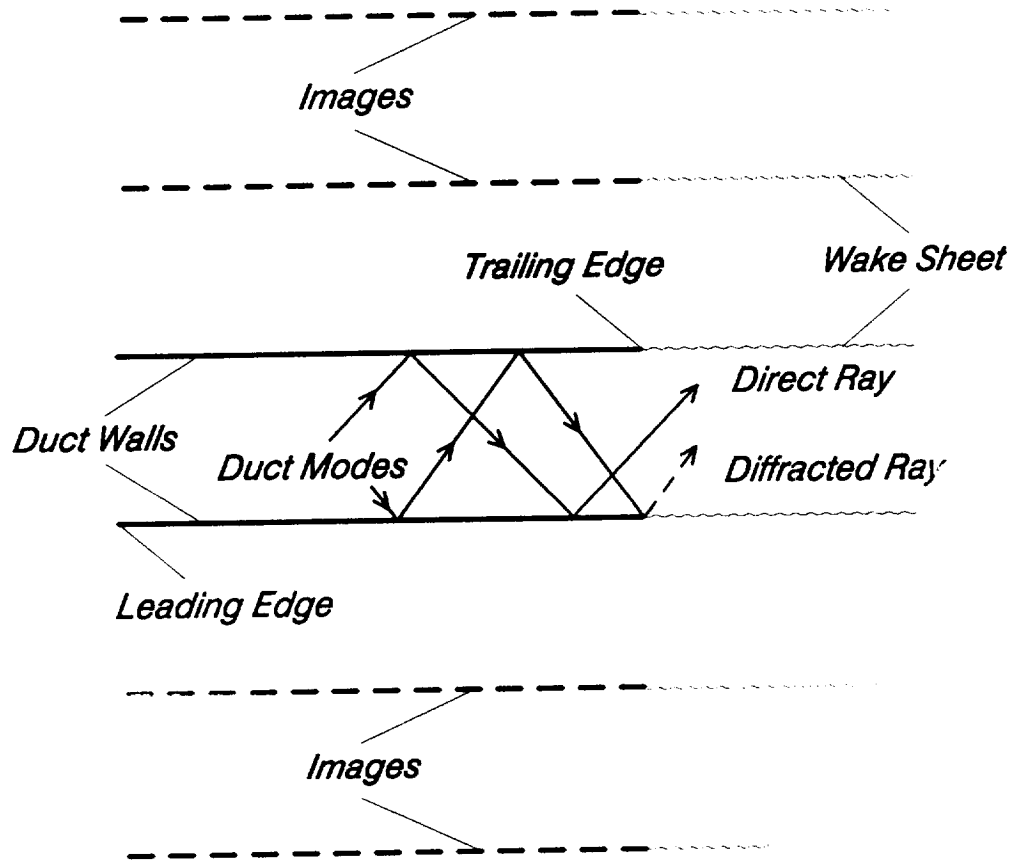
Images

Fig. 5.1   Image system for the duct and downstream radiated noise problems.

134

obtained by adding the duct and trailing-edge solutions together. At the exit of each duct, the acoustic rays either propagate directly to the downstream farfield or are diffracted by the trailing edges. The diffracted field can be ignored since it is $O(k_{\bar{x}}^{1/2})$ weaker in comparison with direct field. Hence, an approximate high-frequency solution to the problem of downstream radiated cascade noise can be computed by adding the contributions from all the ducts in a manner similar to that described for the upstream radiated noise in Chapter 4.

ACKNOWLEDGEMENT

APPENDIX A

LEADING-EDGE BEHAVIOR

The appropriate behavior of $h_m(\xi,0,\varsigma)$ for small ξ is that of a three-dimensional, irrotational, and incompressible flow around the leading edge. Essentially, the effects of compressibility are negligible on the scale of very small distances from the leading edge. In mathematical terms, near the leading edge the equation governing the modified acoustic velocity potential reduces to the three-dimensional Laplace's equation. The behavior of $h_m(\xi,0,\varsigma)$ for small ξ can then be inferred from the solution to that equation. An exact analytical solution of the three-dimensional Laplace's equation for the current geometry is, at best, extremely difficult to obtain. However, the local behavior of $h_m(\xi,0,\varsigma)$ near the leading edge can be discerned using a heuristic argument which follows.

First consider the central portion of the airfoil span. Here, as the leading edge is approached, the ξ and y derivatives become large compared with the ς derivative and the flow behaves essentially two-dimensionally. A simple conformal mapping then shows that the velocitiy potential must behave as $h_m(\xi,0,\varsigma) = O(\xi^{1/2})$ as $\xi \to 0^+$. This result applies as the leading edge is approached ($\xi \to 0^+$) for fixed ς, where $\varsigma \neq 0, 1$.

Next, consider the behavior of $h_m(\xi,0,\varsigma)$ as the junction between the airfoil leading edge and the end wall is approached. Near the lower wall, it is required that ξ and ς to approach zero at the same rate while near the upper wall, ξ and $(1 - \varsigma)$ are required to approach zero at the same rate. Here, the flow is clearly three-dimensional. The behavior of $h_m(\xi,0,\varsigma)$ as ξ and ς, or $1 - \varsigma$, approach zero can be found by determining a local solution to the three-dimensional Laplace's equation.

136

Such a solution was obtained by Noble (1959) using an elegant approximation in the context of diffraction theory. His results, interpreted in the current variables, show that $h_m(\xi,0,\varsigma) = O(\xi^\mu)$ where μ depends on the corner angle v. The corner angle v is $\pi/2 - \alpha$ for the lower corner and $\pi/2 + \alpha$ for the upper corner (see Fig. (A.1)). Figure (A.2) is a plot of μ versus the corner angle v computed using Noble's (1959) results. For a swept vane, the value of μ corresponding to the lower corner is less than $1/2$ while the vales of μ corresponding to the upper corner is greater than $1/2$. An example for the case of $\alpha = 40$ degrees is shown. For this value of α, μ corresponding to the lower corner (i.e., $v = 50$ degrees) and that corresponding to the upper corner (i.e., $v = 130$ degrees) are shown. For comparison, μ corresponding to the case of no-sweep (i.e., $\alpha = 0$ degrees, $v = 90$ degrees) is also shown.

Qualitatively, it is useful to consider $h_m(\xi,0,\varsigma)$ as $O(\xi^{\mu(\varsigma)})$ where $\mu(\varsigma)$ is a function that varies smoothly from the corner values to the value $\mu = 1/2$ appropriate to the central portion of the span. The "boundary layers" near $\varsigma = 0$ and 1 are of $O(\xi)$ thickness, and hence quite thin for small values of ξ.

A similar discussion is possible for the behavior of the derivative $\partial h_m(\xi,0,\varsigma)/\partial y$ as $\xi \rightarrow 0^-$. Combining these results, edge conditions of the form

$$h_m(\xi,0,\varsigma) \propto \xi^{\mu(\varsigma)} F(\varsigma) \qquad as \qquad \xi \rightarrow 0^+ \qquad\qquad (A.1a)$$

and

$$\frac{\partial}{\partial y}h_m(\xi,0,\varsigma) \propto \xi^{\mu(\varsigma)-1} G(\varsigma) \qquad as \qquad \xi \rightarrow 0^- \qquad\qquad (A.1b)$$

are postulated where the $F(\varsigma)$ and $G(\varsigma)$ are smooth functions. For the special case of an infinite span airfoil interacting with a gust which has harmonic spanwise dependence, $F(\varsigma)$

137
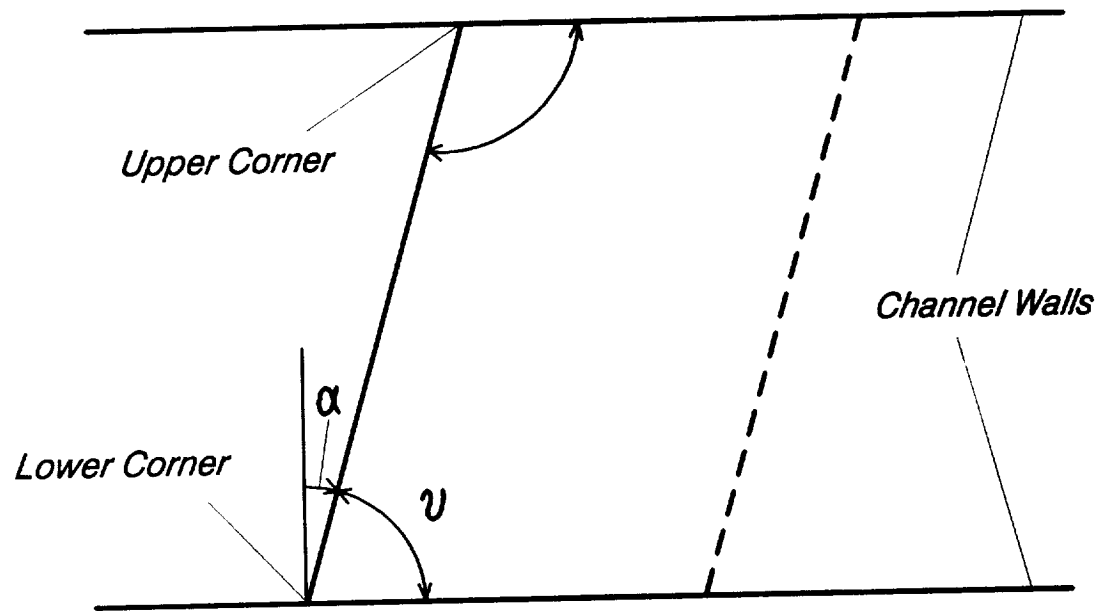
Fig. A.1   Sweep angle α and corner angle v.
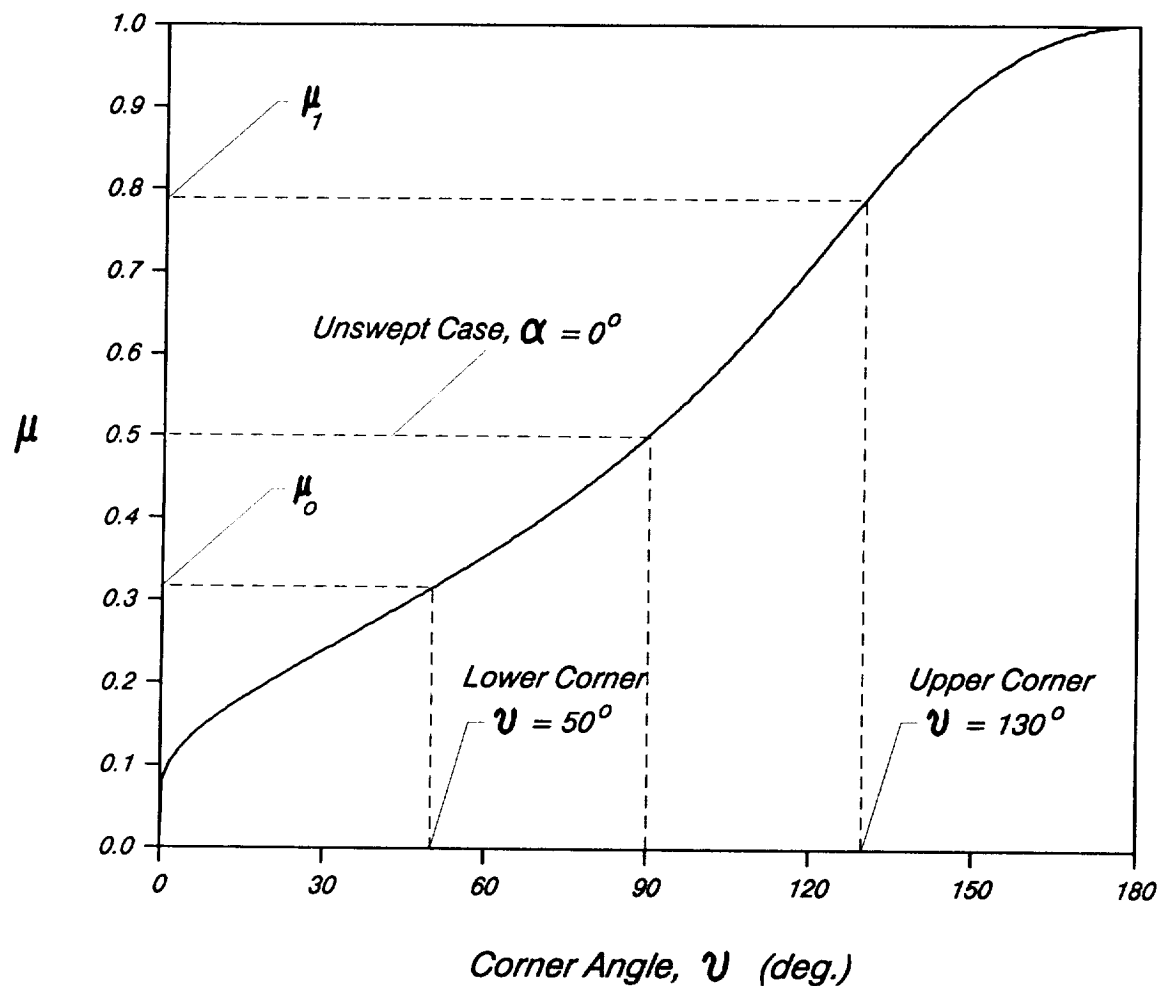
Fig. A.2   Variation of exponent μ as a function of corner angle v. The case for $v = 50$
degrees is shown.

and $G(\zeta)$ are also harmonic with the same dependence as that of the gust. This is a consequence of the symmetry present in this case which allows the ζ-dependence to be factored out of the problem (i.e., out of the differential equation and boundary conditions) altogether. For the current geometry, the presence of the end walls destroys the symmetry mentioned above and therefore the ζ-dependence cannot be factored out. However, it is the exponent $\mu(\zeta)$, rather than the coefficients $F(\zeta)$ and $G(\zeta)$, which is crucial in the application of the Wiener-Hopf technique.

APPENDIX B

SOLUTION OF THE WIENER-HOPF EQUATION (3.10)

In this appendix, details of the Wiener-Hopf solution to Eq. (3.10) of Section 3.1 are presented. The solution contains an infinite number of unknown constants.

Recall that Eq. (3.10) is given by

$$-\sqrt{1 - \gamma^2} \; \sqrt{\lambda + W_n} \; C_n^+(\lambda) = \frac{D_n^-(\lambda)}{\sqrt{\lambda - W_n}}$$

$$- \frac{\epsilon_n \, b_0}{(2\pi)^{1/2} \, \gamma} \; \frac{E_n(\lambda)}{\sqrt{\lambda - W_n} \; (\lambda + \kappa)} \qquad\qquad \text{(B.1a)}$$

where

$$E_n(\lambda) = \frac{(\lambda + \kappa) \, [(-1)^n \, e^{i\gamma(\lambda + \kappa)} - 1]}{(\lambda + \kappa - n\pi/\gamma) \, (\lambda + \kappa + n\pi/\gamma)} . \qquad\qquad \text{(B.1b)}$$

Crude estimates of the behavior at infinity of $C_n^+(\lambda)$ and $D_n^-(\lambda)$ were shown to be

$$C_n^+(\lambda) \propto \lambda^{-2-\mu(0)} \, F(0), \qquad D_n^-(\lambda) \propto \lambda^{-1-\mu(1)} \, e^{i\gamma\lambda} \, G(1) \qquad\qquad \text{(B.2)}$$

as $|\lambda| \to \infty$ in upper and lower half-planes, respectively. Recall that $\mu(0)$ and $\mu(1)$ satisfy the relation $0 < \mu(0) \le 1/2 \le \mu(1) < 1$. Upon solving Eq. (B.1a), the asymptotic estimates given by Eq. (B.2) will be re-examined.

The difficulty due to exponential behavior at infinity of the functions in Eq. (B.1a) can be avoided by dividing both sides of that equation by an appropriate divisor function such that the resulting equation exhibits algebraic behavior at infinity. The solution to Eq. (B.1a) is developed using three different choices of divisor function.

141

B.1 First Choice:

Consider the function

$$Q_1(\lambda) = [(-1)^n\, e^{i\gamma(\lambda + \kappa)} - 1] \ . \tag{B.3}$$

Note that $Q_1(\lambda)$ decays algebraically in the upper half-plane but grows exponentially in the lower half-plane. $Q_1(\lambda)$ also has an infinite number of zeros in the lower half-plane at $\lambda = -\kappa + n\pi/\gamma$ since κ is assumed to have a small positive imaginary part. Upon dividing both sides of Eq. (B.1a) by the divisor function, one obtains

$$- \frac{\sqrt{1 - \gamma^2}\ \sqrt{\lambda + W_n}\ C_n^+(\lambda)}{[(-1)^n\, e^{i\gamma(\lambda + \kappa)} - 1]} = \frac{D_n^-(\lambda)}{\sqrt{\lambda - W_n}\ [(-1)^n\, e^{i\gamma(\lambda + \kappa)} - 1]}$$

$$- \frac{\epsilon_n\, b_0}{(2\pi)^{1/2}\, \gamma}\ \frac{1}{\sqrt{\lambda - W_n}\ (\lambda + \kappa - n\pi/\gamma)\ (\lambda + \kappa + n\pi/\gamma)} \ . \tag{B.4}$$

The term on the left hand side is still a plus function. However, the first term on the right hand side is now a mixed function due to the zeros of $Q_1(\lambda)$. The last term remains a mixed function. The mixed functions can be split additively as follows:

$$\frac{D_n^-(\lambda)}{\sqrt{\lambda - W_n}\ [(-1)^n\, e^{i\gamma(\lambda + \kappa)} - 1]} = U_n^+(\lambda) + U_n^-(\lambda) \ , \tag{B.5a}$$

$$\frac{\epsilon_n\, b_0}{(2\pi)^{1/2}\, \gamma}\ \frac{1}{\sqrt{\lambda - W_n}\ (\lambda + \kappa - n\pi/\gamma)\ (\lambda + \kappa + n\pi/\gamma)} = S_n^+(\lambda) + S_n^-(\lambda) \ . \tag{B.5b}$$

The functions $U_n^-(\lambda)$ and $S_n^-(\lambda)$ can be found via the Cauchy integral formula, or alternatively, the poles in the lower half-plane can be simply subtracted. Thus,

$$- \frac{\sqrt{1 - \gamma^2} \; \sqrt{\lambda + W_n} \; C_n^+(\lambda)}{[(-1)^n \; e^{i\gamma(\lambda + \kappa)} - 1]} - U_n^+(\lambda) + S_n^+(\lambda) = U_n^-(\lambda) - S_n^-(\lambda) \qquad \text{(B.6a)}$$

where

$$U_n^+(\lambda) = - i\gamma^{-1} \sum_{j=-\infty}^{+\infty} \frac{D_n^-(\lambda_j)}{\sqrt{\lambda_j - W_n} \; (\lambda - \lambda_j)}, \qquad \text{(B.6b)}$$

$$U_n^-(\lambda) = \frac{D_n^-(\lambda)}{\sqrt{\lambda - W_n} \; [(-1)^n \; e^{i\gamma(\lambda + \kappa)} - 1]} - U_n^+(\lambda), \qquad \text{(B.6c)}$$

$$S_n^+(\lambda) = \frac{i \epsilon_n \; b_0}{(2\pi)^{3/2} \; n}$$

$$x \left[\frac{1}{\sqrt{\kappa + W_n - n\pi/\gamma} \; (\lambda + \kappa - n\pi/\gamma)} - \frac{1}{\sqrt{\kappa + W_n + n\pi/\gamma} \; (\lambda + \kappa + n\pi/\gamma)} \right] \qquad \text{(B.6d)}$$

$$S_n^-(\lambda) = \frac{\epsilon_n \; b_0}{(2\pi)^{1/2} \; \gamma} \; \frac{1}{\sqrt{\lambda - W_n} \; (\lambda + \kappa - n\pi/\gamma)(\lambda + \kappa + n\pi/\gamma)} - S_n^+(\lambda) \qquad \text{(B.6e)}$$

where $\lambda_j = - \kappa + (2j - n)\pi/\gamma$ are the poles of function on the left hand side of Eq. (B.5a). $D_n^-(\lambda_j)$ are unknown constants representing the values of $D_n^-(\lambda)$ at points λ_j. The left-hand-side of the Eq. (B.6a) is analytic in the upper half while the right-hand-side is analytic in the lower half of the complex λ-plane. Thus, Eq. (B.6a) defines an entire function $J(\lambda)$. Upon examining the edge conditions given by Eq. (B.2), it can be seen that both sides of the equation approach zero as $|\lambda| \to \infty$ in the respective half-planes. Hence, according to the Liouville's theorem $J(\lambda)$ is identically zero. Then, each side of Eq. (B.6a) can be solved separately for the unknown functions $C_n^+(\lambda)$ and $D_n^-(\lambda)$. The result is

143

$$C_n^+(\lambda) = i \; \frac{[(-1)^n \; e^{i\gamma(\lambda + \kappa)} - 1]}{\sqrt{1 - \gamma^2} \; \sqrt{\lambda + W_n}}$$

$$\times \left\{ \gamma^{-1} \sum_{j=-\infty}^{+\infty} \frac{D_n^-(\lambda_j)}{\sqrt{\lambda_j - W_n} \; (\lambda - \lambda_j)} + \frac{\epsilon_n \; b_0}{(2\pi)^{3/2} \; n} \right.$$

$$\times \left. \left[\frac{1}{\sqrt{\kappa + W_n - n\pi/\gamma} \; (\lambda + \kappa - n\pi/\gamma)} - \frac{1}{\sqrt{\kappa + W_n + n\pi/\gamma} \; (\lambda + \kappa + n\pi/\gamma)} \right] \right\} \qquad \text{(B.7a)}$$

and

$$D_n^-(\lambda) = - \sqrt{\lambda - W_n} \; [(-1)^n \; e^{i\gamma(\lambda + \kappa)} - 1]$$

$$\times \left\{ i \, \gamma^{-1} \sum_{j=-\infty}^{+\infty} \frac{D_n^-(\lambda_j)}{\sqrt{\lambda_j - W_n} \; (\lambda - \lambda_j)} \right.$$

$$- \frac{\epsilon_n \; b_0}{(2\pi)^{1/2} \; \gamma} \; \frac{1}{\sqrt{\lambda - W_n} \; (\lambda + \kappa - n\pi/\gamma) \; (\lambda + \kappa + n\pi/\gamma)} + \frac{i \, \epsilon_n \; b_0}{(2\pi)^{3/2} \; n}$$

$$\times \left. \left[\frac{1}{\sqrt{\kappa + W_n - n\pi/\gamma} \; (\lambda + \kappa - n\pi/\gamma)} - \frac{1}{\sqrt{\kappa + W_n + n\pi/\gamma} \; (\lambda + \kappa + n\pi/\gamma)} \right] \right\} . \qquad \text{(B.7b)}$$

These expressions involve an infinite number of unknown constants which must be

determined in order to have an explicit representation for $C_n^+(\lambda)$ and $D_n^-(\lambda)$. The problem of determining these unknown constants and the difficulties involved are discussed in Section 3.1.

It is interesting to re-examine the edge conditions in the light of Eqs. (B.7). According to these equations, the asymptotic behavior of $C_n^+(\lambda)$ and $D_n^-(\lambda)$ are given by

$$C_n^+(\lambda) \propto \lambda^{-3/2} , \qquad D_n^-(\lambda) \propto \lambda^{-1/2} e^{i\gamma\lambda} \tag{B.8}$$

as $|\lambda| \rightarrow \infty$ in the upper and lower lower half-planes, respectively. Therefore, the crude estimates given by Eq. (B.2) while providing the correct trends i.e., the algebraic decay of $C_n^+(\lambda)$ and exponential growth of $D_n^-(\lambda)$, are quantitatively inaccurate.

B.2 Second Choice:

Next, upon dividing Eq. (B.1a) by the function

$$Q_2(\lambda) = \frac{[(-1)^n e^{i\gamma(\lambda + \kappa)} - 1]}{(\lambda + \kappa + n\pi/\gamma)} , \tag{B.9}$$

one obtains

$$- \frac{\sqrt{1 - \gamma^2} \sqrt{\lambda + W_n} (\lambda + \kappa + n\pi/\gamma) C_n^+(\lambda)}{[(-1)^n e^{i\gamma(\lambda + \kappa)} - 1]}$$

$$= \frac{(\lambda + \kappa + n\pi/\gamma) D_n^-(\lambda)}{\sqrt{\lambda - W_n} [(-1)^n e^{i\gamma(\lambda + \kappa)} - 1]} - \frac{\epsilon_n b_0}{(2\pi)^{1/2} \gamma} \frac{1}{\sqrt{\lambda - W_n} (\lambda + \kappa - n\pi/\gamma)} .$$

$$\tag{B.10}$$

Note that, the term on the left hand side is a plus function while the terms on the right hand side are both mixed. Upon splitting the mixed terms and rearranging the resulting

equation, one finds

$$- \frac{\sqrt{1 - \gamma^2} \sqrt{\lambda + W_n} \, (\lambda + \kappa + n\pi/\gamma) \, C_{\overline{n}}^{+}(\lambda)}{[(-1)^n \, e^{i\gamma(\lambda + \kappa)} - 1]} - V_{\overline{n}}^{+}(\lambda) + T_{\overline{n}}^{+}(\lambda) = V_{\overline{n}}^{-}(\lambda) - T_{\overline{n}}^{-}(\lambda)$$

(B.11a)

where

$$V_{\overline{n}}^{+}(\lambda) = -2\pi i \gamma^{-2} \sum_{j=-\infty}^{+\infty}{}' \frac{j \, D_{\overline{n}}^{-}(\lambda_j)}{\sqrt{\lambda_j - W_n} \, (\lambda - \lambda_j)},$$

(B.11b)

$$V_{\overline{n}}^{-}(\lambda) = \frac{(\lambda + \kappa + n\pi/\gamma) \, D_{\overline{n}}^{-}(\lambda)}{\sqrt{\lambda - W_n} \, [(-1)^n \, e^{i\gamma(\lambda + \kappa)} - 1]} - V_{\overline{n}}^{+}(\lambda),$$

(B.11c)

$$T_{\overline{n}}^{+}(\lambda) = \frac{i \, \epsilon_n \, b_0}{(2\pi)^{1/2} \, \gamma} \frac{1}{\sqrt{\kappa + W_n - n\pi/\gamma} \, (\lambda + \kappa - n\pi/\gamma)},$$

(B.11d)

$$T_{\overline{n}}^{-}(\lambda) = \frac{\epsilon_n \, b_0}{(2\pi)^{1/2} \, \gamma} \frac{1}{\sqrt{\lambda - W_n} \, (\lambda + \kappa - n\pi/\gamma)} - T_{\overline{n}}^{+}(\lambda),$$

(B.11e)

and where $\lambda_j = -\kappa + (2j - n)\pi/\gamma$ as before. The prime on the summation sign in Eq. (B.11b) implies that the term corresponding to $j = 0$ is not included in the sum since the apparent pole $\lambda_0 = -\kappa - n\pi/\gamma$ of the first term on the right hand side of the Eq. (B.10) is cancelled by the zero in the numerator. Now, since both sides of Eq. (B.11a) behave to the leading order as λ^0 at infinity, according to Liouville's theorem the entire function $J(\lambda)$ defined by that equation is a constant; i.e., $J(\lambda) = K_1$. Thus, $C_{\overline{n}}^{+}(\lambda)$ and $D_{\overline{n}}^{-}(\lambda)$ are given by

$$C_n^+(\lambda) = i\,\gamma\;\frac{[(-1)^n\,e^{i\gamma(\lambda + \kappa)} - 1]}{\sqrt{1 - \gamma^2}\;\sqrt{\lambda + W_n}\,(\lambda + \kappa + n\pi/\gamma)}$$

$$\times\left[\,i\,\gamma\,K_1 + 2\pi\gamma^{-1}\sum_{j=-\infty}^{+\infty}{}' \frac{j\,D_n^-(\lambda_j)}{\sqrt{\lambda_j - W_n}\,(\lambda - \lambda_j)}\right.$$

$$\left.+\;\frac{\epsilon_n\,b_0}{(2\pi)^{1/2}}\;\frac{1}{\sqrt{\kappa + W_n - n\pi/\gamma}\,(\lambda + \kappa - n\pi/\gamma)}\right]\,,\qquad\text{(B.12a)}$$

$$D_n^-(\lambda) = -\,\gamma^{-1}\,\frac{\sqrt{\lambda - W_n}\,[(-1)^n\,e^{i\gamma(\lambda + \kappa)} - 1]}{(\lambda + \kappa + n\pi/\gamma)}$$

$$\times\left\{-\,\gamma\,K_1 + 2\pi i\gamma^{-1}\sum_{j=-\infty}^{+\infty}{}' \frac{j\,D_n^-(\lambda_j)}{\sqrt{\lambda_j - W_n}\,(\lambda - \lambda_j)}\right.$$

$$\left.-\;\frac{\epsilon_n\,b_0}{(2\pi)^{1/2}}\left[\frac{1}{\sqrt{\lambda - W_n}\,(\lambda + \kappa - n\pi/\gamma)} + \frac{i}{\sqrt{\kappa + W_n - n\pi/\gamma}\,(\lambda + \kappa - n\pi/\gamma)}\right]\right\}\,.$$

$$\text{(B.12b)}$$

Equations (B.12) are another representation for functions $C_n^+(\lambda)$ and $D_n^-(\lambda)$ involving the same unknown constants as Eqs. (B.7). Moreover, the new representation also contains an unknown constant K_1. Note that, the estimates for the asymptotic behavior of $C_n^+(\lambda)$ and $D_n^-(\lambda)$ at infinity as given by Eqs. (B.12), are in accordance with the ones given by Eq.

(B.8).

B.3 Third Choice:

Dividing Eq. (B.1a) by the function

$$Q_3(\lambda) = \frac{[(-1)^n e^{i\gamma(\lambda + \kappa)} - 1]}{(\lambda + \kappa - n\pi/\gamma)} \tag{B.13}$$

and proceeding as before, another representation for $C_n^+(\lambda)$ and $D_n^-(\lambda)$, given by

$$C_n^+(\lambda) = i \, \gamma^{-1} \, \frac{[(-1)^n e^{i\gamma(\lambda + \kappa)} - 1]}{\sqrt{1 - \gamma^2} \, \sqrt{\lambda + W_n} \, (\lambda + \kappa - n\pi/\gamma)}$$

$$\times \left\{ i \, \gamma \, K_2 + 2\pi\gamma^{-1} \sum_{j=-\infty}^{+\infty}{}' \frac{j \, D_n^-(\lambda_j)}{\sqrt{\lambda_j - W_n} \, (\lambda - \lambda_j)} \right.$$

$$\left. + \frac{\epsilon_n \, b_0}{(2\pi)^{1/2}} \, \frac{1}{\sqrt{\kappa + W_n + n\pi/\gamma} \, (\lambda + \kappa + n\pi/\gamma)} \right\}, \tag{B.14a}$$

$$D_n^-(\lambda) = - \gamma^{-1} \, \frac{\sqrt{\lambda - W_n} \, [(-1)^n e^{i\gamma(\lambda + \kappa)} - 1]}{(\lambda + \kappa - n\pi/\gamma)}$$

$$\times \left\{ - \gamma \, K_2 + 2\pi i\gamma^{-1} \sum_{j=-\infty}^{+\infty}{}' \frac{j \, D_n^-(\lambda_j)}{\sqrt{\lambda_j - W_n} \, (\lambda - \lambda_j)} \right.$$

148

$$- \frac{\epsilon_n \, b_0}{(2\pi)^{1/2}} \left[\frac{1}{\sqrt{\lambda - W_n} \, (\lambda + \kappa + n\pi/\gamma)} + \frac{i}{\sqrt{\kappa + W_n + n\pi/\gamma} \, (\lambda + \kappa + n\pi/\gamma)} \right] \Bigg\} \qquad \text{(B.14b)}$$

can be obtained where the prime on the summation sign in the equations above now implies that the term corresponding to $j = 2n$ is not included in the sum, since $\lambda_{2n} = - \kappa + n\pi/\gamma$ is not a pole. Note that the new representation contains an unknown constant K_2. The asymptotic estimate for behavior of $C_n^+(\lambda)$ and $D_n^-(\lambda)$ at infinity are in agreement with the ones given by the other two representations.

APPENDIX C

INFINITE SPAN SOLUTION

In this appendix, the solution to the problem of a high-frequency convected gust interacting with an infinite span swept airfoil is derived. As in the case of the finite span airfoil, ξ and ζ coordinates, which are aligned with the free stream and the airfoil leading edge, respectively, are introduced. Then, the equations derived in the beginning of the Chapter 3 apply. Hence,

$$\frac{\partial^2 h_m}{\partial \xi^2} + \frac{\partial^2 h_m}{\partial \zeta^2} - 2\gamma \frac{\partial^2 h_m}{\partial \xi \partial \zeta} + \frac{\partial^2 h_m}{\partial y^2} + k_x^2 \frac{M_\infty^2}{\beta_\infty^2} h_m = 0 , \tag{C.1a}$$

$$\left. \frac{\partial h_m}{\partial y} \right|_{y=0, \ \xi>0} = - b_m \, e^{i\kappa(\xi + \gamma\zeta)} \cos m\pi\zeta . \tag{C.1b}$$

Note that the factor $\cos m\pi\zeta$ on the right hand side of Eq. (C.1b) can be written as $(e^{im\pi\zeta} + e^{-im\pi\zeta})/2$. Therefore, every spatial mode m of the gust can be represented as the sum of two oblique plane wave gusts. Taking advantage of the linearity of the differential equation, one can write

$$h_m = h_m^{(+)} + h_m^{(-)} \tag{C.2a}$$

where $h_m^{(\pm)}(\xi, y, \zeta)$ satisfy

$$\frac{\partial^2 h_m^{(\pm)}}{\partial \xi^2} + \frac{\partial^2 h_m^{(\pm)}}{\partial \zeta^2} - 2\gamma \frac{\partial^2 h_m^{(\pm)}}{\partial \xi \partial \zeta} + \frac{\partial^2 h_m^{(\pm)}}{\partial y^2} + k_x^2 \frac{M_\infty^2}{\beta_\infty^2} h_m^{(\pm)} = 0 , \tag{C.2b}$$

150

$$\left.\frac{\partial h_m^{(\pm)}}{\partial y}\right|_{y=0,\ \xi>0} = -\frac{1}{2}\, b_m\, e^{i\kappa(\xi + \gamma\zeta)}\, e^{\pm im\pi\zeta} \ . \tag{C.2c}$$

Equation (C.2c) implies that $h_m^{(\pm)} \propto e^{i(\gamma\kappa \pm m\pi)\zeta}$. Extracting this phase factor by setting

$$h_m^{(\pm)}(\xi,y,\zeta) = g_m^{(\pm)}(\xi,y)\, e^{i(\gamma\kappa \pm m\pi)(\zeta + \gamma\xi)} \ , \tag{C.3a}$$

the reduced velocity potential $g_m^{(\pm)}(\xi,y)$ satisfies:

$$\frac{\partial^2 g_m^{(\pm)}}{\partial\xi^2} + \frac{\partial^2 g_m^{(\pm)}}{\partial y^2} + \frac{k_x^2}{\beta_\infty^2}\,[M_\infty^2 - (\gamma \pm m\pi/\kappa)^2]\, g_m^{(\pm)} = 0 \ , \tag{C.3b}$$

$$\left.\frac{\partial g_m^{(\pm)}}{\partial y}\right|_{y=0,\ \xi>0} = -\frac{1}{2}\, b_m\, e^{i[(1 - \gamma^2)\kappa \mp m\pi\gamma]\xi} \ . \tag{C.3c}$$

For positive values of the coefficient of $g_m^{(\pm)}(\xi,y)$ in Eq. (C.3b), one has propagating solutions while for negative values the solutions decay exponentially, i.e., the sound field is cut-off. Upon manipulating this coefficient, it is found that for a given k_x and M_∞, the critical sweep angles separating propagating and decaying solutions are given by

$$\alpha_{cr} = \tan^{-1}\!\left[- \tan\Lambda + M_\infty\, \sqrt{1 + \tan^2\Lambda}\, \right], \qquad \tan\Lambda = m\pi/k_x \tag{C.4}$$

where Λ is the angle of the convected gust vector relative to the streamwise direction (i.e., x-axis). The significance of Λ will be discussed in Section 3.3. For the simple case of a plane wave gust whose wavenumber vector is parallel to the streamwise direction (m = 0), Eq. (C.4) reduces to the simple result $\alpha_{cr} = \tan^{-1}(M_\infty)$ and $\Lambda = 0$. The solution to Eqs. (C.3) is well known and can be easily found using the Wiener-Hopf technique. In the interest of brevity, here only the final result is presented. The solution is

151

$$g_m^{(\pm)}(\xi,y) = - \frac{b_m \, \text{sgn}(y)}{4\pi \sqrt{(1-\gamma^2)\kappa + W_\pm}} \int_{-\infty}^{+\infty} \frac{e^{-i\lambda\xi - |y|\sqrt{\lambda^2 - W_\pm^2}}}{\sqrt{\lambda + W_\pm} \, [\lambda + (1-\gamma^2)\kappa]} \, d\lambda \qquad (C.5a)$$

where

$$W_\pm^2 = \frac{k_x^2}{\beta_\infty^2} [M_\infty^2 - (\gamma \pm m\pi/\kappa)^2] . \qquad (C.5b)$$

Note that $W_\pm$ is the coefficient of $g_m^{(\pm)}(\xi,y)$ in Eq. (C.3b). When orthogonal airfoil aligned coordinates are introduced, the solutions agree with those obtained by previous investigators (see for example, Adamczyk (1974)). Now, using Eq. (C.3a), the solution to Eqs. (C.1) can be written as

$$h_m(\xi,y,\zeta) = g_m^{(+)}(\xi,y) \, e^{i(\gamma\kappa + m\pi)(\zeta + \gamma\xi)} + g_m^{(-)}(\xi,y) \, e^{i(\gamma\kappa - m\pi)(\zeta + \gamma\xi)} . \qquad (C.6)$$

Equation (C.6) represents the complete solution to Eqs. (C.1).

Next, a formula for the gust (wake) trace velocity along the span relative to the oncoming mean flow is derived. The simplest way to develop the trace velocity formula is to consider the fluid as stationary. The gust constant phase line is then also a stationary line. The airfoil leading edge is now a moving line (with velocity U_∞) whose intersection point with gust constant phase line defines a point. The velocity of this point along the constant phase line as the airfoil moves through the stationary fluid is the desired trace velocity. Consider the location of the airfoil at two different times (say t and t + Δt, respectively) shown in Fig. (C.1). A is the intersection point between the airfoil leading edge and the gust constant phase line. In the time Δt that it takes for the leading edge of the airfoil to move a distance AA', the intersection point A moves a distance AA". One can, therefore, write

152
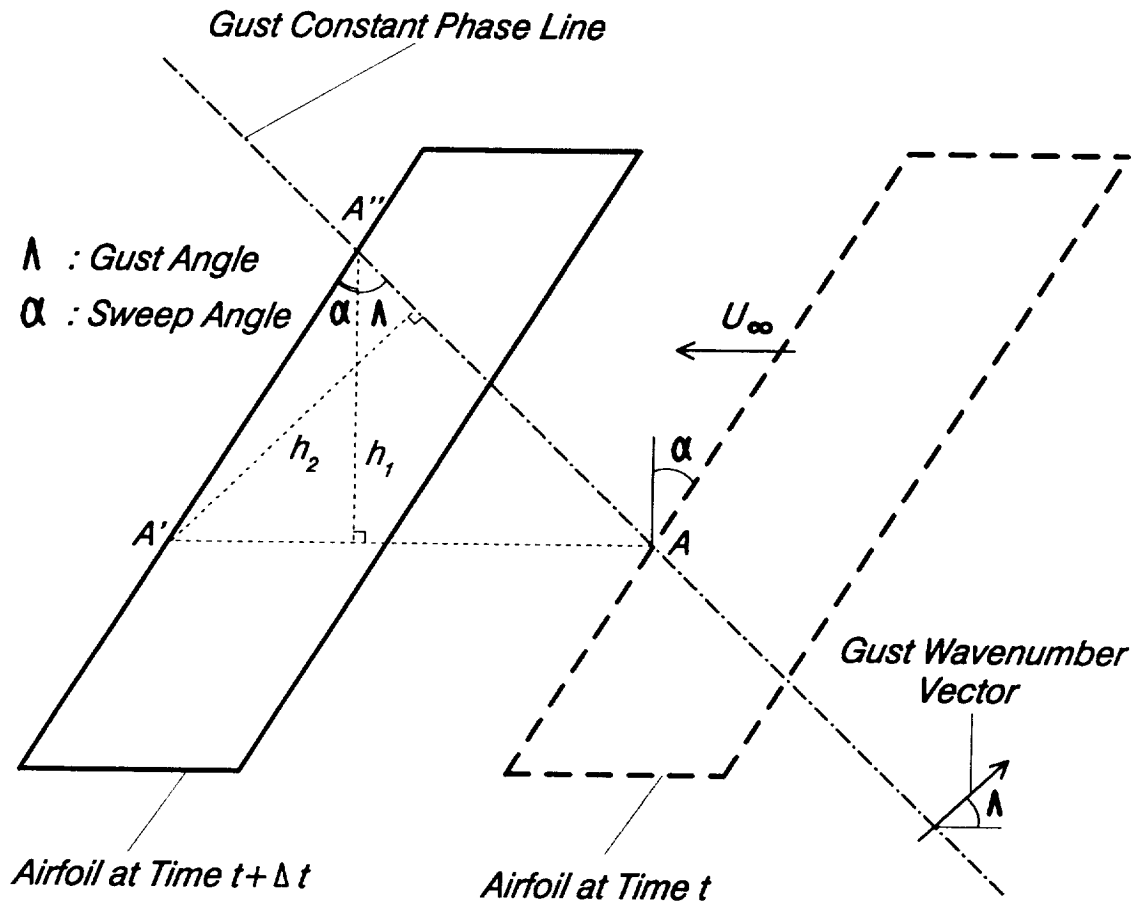
Fig. C.1 Schematic describing the gust spanwise relative trace velocity.

$$\Delta t = \frac{AA'}{U_\infty} = \frac{AA''}{V_{tr}} \tag{C.7}$$

where V_{tr} denotes the trace velocity of the gust along the leading edge. Solving for V_{tr} and noting that $AA''/AA' = h_1/h_2$, one find

$$V_{tr} = \frac{U_\infty \cos\alpha}{\sin(\alpha + \Lambda)} . \tag{C.8}$$

This is the formula for the spanwise gust trace velocity relative to the oncoming mean flow. To demonstrate the critical influence of this trace velocity on the character of the noise field produced by the interaction of a convected gust with an infinite span airfoil, note that Eq. (C.3b) can be rearranged as

$$\frac{\partial^2 g_m^{(\pm)}}{\partial \xi^2} + \frac{\partial^2 g_m^{(\pm)}}{\partial y^2} + \frac{(1 - \gamma^2) \, k_x^2}{\beta_\infty^2 (\tan\alpha + \tan\Lambda)^2} \left[\frac{M_\infty^2 \cos^2\alpha}{\sin^2(\alpha + \Lambda)} - 1 \right] g_m^{(\pm)} = 0 . \tag{C.9}$$

It is now clear that if V_{tr} is supersonic, the coefficient of the term $g_m^{(\pm)}$ is positive, hence acoustic waves propagate to the farfield. On the other hand if V_{tr} is subsonic, the coefficient is negative, and hence the noise field is cut-off (i.e., the waves decay exponentially in the farfield).

REFERENCES

Adamczyk, J.J., "Passage of a Swept Airfoil through an Oblique Gust," Journal of Aircraft, 11, 281-287 (1974).

Amiet, R.K., "High Frequency Thin-Airfoil Theory for Subsonic Flow," AIAA Journal, 14, 8, 1076-1082 (1976).

Carlson, J.F. and A.E. Heins, "The Reflection of Electromagnetic Waves by an Infinite Set of Plates I," Quarterly of Applied Mathematics, 4, 313-329 (1946).

Carrier, G.F., M. Krook and C.E. Pearson, Functions of a Complex Variable, McGraw-Hill, Inc., New York (1966).

Envia, E. and E.J. Kerschen, "Noise Produced by the Interaction of a Rotor Wake with a Swept Stator Blade," AIAA Paper No. 84-2326 (1984).

Envia, E. and E.J. Kerschen, "Noise Generated by Convected Gusts Interacting with Swept Airfoil Cascades," AIAA Paper No. 86-1872 (1986).

Filotas, L.T., "Response of an Infinite Wing to an Oblique Sinuosoidal Gust," Basic Aerodynamic Noise Research, NASA SP-207, 231-246 (1969).

Goldstein, M.E., Aeroacoustics, McGraw-Hill, New York (1976).

Graham, J.M.R., "Lifting Surface Theory for the Problem of an Arbitrarily Yawed Sinuosoidal Gust Incident on a Thin Aerofoil In Incompressible Flow," Aeronautical Quarterly, 21, 182-198 (1970).

Groeneweg, J.F. and E.J. Rice, "Aircraft Turbofan Noise," Transactions of the ASME, 109, 130-141 (1987).

Gutin, L., "On the Sound Field of a Rotating Propeller," NASA TM 1195 (1948).

Heins, A.E. and J.F. Carlson, "The Reflection of Electromagnetic Waves by an Infinite Set of Plates II," Quarterly of Applied Mathematics, 5, 82-88 (1947).

Heins, A.E., "The Reflection of Electromagnetic Waves by an Infinite Set of Plates III," Quarterly of Applied Mathematics, 8, 281-291 (1950).

Hodge, C.G., "Subsonic Transport Noise," AIAA Paper No. 80-0858 (1980).

Hayden, R.E. and D.B. Bliss, "Analysis and Design of a High-Speed Low-Noise Aircraft Fan Incorporating Swept Leading Edge Rotor and Stator Blades," NASA CR-135092 (1977).

Johnston, R.P., et al., "Energy Efficient Engine - Preliminary Design and Integration Study," NASA CR-135444 (1978).

Jones, D.S., "Diffraction by a Thick Semi-Infinite Plate," Proceedings of the Royal Society of London, A217, 153-175 (1953).

Kantola, R.A. and R.E. Warren, "Basic Research in Fan Source Noise - Inlet Distortion and Turbulence Noise", NASA CR 159451 (1978).

von Kármán, Th. and W.R. Sears, "Airfoil Theory for Non-Uniform Motion," Journal of Aeronautical Sciences, 5,(10), 379-390 (1938).

Kemp, N.H. and W.R. Sears, "The Unsteady Forces Due to Viscous Wakes in Turbomachines," Journal of the Aeronautical Sciences, 22, 478-483 (1955).

Kerschen E.J. and E. Envia, "Noise Generation by a Finite Span Swept Airfoil," AIAA Paper No. 83-0768 (1983).

Kovásznay, L.S.G., "Turbulence in Supersonic Flow," Journal of Aeronautical Sciences, 20, 657-674 (1953).

Küssner, H.G., "Summarized Report on the Unstable Lift of Wings," Luftfahrtforschung, 13, 410-424 (1936).

Landahl, M.T., "Theoretical Studies of Unsteady Transonic Flow - IV. The Oscillating Rectangular Wing with Control Surface," Aeronautical Research Institute of Sweden (FFA), Rept. 80 (1958).

Mani, R. and G. Horvay, "Sound Transmission Through Blade Rows," Journal of Sound and Vibration", 12 (1), 59-83 (1970).

Martinez, R. and S.E. Widnall, "Aerodynamic Theory for Wing with Side Edge Passing Subsonically through a Gust," AIAA Journal, 21, 808-815 (1983).

Morse, P.M. and H. Feshbach, Methods of Theoretical Physics, McGraw-Hill, Inc., New York (1953).

Noble, B., Methods Based on the Wiener-Hopf Technique, Pergamon Press, New York (1958).

Noble, B., "The Potential and Charge Distribution Near the Tip of a Flat Angular Sector," EM-135, NYU (1959).

Olver, F.W.J., Asymptotics and Special Functions, Academic Press, New York (1974).

Owens, R.E., "Energy Efficient Engine Propulsion System-Aircraft Integration Evaluation," NASA CR-159488 (1979).

Rice, E.J.,"Multimodal Farfield Acoustic Radiation Pattern Using Mode Cutoff Ratio," AIAA Journal, 16, 906-911 (1978).

Schulten, J.B.H.M., "A Lifting Surface Theory for the Sound Generated by the Interaction of Velocity Disturbances with a Leaned Stator," AIAA Paper No. 81-0091 (1981).

Shaw, L.M. and J.R. Balombin, "Rotor wake Characteristics Relevant to Rotor-Stator Interaction Noise Generation," AIAA Paper No. 81-2031 (1981).

Tyler, J.M. and T.G. Sofrin, "Axial Flow Compressor Noise Studies," ASME Transactions, 70, 309-332 (1961).

Report Documentation Page

1. Report No.	2. Government Accession No.	3. Recipient's Catalog No.
NASA CR–187052		

4. Title and Subtitle		5. Report Date
Influence of Vane Sweep on Rotor-Stator Interaction Noise		December 1990
		6. Performing Organization Code

7. Author(s)		8. Performing Organization Report No.
Edmane Envia and Edward J. Kerschen		None
		10. Work Unit No.
		535–03–10

9. Performing Organization Name and Address		11. Contract or Grant No.
Sverdrup Technology, Inc. Lewis Research Center Group 2001 Aerospace Parkway Brook Park, Ohio 44142		NAG3–357
		13. Type of Report and Period Covered

12. Sponsoring Agency Name and Address		Contractor Report
National Aeronautics and Space Administration Lewis Research Center Cleveland, Ohio 44135–3191		14. Sponsoring Agency Code

16. Abstract

In this study the influence of vane sweep on rotor-stator interaction noise is investigated. In an analytical approach, the interaction of a convected gust, representing the rotor viscous wake, with a cascade of finite span swept airfoils, representing the stator, is analyzed. The analysis is based on the solution of the exact linearized equations of motion. High-frequency convected gusts for which noise generation is concentrated near the leading edge of the airfoils are considered. In a preliminary study, the problem of an isolated finite span swept airfoil interacting with a convected gust is analyzed. Using Fourier transform methods and the Wiener-Hopf technique, an approximate solution for this problem is developed. Closed form expressions for the acoustic farfield are obtained and used in a parametric study to assess the effect of airfoil sweep on noise generation. Results indicate that sweep can substantially reduce the farfield noise levels for a single airfoil. Utilizing the single airfoil model, an approximate solution to the problem of noise radiation from a cascade of finite span swept airfoils interacting with a convected gust is derived. Only upstream radiated noise is considered. Neglecting the weak coupling between the adjacent airfoils at high frequencies, the cascade solution is constructed as a superposition of acoustic farfields emanating from an infinite number of isolated airfoils. A parametric study of noise generated by gust-cascade interaction is then carried out to assess the effectiveness of vane sweep in reducing rotor-stator interaction noise. The results of the parametric study show that, over a fairly wide range of conditions, sweep is beneficial in reducing noise levels. One conclusion of particular importance is that rotor wake twist or circumferential lean substantially influences the effectiveness of vane sweep. The orientation of the vane sweep must be chosen to enhance the natural phase lag caused by wake lean, in which case rather small sweep angles substantially reduce the noise levels.

17. Key Words (Suggested by Author(s))	18. Distribution Statement
Noise reduction; Rotor-stator interaction noise; Sweep; Finite span airfoil; Cascade; Convected gust; Rotor wake lean; Weiner-Hopf technique	Unclassified – Unlimited Subject Category 71

19. Security Classif. (of this report)	20. Security Classif. (of this page)	21. No. of pages	22. Price*
Unclassified	Unclassified	159	A08